A study of turbulence and scalar mixing in a wall-jet using direct numerical simulation

by

Daniel Ahlman

April 2006
Technical Reports from
Royal Institute of Technology
Department of Mechanics
SE-100 44 Stockholm, Sweden

Akademisk avhandling som med tillstånd av Kungliga Tekniska Högskolan i Stockholm framlägges till offentlig granskning för avläggande av teknologie licentiatexamen fredagen den 28 april 2006 kl 10.15 i D3, Huvudbyggnaden, Kungliga Tekniska Högskolan, Lindstedtsvägen 5, entréplan, Stockholm.

Universitetsservice US–AB, Stockholm 2006

A study of turbulence and scalar mixing in a wall-jet using direct numerical simulation

Daniel Ahlman
Dept. of Mechanics, Royal Institute of Technology
SE-100 44 Stockholm, Sweden

Abstract

Direct numerical simulation is used to study the dynamics and mixing in a turbulent plane wall-jet. The investigation is undertaken in order to extend the knowledge base of the influence of the wall on turbulent dynamics and mixing. The mixing statistics produced can also be used to evaluate and develop models for mixing and combustion. In order to perform the simulations, a numerical code was developed. The code employs compact finite difference schemes, of high order, for spatial integration, and a low-storage Runge-Kutta method for the temporal integration. In the simulations performed the inlet based Reynolds and Mach numbers of the wall jet were $Re = 2000$ and $M = 0.5$, respectively. Above the jet a constant coflow of 10% of the inlet jet velocity was applied. A passive scalar was added at the inlet of the jet, in a non-premixed manner, enabling an investigation of the wall-jet mixing as well as the dynamics. The mean development and the respective self-similarity of the inner and outer shear layers were studied. Comparisons of properties in the shear layers of different character were performed by applying inner and outer scaling. The characteristics of the wall-jet was compared to what has been observed in other canonical shear flows. In the inner part of the jet, $0 \leqslant y^+ \leqslant 13$, the wall-jet was found to closely resemble a zero pressure gradient boundary layer. The outer layer was found to resemble a free plane jet. The downstream growth rate of the scalar was approximately equal to that of the streamwise velocity, in terms of the growth rate of the half-width. The scalar fluxes in the streamwise and wall-normal direction were found to be of comparable magnitude.

Descriptors: wall-jet, direct numerical simulation, turbulence, scalar mixing

Preface

In this thesis, dynamics and mixing in a plane wall-jet are studied by means of direct numerical simulation. In the following introduction, a brief background and the context of the work is presented. In the enclosed papers, the results and conclusions of the performed simulations are presented and the developed simulation code is documented. The thesis is based on and contains the following papers;

Paper 1. Ahlman D., Brethouwer G and Johansson A. V., 2006
"Direct numerical simulation of a plane turbulent wall-jet including scalar mixing", To be submitted

Paper 2. Ahlman D., Brethouwer G. and Johansson A. V., 2006
"A numerical method for simulation of turbulence and mixing in a compressible wall-jet", Technical Report, Dept. of Mechanics, KTH, Stockholm Sweden

Division of work between authors

The project was initiated and defined by Arne Johansson (AJ) and Geert Brethouwer (GB). The work was performed by Daniel Ahlman (DA) under the supervision of AJ and GB.

The simulation and computation of statistics in Paper 1 was performed by DA. The paper was written by DA and examined by GB and AJ.

The code development described in Paper 2 was performed by DA. The report was written by DA and examined by GB and AJ.

Som för vindarnas våld ett moln försvinner,
som i klingande bäck en våg förrinner
likså människans dagar
rastlöst ila sin kos.

Erik Johan Stagnelius (1793–1823)

Contents

Part I

Introduction

CHAPTER 1

Introduction

1.1. Turbulence and combustion

One of the most prominent features of turbulent flows is the diffusivity. The turbulent flow state infers rapid mixing and transfer of fluid properties such as mass, momentum and heat. Turbulent mixing rates are significantly higher than mixing rates in laminar flows, where it occurs exclusively at the molecular level. In fact turbulent diffusivity is the reason why we stir our cup of coffee after adding milk, to quickly mix it evenly. Relying on the slow molecular mixing would leave us waiting till the coffee had cooled off.

The diffusivity of turbulence also has important implications in turbulent combustion. In technical applications such as automobile engines or gas turbines, combustion nearly always takes place in turbulent flow fields. The reason for this stems mainly from the fact that combustion is enhanced by the turbulence. For combustion, characterized by high rates of heat release, to occur, the participating species have to be mixed to the right proportions on the molecular level. The high rates of transport and mixing inherently present in the turbulent environment, generate a faster combustion and energy conversion rate. Combustion processes also include heat release, which through buoyancy and gas expansion can generate instabilities.

From this brief description it is evident that the combustion is strongly coupled to the turbulent flow field. Turbulence close to the flamefront may interact with the flame in a number of ways depending on the scale and strength of the turbulent fluctuation. Large, high intensity velocity fluctuations, may convolute the flame, increasing the flame surface and also the reaction rate. As the fluctuation scale becomes small and eventually of the order of the flame thickness it can enhance the mixing close to the flamefront but also quench the it locally through high strain.

The influence of combustion on turbulence, apart from the altered fluid dynamics due to density and temperature changes, is less prominent. However, when the temperature increases in the vicinity of the flame, owing to heat transfer from the reaction zone, the viscosity of the fluid increases and may locally modify the turbulence.

Gaseous turbulent combustion is subdivided into different régimes, describing the species initial mixing situation. The reaction processes are described as premixed, non-premixed or partially premixed turbulent combustion. In the

premixed régime the participating species are thought to be perfectly mixed before ignition. This is generally the case in spark-ignition engines, where the fuel and oxidizer are mixed by turbulence for sufficiently long time, prior to the spark ignition of the mixture. Premixed flames also possess an inherent flame speed. As the reaction progresses in the premixed régime, the flame propagates relative to the unburnt mixture.

When fuel and oxidizer enter the combustion chamber in separate streams prior to reaction, the combustion is instead termed non-premixed. The flames present in this combustion régime are commonly referred to as diffusion flames, indicating that diffusion processes are essential for bringing the fuel and oxidizer into contact. Contrary to flames in a premixed environment, diffusion flames do not possess an inherent flame speed. In aircraft turbines, the liquid fuel is injected into the combustion chamber. The liquid evaporates before it burns, typically in a non-premixed way in the form of diffusion flames. Incoming reactants from non-premixed streams must be continuously mixed and ignited by burnt gases, in order for the combustion to proceed. This process is referred to as flame stabilization and is often accomplished fluid dynamically by creating recirculation zones. Intermediate to these canonical régimes is partially premixed combustion. This occurs when fuel and oxidizer are injected separately but are able mix partially before ignition. This is generally speaking the case in diesel engines.

Combustion of fossil fuels globally constitutes the dominating source of energy. Energy from other sources such as hydroelectric, solar, wind and nuclear energy account for less than 20% of the total energy consumption. Combustion of fossil fuel will therefore prevail as a key energy conversion technology at least in the next few decades. However, the negative environmental impacts of excessive fossil fuel combustion are becoming evident. Emissions of CO_2 contribute to global warming. Other pollutants produced such as unburnt hydrocarbons, soot and nitrogen oxides (NO_x) have also been found to have a negative impact on the environment. Nitrogen oxides in particular contribute to acidification, photochemical smog and influence the ozone balance in the stratosphere. More rigorous regulations concerning emissions are presently enforced in the automotive industry and on power plants to reduce emissions and environmental impact. To reach these goals, an improved understanding of combustion and mixing processes is needed, as well as improved models to be used in the development of cleaner combustion applications.

The present thesis concerns the investigation of turbulent dynamics and mixing near a wall, by means of direct numerical simulation. The study is part of a long term project, with the aim of simulating combustion near cold solid walls. In the present work, simulations of passive scalar mixing in a turbulent plane wall-jet have been performed. Information of the underlying mixing processes is of importance for evaluation and development of combustion models. Since the wall-jet configuration contains a solid wall, a study of the wall influence on the dynamics and mixing is facilitated. In the following sections,

the interaction of the wall and turbulent combustion in the near-wall region is described. The role of numerical simulation in the study of combustion phenomena is outlined, and an overview of the area of combustion modeling is presented. In the section on modeling, the importance of accurately representing the mixing situation is emphasized.

1.2. Mixing and combustion near walls

In order to generate power, combustion processes often take place in chambers. Inside a chamber, some of the reaction and mixing is likely to occur close to, and be affected by, the solid enclosing walls. In the near-wall area, the interaction of the wall and the turbulent combustion will be complex. These interactions are outlined in figure 1.1. Since the solid wall usually is significantly colder

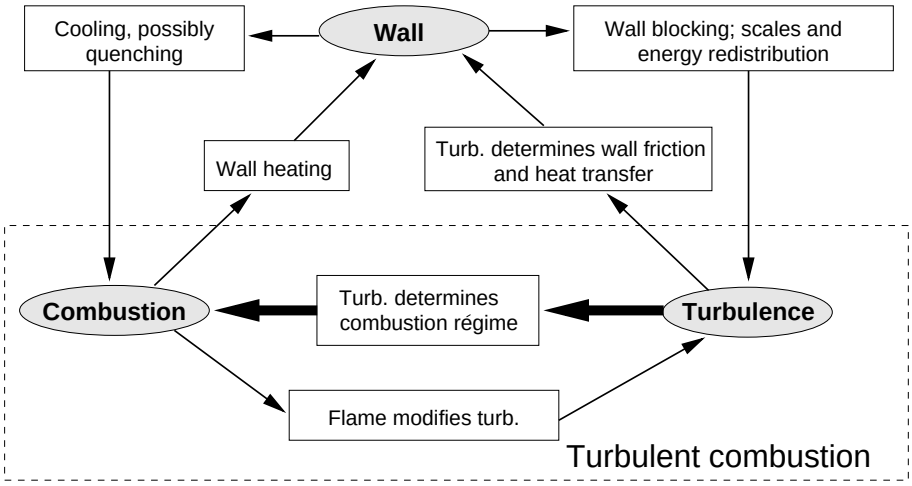

FIGURE 1.1. The interaction between the wall and the turbulent combustion (modified from Poinsot & Veynante (2001)).

than the burning mixture, a heat flux is generated towards the wall. The wall thus cools the flames. This can lead to flame quenching. In internal combustion engines, flame wall interaction is one of the dominant sources of unburnt hydrocarbon emission. Another influence of the wall is on the mixing of the reacting components. Close to the wall turbulent fluctuations are damped, resulting in reduced mixing.

Clearly the wall influences the mixing and combustion in the vicinity of the wall in a profound way. It is therefore of interest to study processes in this region, and to add to the knowledge of the complex interaction. Simulations of mixing and combustion near walls are useful for a number of reasons. Accurate experiments in this region are difficult since the region of interest is very close to the wall. Highly resolved simulations can be used to support model development. Most combustion models are developed for isotropic conditions

far from walls. It is not fully known how accurate the present models can capture wall effects on the mixing and combustion. Considering that walls have a profound impact, it is of interest to evaluate and develop accurate mixing and combustion models for the near-wall region.

1.3. The role of simulations

Direct numerical simulations (DNS) has emerged as a valuable tool in the study of mixing and combustion phenomena. Increasing computational resources have facilitated high resolution simulations, but also simulation of more complex phenomena including coupled fluid dynamics and chemistry.

The benefit of DNS in investigations of mixing and combustion is that it provides access to the complete solution, because all length and time scales are resolved. Higher order statistics such as correlations, probability density functions and conditional averages can be computed. The largest disadvantage of DNS is the computational cost. Since all scales have to be resolved, simulation of engineering application is not possible. The range of scales present in these makes the simulation prohibitively computationally demanding, even for the foreseeable future.

For simulations of reacting flows, the description of the reactions also have to be simplified. A complete mechanism for the simple reaction of hydrogen and oxygen gas typically involves 19 reactions and 9 species (Conaire *et al.* 2004). The combustion of a primary reference fuel (PRF) of iso-octane and n-heptane, used to evaluate the octane number of gasoline, is described by a mechanism of 4238 reactions and 1034 species (Curran *et al.* 2002).

Considering the limitations, DNS should be regarded as a useful tool for model development and evaluation. Highly resolved simulations of simplified model problems can produce information on how to construct accurate models, and can be used to test which model approach provides the most accurate prediction. Bilger (2000) presents an overview of the issues of current interest in turbulent combustion, including the status and outlook of present computational models. The recent progress in the application of DNS to study premixed turbulent combustion is reviewed by Poinsot *et al.* (1996), and non-premixed combustion is reviewed by Vervisch & Poinsot (1998).

Using experiments, measurements of the complete reaction phenomena and in some cases directly in the technical application, are possible. Also experimental techniques have exhibited a fast evolution. The advent of laser measurement technique has allowed for the development of fast and accurate measurement techniques. In comparison to simulation, experimental investigations however provide more localized information.

Studies of combustion near walls employing DNS include Poinsot *et al.* (1993) who studied flame-wall interaction of laminar and premixed combustion, through compressible two-dimensional DNS, using a simple reaction. Bruneaux *et al.* (1996) employed incompressible three-dimensional simulations of premixed combustion in a channel using a simple reaction. They found that

quenching distances decrease and maximum heat fluxes increase in comparison to those of laminar flames. Their DNS data was also used in Bruneaux *et al.* (1997) to develop and evaluate a flame surface density model. Using a complex reaction mechanism consisting of 18 reactions involving 8 species, one-dimensional premixed and non-premixed flame interaction with an inert wall was simulated by Dabrieau *et al.* (2003). Wang & Trouvé (2005) used DNS to study flame structure and extinction events of non-premixed flames interacting with a cold wall. Their simulation was fully compressible, two-dimensional and the reaction was described using a single step model containing four species.

1.4. Combustion models

Numerical computation of turbulent combustion is often divided into three categories in terms of the resolution of the computation. The highest level of resolution is reached by solving the governing equations without resorting to models, referred to as direct numerical simulation (DNS). The application of DNS to combustion was discussed in the previous section.

In large eddy simulation (LES) the large scales are resolved, while the smaller, unresolved scales, are modelled. By reducing the resolved range of scales the computational effort is also reduced. A review of the application of LES to combustion, and its modelling issues, is presented by Pitsch (2006).

The classical, and least computationally demanding approach, is to fully average the governing equations. This introduces unclosed terms that have to be modelled. During the last decades, a wide variety of combustion models based on this approach have been developed. Some of the more prominent models, presently used and still under development, include probability-density-function (pdf) models (Pope 1985), flamelet models (Peters (1971,2000)) and conditional moment closure methods (Klimenko & Bilger 1999). A recent overview of the state-of-the-art in combustion modeling has been published by Veynante & Vervisch (2002), but can also be found in Bilger (2000) and in the books of Poinsot & Veynante (2001) and Peters (2000).

1.4.1. *Averaged conservation equations*

Reacting flows in general include heat release, and therefore also significant density fluctuations. This has implications for the averaging of the governing equations. When averaging the conservation equations for constant density flows, Reynolds decomposition of the flow variables, into a mean $\bar{f}$ and fluctuating f' component, is conventionally used. Applying this to flows with varying density introduces unclosed correlations involving the fluctuating density of the type $\overline{\rho' f'}$. To reduce the number of unclosed terms, mass-weighted averages, also called Favre averages, are usually employed. Favre decomposition of an instantaneous variable f is performed through

$$f = \frac{\overline{\rho f}}{\bar{f}} + f'' = \widetilde{f} + f'' \tag{1.1}$$

where $\widetilde{f}$ denotes the mass-weighted mean and f'' the corresponding fluctuating part. Using this decomposition and formalism, the averaged equations for conservation of mass, momentum and the mass fractions $\theta_k = m_k/m$, of species $k = 1, \ldots, N$ involved in the reaction becomes

$$\frac{\partial \bar{\rho}}{\partial t} + \frac{\partial}{\partial x_i}(\bar{\rho}\widetilde{u}_i) = 0 \tag{1.2}$$

$$\frac{\partial \bar{\rho}\widetilde{u}_i}{\partial t} + \frac{\partial}{\partial x_j}(\bar{\rho}\widetilde{u}_i\widetilde{u}_j) = -\frac{\partial \bar{p}}{\partial x_i} + \frac{\partial}{\partial x_j}\left(\bar{\tau}_{ij} - \overline{\rho u_i'' u_j''}\right) \tag{1.3}$$

$$\frac{\partial \bar{\rho}\widetilde{\theta}_k}{\partial t} + \frac{\partial}{\partial x_i}(\bar{\rho}\widetilde{u}_i\widetilde{\theta}_k) = \frac{\partial}{\partial x_i}\left(\overline{\rho \mathcal{D}_k \frac{\partial \theta_k}{\partial x_i}} - \overline{\rho u_i'' \theta_k''}\right) + \overline{\dot{\omega}}_k \tag{1.4}$$

The Favre averaged equations are formally identical to the Reynolds averaged equations for constant density flows. The unclosed terms appearing in the equations are the Reynolds stresses $\overline{\rho u_i'' u_j''}$, the scalar fluxes $\overline{\rho u_i'' \theta_k''}$ and the reaction source term $\overline{\dot{\omega}}_k$. Closure for the Reynolds stress term is usually achieved with a RANS-type turbulence model, e.g. a k–ϵ model.

An often used model for the scalar flux is formulated in terms of a classical gradient diffusion assumption

$$\overline{\rho u_i'' \theta_k''} = \widetilde{\bar{\rho} u_i'' \theta_k''} = -\frac{\mu_t}{Sc_{kt}} \frac{\partial \widetilde{\theta}_k}{\partial x_i} \tag{1.5}$$

where μ_t is the turbulent viscosity, estimated from the turbulence model, and Sc_{kt} is the turbulent Schmidt number, which is usually of the order of one. In the case of reactive flow a gradient based model is a poor approximation for a number of reasons. The model can be argued to fail at the reaction zone, where the reaction influences the scalar flux. Furthermore it is assumed that the scalar flux is aligned with the mean gradient, which in general is not true (Wikström *et al.* 2000).

Modeling the reaction source term $\overline{\dot{\omega}}_k$ can be regarded as the key difficulty in modeling turbulent combustion. The problem can be appreciated by studying the simple reaction $F + O \rightarrow P$. The mean reaction rate of the Fuel species F is of the form

$$\overline{w}_F = -\overline{\rho^2 \theta_F \theta_O k} = -\overline{\rho^2 \theta_F \theta_O B e^{(-E_a/RT)}} \tag{1.6}$$

where $k(T)$ is the Arrhenius reaction rate constant and E_a the activation energy of the reaction. The reaction rate is highly temperature dependent, which can have implications in computations in terms of stiffness of the solution. Also, the reaction rate is a function of the product of the instantaneous species concentrations, which can be termed as the mixing. In fact if the reaction rate is sufficiently fast, which it often is, the combustion rate depends directly on the mixing rate. The full expression is highly non-linear, indicating that modeling in terms of mean variables is not suitable.

1.4.2. *The eddy break up (EBU) model*

An early attempt to model the mean reaction rate was proposed by Spalding (1971). In premixed combustion the model is formulated in terms of the progress variable $c = (T - T_u)/(T_b - T_u)$, reaching from 0 in the unburnt (T_u) to 1 in the completely burnt (T_b) mixture. Assuming that the reactions are sufficiently fast, the turbulent mixing becomes the rate-determining process, and the reaction rate is modelled as

$$\overline{\dot{\omega}} = \bar{\rho} C_{EBU} \frac{\sqrt{\widetilde{c''^2}}}{\tau_{EBU}} = \bar{\rho} C_{EBU} \frac{\epsilon}{k} \sqrt{\widetilde{c''^2}} \tag{1.7}$$

where C_{EBU} is a model constant, τ_{EBU} is a characteristic time scale of the reaction and c''^2 is the variance of the progress variable. Since fast reactions are assumed, the time scale is estimated to correspond to the integral time scale of the turbulent flow field $\tau_{EBU} = k/\epsilon$.

Also assuming that the flame is infinitely thin, the species can only take two values since it is either fresh or fully burnt. In this case the mean reaction rate can be written as

$$\overline{\dot{\omega}} = \bar{\rho} C_{EBU} \frac{\epsilon}{k} \widetilde{c}_k (1 - \widetilde{c}_k) \tag{1.8}$$

in terms of the known mean quantities. Due to the simplicity of the description, the eddy break up model is found in most commercial combustion codes. The obvious limitation of the model however is that no effects of chemical kinetics is included.

1.4.3. *Non-premixed combustion models*

In order to provide an example of how passive scalars enter into models of combustion, examples from the the modeling of non-premixed combustion are also presented here.

Models of non-premixed combustion are usually derived using a set of simplifying assumptions. Typical assumptions include constant and equal heat capacities for all species, low Mach numbers and unit Lewis numbers. Employing these assumptions, the flame position can be related to a scalar quantity, z, termed the mixture fraction. Using global conservation of species, linear combinations of the species and temperature, Z_j, can be constructed that eliminates the source terms. The scalars Z_j are all governed by the same balance equation,

$$\frac{\partial \rho Z}{\partial t} + \frac{\partial}{\partial x_i} \left(\rho u_i Z \right) = \frac{\partial}{\partial x_i} \left(\rho \mathcal{D} \frac{\partial \rho Z}{\partial x_i} \right) \tag{1.9}$$

when the diffusivity $\mathcal{D}$ has been assumed constant and equal for all species. Since the source term is eliminated, Z is a conserved scalar, subjected to diffusion and convection only. Reactions however plays an indirect role for the density and velocity fields by controlling the heat release. Normalization of the

variables Z_j can be performed through

$$z_j = \frac{Z_j - Z_j^O}{Z_j^F - Z_j^O} \tag{1.10}$$

where superscript F denotes values in the fuel stream and O values in the oxidizer stream. The normalized variables z_j are governed by the same balance equation and subjected to the same boundary condition; $z_j = 1$ in the fuel stream and $z_j = 0$ in the oxidizer stream. Hence all normalized variables are equal, reducing the problem to the solution of one conserved scalar, the mixture fraction z.

In turbulent combustion models, the solution of the averaged mixture fraction is sought. Using Favre averaging this becomes

$$\frac{\partial \bar{\rho}\widetilde{z}}{\partial t} + \frac{\partial}{\partial x_i}(\bar{\rho}\widetilde{u}_i\widetilde{z}) = \frac{\partial}{\partial x_i}\left(\overline{\rho\mathcal{D}\frac{\partial z}{\partial x_i}} - \bar{\rho}\widetilde{u_i''z''}\right). \tag{1.11}$$

In the averaged equation, the mixture fraction scalar flux $\widetilde{u_i''z''}$ is usually modelled using a gradient diffusion assumption of the form in (1.5). This gradient assumption is more justified for the mixture fraction, since it is a conserved scalar.

The introduction of a mixture fraction is used in many models. The reason for this is that it provides a possibility to avoid the direct closure of the species source term, which was seen in section 1.4.1 to be a hard task. The definition of the mixture fraction can essentially be used to split the solution of the mean flame properties, the mixture fractions and the temperature, into two problems; a mixing problem and a flame structure problem. The first problem consists of describing the underlying mixing situation, which is provided from the mixture fraction. For an accurate description, both the mean field $\widetilde{z}$ and higher order statistics, preferably the full pdf $p(z)$, are needed. Usually at least the variance $\widetilde{z''^2}$ is provided. In the following flame structure problem, the flame properties, mass fractions, temperature and species source terms, are recovered by using the mixture fraction information i.e. the flame properties are expressed conditionally on the mixture fraction and its higher moments.

When the pdf of z, $p(z)$ is known, the procedure to compute the average values, using the information of the underlying mixing can be expressed as

$$\bar{\rho}\widetilde{\theta}_k = \int_0^1 \left(\overline{\rho\theta_k|z^*}\right) p(z^*)dz^*, \quad \bar{\rho}\widetilde{T} = \int_0^1 \left(\overline{\rho T|z^*}\right) p(z^*)dz^* \tag{1.12}$$

$$\bar{\rho}\overline{\dot{\omega}}_k = \int_0^1 \left(\overline{\rho\dot{\omega}_k|z^*}\right) p(z^*)dz^*. \tag{1.13}$$

Here z^* is used to represent the mixture fraction and its higher moments e.g. the scalar dissipation rate χ described in section 1.4.5. $(\overline{f|z^*})$ denotes the conditional average of the quantity f for a set of mixture fraction statistics $z = z^*$.

As an example, using the flamelet model approach, the flame structure is characterized by the mixture fraction and the scalar dissipation rate at the reaction front χ_{st}. Flame structure functions of the form $\theta_k(z, \chi_{st})$ are pre-calculated for laminar flames and stored in "flamelet libraries". The averaged property can then be computed from

$$\bar{\rho}\widetilde{\theta_k} = \int_0^\infty \int_0^1 \rho\theta_k(z, \chi_{st})p(z, \chi_{st})dzd\chi_{st} \tag{1.14}$$

where $p(z, \chi_{st})$ is the joint pdf of the mixture fraction and the scalar dissipation rate at the reaction front.

1.4.4. *Infinitely fast chemistry*

In the limit of infinitely fast chemistry, the combustion is determined solely by the mixing. Moreover, since reaction is instant, the flame structure depends only on the mixture fraction z. The mean quantities can be computed as

$$\bar{\rho}\widetilde{\theta_k} = \int_0^1 \rho\theta_k(z)p(z)dz, \quad \bar{\rho}\widetilde{T} = \int_0^1 \rho T(z)p(z)dz \tag{1.15}$$

The only unknown in the infinitely fast chemistry limit is thus $p(z)$. The determination of the pdf of the mixture fraction in a reacting mixture is still an open question. Two possible routes are to either estimate the pdf using an assumed shape, or to solve a transport equation for the pdf (Pope 1985). For engineering purposes the first possibility is often sufficient. The most common assumed pdf is the β-function, which is defined as

$$p(z) = \frac{z^{a-1}(1-z)^{b-1}}{B(a,b)} \tag{1.16}$$

where B is a normalization function. The parameters a and b are determined from the mean $\widetilde{z}$ and variance $\widetilde{z''^2}$ of the mixture fraction as

$$a = \widetilde{z}\left(\frac{\widetilde{z}(1-\widetilde{z})}{\widetilde{z''^2}} - 1\right), \quad b = \frac{a}{\widetilde{z}} - a. \tag{1.17}$$

The structure of the pdf and also the complete flame is defined through the assumed pdf. The determination of the pdf requires information of the mixture fraction $\widetilde{z}$ and its variance $\widetilde{z''^2}$.

1.4.5. *Scalar variance transport equation*

Most combustion models require information on a scalar variance for closure. As was seen in the previous section, even in the limit of infinitely fast reactions using an assumed pdf approach, information on the passive scalar variance z''^2 is needed.

Regarding the mixing information contained in the mixture fraction, the mean field value $\widetilde{z}$ can be seen to represent the global location and the structure of the flame. For information of the local mixing situation, higher order statistics are needed. The mixture fraction variance $\widetilde{z''^2}$ provides the first level

of information of the local mixing. The scalar variance can be employed directly for closure in moment methods and in models employing assumed pdfs. In fact most higher level combustion models include assumed pdfs in their formulation. Both models using the flamelet approach, and conditional moment closure models include assumed pdfs.

In the RANS approach the variance is obtained from a transport equation. The transport equation for the mixture fraction variance $\widetilde{z''}$ reads

$$\frac{\partial \bar{\rho}\widetilde{z''^2}}{\partial t} + \frac{\partial}{\partial x_i}\left(\bar{\rho}\widetilde{u}_i\widetilde{z''^2}\right) = \underbrace{-\frac{\partial}{\partial x_i}\left(\overline{\rho u_i'' z''^2}\right)}_{I} + \underbrace{\frac{\partial}{\partial x_i}\left(\overline{\rho\mathcal{D}\frac{\partial z''^2}{\partial x_i}}\right)}_{II} - \underbrace{2\overline{\rho u_i'' z''}\frac{\partial \widetilde{z}}{\partial x_i}}_{III} - \underbrace{2\overline{\rho\mathcal{D}\frac{\partial z''}{\partial x_i}\frac{\partial z''}{\partial x_i}}}_{IV} \quad (1.18)$$

when $\mathcal{D}$ is constant. The the various right hand side terms are identified as (I) turbulent transport, (II) molecular diffusion, (III) production and (IV) dissipation. Closing the equation requires models for all the right-hand-side terms. For the turbulent transport, a gradient transport model of the form in (1.5) can be used. Molecular diffusivity is usually neglected, assuming sufficiently large Reynolds numbers. The scalar flux term in the turbulent production is modeled using a gradient model in conjunction with the transport term.

The dissipation term identified (IV), often referred to as the scalar dissipation rate, is an important quantity in combustion modeling. The scalar dissipation rate is a direct measure of the fluctuation decay. This can be seen by considering homogeneous combustion, i.e. negligible mean mixture fraction gradients, in which case the mixture fraction balance equation reduces to

$$\frac{\partial \bar{\rho}\widetilde{z''^2}}{\partial t} = -2\overline{\rho\mathcal{D}\frac{\partial z''}{\partial x_i}\frac{\partial z''}{\partial x_i}} = -\bar{\rho}\widetilde{\chi}_f \quad (1.19)$$

which shows that the decay is fully governed by the turbulent micro-mixing in terms of the scalar dissipation rate. This reflects the nature of the non-premixed flames where fresh fuel and oxidized have to be mixed on the molecular level and the reaction is mainly controlled by turbulent mixing. A commonly used model for the scalar dissipation rate $\widetilde{\chi}_f$ is to relate it to the turbulence time scale τ_t as

$$\widetilde{\chi}_f = c\frac{\epsilon}{k}\widetilde{z''^2} = c\frac{\widetilde{z''^2}}{\tau_t} \quad (1.20)$$

where k and ϵ are the turbulent kinetic energy and dissipation rate, and c is a model constant of order unity. The assumption implies that the respective scalar and turbulence time scales are proportional to each other.

The concept of scalar dissipation varies throughout the combustion literature. The main difference is whether it concerns the mean scalar or the fluctuation, i.e. z or z'', in the turbulent non-premixed case. A total Favre

averaged scalar dissipation rate $\widetilde{\chi}$ can be formulated as

$$\bar{\rho}\widetilde{\chi} = 2\overline{\rho\mathcal{D}\frac{\partial z}{\partial x_i}\frac{\partial z}{\partial x_i}} = 2\overline{\rho\mathcal{D}}\frac{\partial \widetilde{z}}{\partial x_i}\frac{\partial \widetilde{z}}{\partial x_i} + 4\overline{\rho\mathcal{D}\frac{\partial z''}{\partial x_i}}\frac{\partial \widetilde{z}}{\partial x_i} + 2\overline{\rho\mathcal{D}\frac{\partial z''}{\partial x_i}\frac{\partial z''}{\partial x_i}} \tag{1.21}$$

1.4.6. *Conclusion; scalar mixing*

In conclusion, scalar mixing can be stated to be of utmost importance in combustion modeling. In models of non-premixed combustion the mixing situation is characterized by a single conserved scalar, the mixture fraction $\widetilde{z}$, and its higher order statistics. Scalar variances are often used in closures and in prescribed pdfs.

The scalar dissipation rate $\widetilde{\chi}$ was found to be a key concept in combustion models, since it can be interpreted as a measure of the scalar fluctuation decay rate from turbulent micro-mixing. In fact either $\widetilde{\chi}$ or a closely related quantity can be found in any model. Apart from the micro-mixing description, accurate modeling of the scalar flux term $\widetilde{u''z''}$ is also important, since it has a large influence on $\widetilde{z}$ and $\widetilde{z''^2}$. From this description DNS can be used to develop combustion models, and to evaluate presently used models, since it can provide highly resolved information on the scalar mixing. Of particular interest is to evaluate the scalar dissipation and the validity of gradient based closures of scalar fluxes.

CHAPTER 2

Simulation of turbulent flow and mixing

2.1. Simulation code development

In order to study turbulence and scalar mixing by means of direct numerical simulation, a simulation code has been developed. All results in this chapter and the enclosed paper are produced using this code. The background of the code, the numerical techniques employed and the implementation are described in Ahlman *et al.* (2006). The simulation code was originally written by Dr. Bendiks Jan Boersma, and has previously been used in simulation of the sound field produced by a round jet (Boersma 2004). The basic structure, the computational techniques and the method for parallel computation have been maintained from the original implementation. The essential numerical method involves compact finite differences for the spatial integration and a Runge-Kutta method for the temporal integration. To reduce reflections, boundary zones are applied adjacent to in- and outlets.

The code solves the fully compressible fluid governing equations. This formulation was used in order to facilitate a later extension to reactive flow, including heat release and density fluctuations of significant magnitudes. The present study has required changes to the computational domain, redesign and tuning of the inlet and boundary conditions and the implementation of a passive scalar equation in order to study mixing. The spanwise direction was made periodic and a wall, with a no-slip boundary condition, was added at the bottom of the domain. To simulate a plane wall-jet, appropriate inlet profiles were developed. At the top of the domain an entrainment inflow was devised, using information from the experimental results of Eriksson *et al.* (1998). In the developing process it was found that large vortices, propagating into the quiescent region, were initiated at the simulation startup. These large scale structures were also very persistent and considerably affected the statistics. A parallel coflow was therefore added above the jet in order to advect the vortices out of the computational domain.

The purpose of the present study was to investigate turbulent mixing and dynamics in a plane wall-jet, therefore an effort was made to provide efficient inlet disturbances to trigger the transition. Early simulations, using random noise added at the inlet, showed that the transition took place far downstream of the inlet. It can be noted that random noise is not the ideal candidate to trigger transition, because the introduced length and time scale are very small,

of the order of the node spacing and time, increment respectively. Considering that the flow case, a wall-jet can be seen to require a longer transition region than a plane jet (see e.g. Stanley *et al.* 2002). Effective disturbances are required to enforce a reasonably fast transition to turbulence. For the wall-jet simulations three types of inlet disturbances are used; correlated disturbances, streamwise vortices and periodic streamwise forcing. Correlated disturbances are produced using a digital filter (Klein *et al.* 2003) using an assumed autocorrelation. Streamwise vortices are added in the upper shear layer of the wall jet in the light of the investigation of Levin *et al.* (2005), who found that streamwise streaks in the upper shear layer enhanced the breakdown in a plane wall-jet.

In the simulations, spurious negative scalar concentrations appear in the outer part of the jet. The reason for this, is the steep gradients present in this region.

The compact finite difference scheme uses a central form, which is known to have dispersion errors. The errors introduced could possibly be reduced by applying an upwind scheme to the scalar equation. However, the development of an effective and high order upwind formulation for a turbulent flow, is a difficult task.

In the simulation, the streamwise grid stretching is adjusted to decrease the node separation over the transition region, where strong disturbances are produced. Filters of reduced order where tested in order to remove the high scalar gradients. To completely remove the negative scalar instances required a second order filter. During simulation the second order filter is continuously applied to the scalar, however with a reduced frequency than the filters applied to the other variables, to reduce the introduced diffusivity.

To reduce the negative scalar concentrations the grid was stretched in the streamwise direction, increasing the node density in the transition region, and a low order filter was applied to the scalar. The negative scalar instances were completely removed in the transition region by a second order filter. The frequency of the filter applications was reduced in order to minimize the introduced diffusivity, and a higher order filter was used in the downstream region with turbulent flow.

2.2. Early simulation results

The aim of the current research is to simulate dynamics and mixing in a wall-bounded domain. The flow setup used in this study is a plane wall-jet. All simulations performed have employed an inlet based Reynolds and Mach number of $Re = U_{in}h/\nu = 2000$ and $M = U_{in}/a_\infty = 0.5$, where h is the jet height at the inlet and a_∞ the ambient speed of sound. A parallel coflow of $U_c = 0.10U_{in}$ was applied above the jet. The computational domain used in the simulations is depicted in figure 2.1. Early results from the plane wall-jet simulations have been presented at the 10th European Turbulence Conference

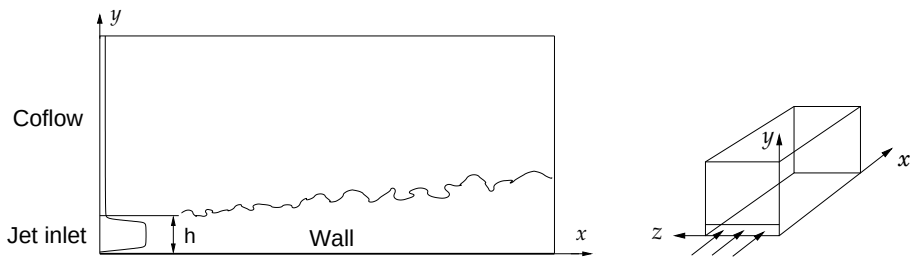

FIGURE 2.1. Plane wall-jet computational domain.

in Trondheim Norway in 2004 (Ahlman *et al.* 2004) and at the Fourth International Symposium on Turbulence and Shear Flow Phenomena in Williamsburg, Virginia, USA in 2005 (Ahlman *et al.* 2005). The results presented at the latter conference were generated from a wall-jet simulation using a computational box of size $37h \times 16h \times 8h$ in the streamwise, wall-normal and spanwise direction, respectively, and the resolution was $256 \times 192 \times 96$ nodes. The flow statistics were compared to the experimental data of Eriksson *et al.* (1998). Their wall-jet experiments were carried out in a water tank, using an inlet Reynolds number of $Re = 9600$, and comprised measurements in the viscous sublayer of the wall. In the simulation the spreading of the wall-jet, in terms of the growth rate of the half-width, $y_{1/2}$, was found to be approximately linear. The half-width of wall-jet is defined as the distance from the wall to the position where the mean velocity is $\frac{1}{2}(U_m - U_c)$, where U_m is the local maximum jet velocity and U_c is the coflow velocity. The scalar half-width is defined in analogy as the distance from the wall to the position with mean scalar concentration of $\Theta = \Theta_m/2$, where Θ_m is the local maximum scalar concentration, occurring at the wall. The linear half-width development also holds for free plane jets, where it can be derived from classical self-similarity analysis (Pope 2000). The magnitude of the growth rate is however reduced in the wall-jet in comparison to that of a plane jet in agreement with wall-jet experiments reviewed by Launder & Rodi (1983).

Using separate inner and outer scaling the wall-normal velocity fluctuations were found to agree well with the experiments, despite the difference in Reynolds number. In the inner region, close to the wall an inner scaling led to collapse of the profiles, and in the outer part an outer scaling provided an approximate collapse. This indicated that the inner and outer layer possess fundamentally different properties. Concerning the mixing, the scalar flux was found to consist of a single peak positioned in the outer layer, with the maximum at the scalar half-width position. Mixing is thus dominant in the outer layer. This is expected since the outer region contains larger length scales.

The mixing processes in the inner and outer shear layers were further studied using pdfs. In figure 2.2 joint pdfs of the wall normal fluctuating velocity and the fluctuating scalar concentration are reproduced from Ahlman *et al.*

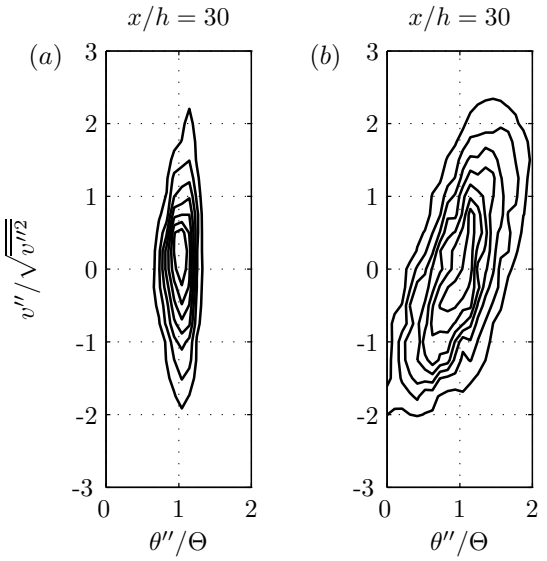

FIGURE 2.2. Joint pdfs of the wall-normal velocity fluctuation, scaled by the local rms-value, and the scalar fluctuation, scaled by the local mean. Pdfs acquired at wall normal distances of $u''(y_{in}) = u''_{\text{inner peak}}$ (a) and $y_{out}/y^{\theta}_{1/2} = 1$ (b)

(2005). The velocity fluctuation is normalized by the local root-mean-square (rms) of the fluctuation while the scalar fluctuation is normalized by the local mean scalar concentration. Both pdfs shown are extracted from the DNS at a downstream distance of $x/h = 30$, where the wall-jet is fully turbulent, but at different distances from the wall. The inner pdf is obtained from the position of maximum streamwise fluctuation, and the outer is obtained at the velocity half-width position. The pdfs at the inner and outer location reveal a significant difference in the respective regions. The inner pdf is aligned with the vertical direction, hence indicating that the velocity and scalar fluctuations are uncorrelated. The outer pdf on the other hand exhibits a positive inclination, indicating that low concentration fluid is correlated to velocity fluctuations towards the wall and vice versa.

The turbulence transition region of the simulation was found to occupy a substantial part of the computational domain in the simulations. The applied inlet disturbances consisted of correlated inlet disturbances (Klein *et al.* 2003). The disturbance length scale was however short, $l \ll h$, which most likely reduced the effect of the disturbances on the transition. In the next simulation, an effort was therefore made to improve the inlet disturbances.

2.3. Summary of results in paper 1

The simulation in paper 1 concerns a plane wall-jet of the same inlet Reynolds and Mach number as in previous simulations, $Re = 2000$, $M = 0.5$. The computational domain was increased to $47h \times 18h \times 9.6h$, and the resolution to $384 \times 192 \times 128$ nodes in the streamwise, wall-normal and spanwise directions, respectively. The larger computational domain allowed a more thorough study of the self-similarity of the wall-jet and comparison with the experimental data of Eriksson *et al.* (1998). Inlet disturbances were generated through a superposition of filtered correlated disturbances, using a length scale of $l = h/3$, streamwise vortices positioned in the upper shear layer and a periodic forcing in the streamwise component. To reduce negative concentrations in the outer layer, the grid was refined to contain more nodes in the transition region and a second order filter was applied to the scalar over the transition region. The Schmidt and Prandtl numbers of the jet were $Sc = 1$ and $Pr = 0.72$. Statistics of the flow field and the scalar mixing were sampled over a time period of $t_{samp} = 309t_j$ where $t_j = h/U_{in}$ is the inlet time scale of the jet.

A view of the simulated wall-jet is shown in figure 2.3, where instantaneous solutions of the streamwise velocity and the scalar concentration are plotted in an xy-plane. The jet enter the domain at the lower left corner, and it is seen that the inlet disturbances enforce a quick transition.

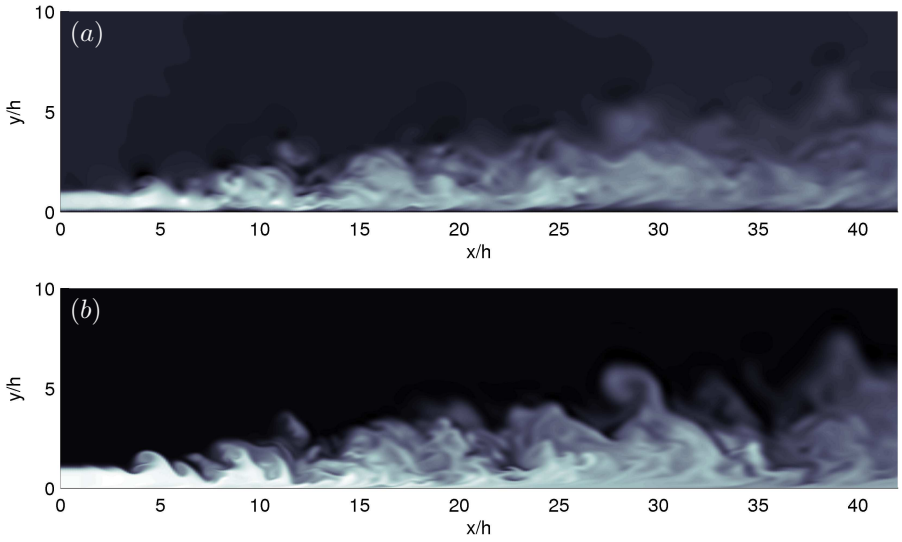

FIGURE 2.3. Instantaneous plots of the streamwise velocity, u (a) and the scalar concentration θ (b) in an xy-plane. For the velocity light areas represent positive values and dark negative, while for the scalar light areas represent finite concentration and dark areas correspond to zero concentration.

Concerning the spreading rate of the wall-jet, the velocity half-width increases approximately linearly with downstream distance, $dy_{1/2}/dx = 0.068$. The velocity and scalar half-width exhibit an approximately equal growth rate, which is in contrast to the mixing situation in a plane jet, where the mean scalar profile is wider than the velocity profile. The growth rates obtained from the DNS and the measurements of Eriksson *et al.* (1998) are shown in figure 2.4.

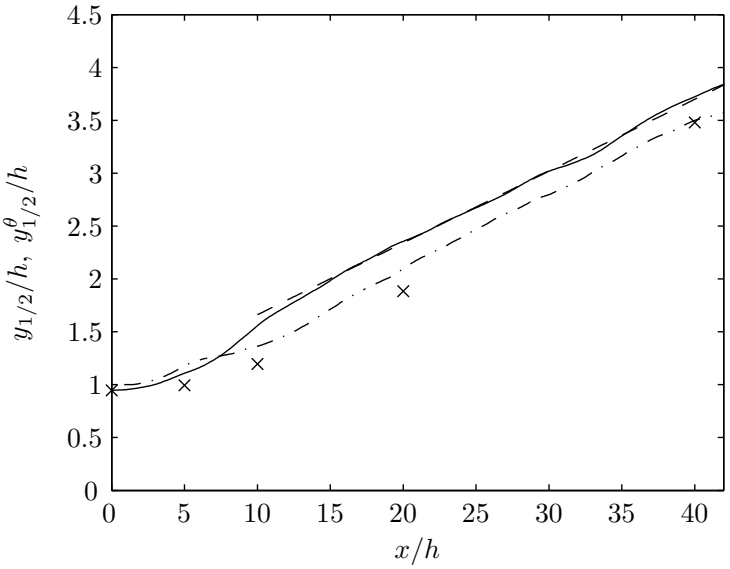

FIGURE 2.4. Wall-jet growth rate; velocity half-width $y_{1/2}/h$ (solid), linear fit (dashed), scalar half-width $y^{\theta}_{1/2}$ (dash-dotted) and experimental values for the velocity half-width by Eriksson *et al.* (1998) ($\times$).

The maximum streamwise velocity decay, in terms of $(U_{in} - U_c)^2/(U_m - U_c)^2$, is also approximately linear downstream of $x/h = 15$, whereas in the experiments of Eriksson *et al.* (1998) the linear behavior is observed at $x/h > 70$. This difference is presumably owing to the strong disturbances applied in the simulations as well as the difference in Reynolds number.

The properties of the inner and outer shear layers were investigated by applying respective inner and outer scaling. In figure 2.5 the mean streamwise profiles are shown in inner scaling, using the friction velocity $u_\tau = \sqrt{\tau_w/\rho}$ and the corresponding inner length scale $l^* = \nu/\nu_\tau$, in accordance with classical boundary layer scaling. Using inner scaling the mean velocities profiles collapse in the inner region $0 \leqslant y^+ \leqslant 13$. Profiles of the fluctuation intensities were also found to collapse in this region using the same inner scaling. A viscous sublayer is found in the profiles, extending out to $y^+ = 5$, and the position of the maximum streamwise fluctuation agrees with that observed in boundary

layers. The near wall region in a plane-wall jet is thus concluded to resemble a turbulent zero pressure gradient boundary layer. The outer part of the mean

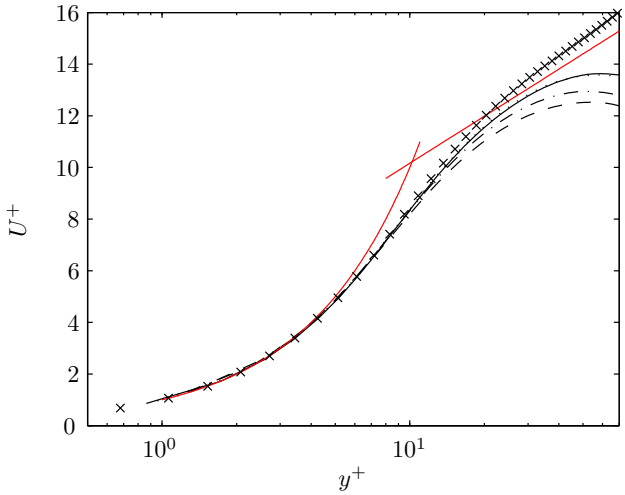

FIGURE 2.5. Mean velocity profiles in inner scaling ($U^+ = U/u_\tau$, $y^+ = yu_\tau/\nu$) at different downstream positions; $x/h = 15$ (dashed), $x/h = 20$ (dashed-dotted), $x/h = 30$ (dotted) and $x/h = 40$ (solid). The linear viscous relation $U^+ = y^+$, the logarithmic inertial relation $U^+ = \frac{1}{0.38}\ln(y^+) + 4.1$ and DNS data ($Re_{\delta^*} = 200$) from Skote *et al.* (2002) ($\times$) are also shown.

streamwise profiles, from the maximum position and further out, are shown in figure 2.6 using an outer scaling. The velocity difference ($U_m - U_c$) and the half-width $y_{1/2}$ are employed for outer scaling, in analogy with what is used in self-similar plane jets. The outer scaling is found to lead to a collapse of the outer part of the profiles, and hence this region is found to resemble a free plane jet.

The scalar fluctuation intensity is constant in the viscous sublayer in the DNS. In the outer layer the values of the scalar fluctuation intensities corresponds to what is observed in a plane jet.

The scaling of the streamwise and wall-normal turbulent scalar flux was also studied. In the outer part of the jet, the flux components are of comparable magnitudes, although the mean scalar gradient is approximately perpendicular to the wall. In the inner region the streamwise flux intensity increases with downstream distance, attaining significant values at $x/h > 30$. Non-zero streamwise flux has previously been observed in channel flow and in plane jets, and can be explained by observing that the production term of the scalar flux transport equation is non-zero.

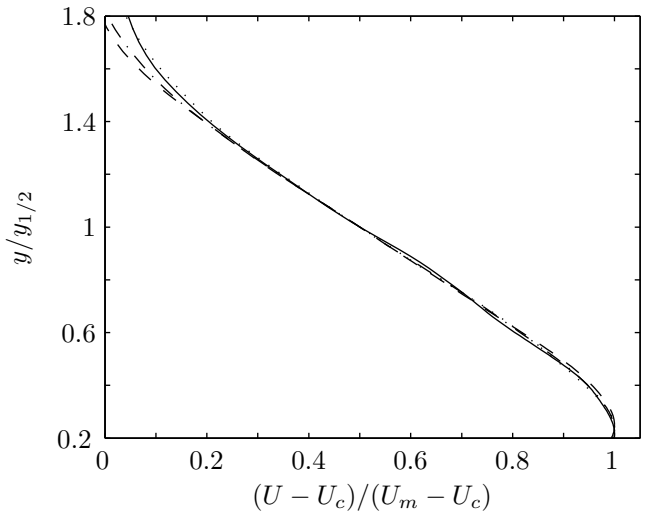

FIGURE 2.6. Mean velocity profiles in the outer shear layer, using an outer scaling adjusted for the coflow. Profiles at increasing downstream positions; $x/h = 15$ (dashed), $x/h = 20$ (dashed-dotted), $x/h = 30$ (dotted) and $x/h = 40$ (solid)

Acknowledgements

I would first and foremost like to express my gratitude to my supervisors, for their invaluable guidance and support. Professor Arne Johansson; your vast knowledge in fluid mechanics, in combination with your management skills, are ever encouraging. Doctor Geert Brethouwer; thank you for introducing me to direct numerical simulations, and for taking the time to answer all my questions on it.

The Centre for Combustion Science and Technology (CECOST) and the Swedish Energy Agency (Energimyndigheten) are gratefully acknowledged for financing this work.

Computer time have been provided by The Swedish National Allocation Committee (SNAC). The simulations were carried out using resources at The Center for Parallel Computers (PDC) at The Royal Institute of Technology (KTH).

A special thanks is extended to Doctor Bendiks Jan Boersma, for providing the original version of the simulation code, and for extensively answering my questions on numerical techniques.

I would like to thank Docent Tony Burden for examining and providing valuable feedback on the combustion background. I am also indebted to Doctor Gunnar Tibert for scrutinizing the thesis, and for fatherly guiding me in the art of scientific typesetting. Anders Rosén is acknowledged for discussions on any and all aspects of computers, at just about any time of the day.

All colleagues at the Department of Mechanics are thanked for providing a friendly and inspiring environment. In particular I would like to thank the past and present inhabitants of Plan 8, for always bringing a smile to my face. The lunch gang are greatfully acknowledged for providing me with numerous opportunities for uncontrollable laughter. All great friends outside of the Department are thanked for being precisely that.

Slutligen vill jag tacka min familj för all kärlek, stöd och uppmuntran!

Bibliography

Ahlman, D., Brethouwer, G. & Johansson, A. V. 2004 Simulation and mixing in a plane compressible wall jet. In *Advances in Turbulence X*, pp. 369–372.

Ahlman, D., Brethouwer, G. & Johansson, A. V. 2005 Direct numerical simulation in a plane compressible and turbulent wall jet. In *Fourth international symposium on Turbulence and Shear Flow Phenomena*, pp. 1131–1136.

Ahlman, D., Brethouwer, G. & Johansson, A. V. 2006 A numerical method for simulation of turbulence and mixing in a compressible wall-jet. *Tech. Rep*. Dept. of Mechanics, Royal Instutute of Technology.

Bilger, R. W. 2000 Future progress in turbulent combustion research. *Prog. Energy Combust. Sci.* **26**, 367–380.

Boersma, B. J. 2004 Numerical simulation of the noise generated by a low Mach number, low Reynolds number jet. *Fluid Dyn. Res.* **35** (6), 425–447.

Bruneaux, G., Akselvoll, K., Poinsot, T. & Ferziger, J. H. 1996 Flame-wall interaction simulation in a turbulent channel flow. *Combust. Flame* **107**, 27–44.

Bruneaux, G., Poinsot, T. & H., F. J. 1997 Premixed flame-wall interaction in a turbulent channel flow: budget for the flame surface density evolution equation and modeling. *J. Fluid Mech.* **349**, 191–219.

Conaire, M. O., Curran, H. J., Simmie, J. M., Pitz, W. J. & Westbrook, C. K. 2004 A comprehensive modeling study of hydrogen oxidation. *Int. J. Chem. Kinet.* **36**, 603–622.

Curran, H. J., Gaffuri, P., Pitz, W. J. & Westbrook, C. 2002 A comprehensive modeling study of iso-octane oxidation. *Combust. Flame* **129**, 253–280.

Dabrieau, F., Cuenot, B., Vermorel, O. & Poinsot, T. 2003 Interaction of flames of $H_2 + O_2$ with inert walls. *Combust. Flame* **135**, 123–133.

Eriksson, J. G., Karlsson, R. I. & Persson, J. 1998 An experimental study of a two-dimensional plane turbulent wall jet. *Experiments in Fluids* **25**, 50–60.

Klein, M., Sadiki, A. & Janicka, J. 2003 A digital filter based generation of inflow data for spatially developing direct numerical or large eddy simulations. *J. Comp. Phys.* **186**, 652–665.

Klimenko, A. Y. & Bilger, R. W. 1999 Conditional moment closure for turbulent combustion. *Prog. Energy Combust. Sci.* **25**, 595–687.

Launder, B. E. & Rodi, W. 1983 The turbulent wall jet – measurements and modelling. *Ann. Rev. Fluid Mech.* **15**, 429–459.

Levin, O., Chernoray, V. G., Löfdahl, L. & Henningson, D. 2005 A study of the blasius wall jet. *J. Fluid Mech.* **539**, 313–347.

Peters, N. 1971 Laminar flamelet concepts in turbulent combustion. In *Twenty-First Symposium (Int.) on Combustion*, pp. 1231–1250. The Combustion Institute, Pittsburgh.

Peters, N. 2000 *Turbulent Combustion*. Cambridge University Press.

Pitsch, H. 2006 Large-eddy simulation of turbulent combustion. *Ann. Rev. Fluid Mech.* **38**, 453–482.

Poinsot, T., Candel, S. & A., T. 1996 Applications of direct numerical simulation to premixed turbulent flames. *Prog. Energy Combust. Sci.* **21**, 531–576.

Poinsot, T., Haworth, D. C. & G., B. 1993 Direct simulation and modeling of flame-wall interaction for premixed turbulent combustion. *Combust. Flame* **95**, 118–132.

Poinsot, T. & Veynante, D. 2001 *Theoretical and Numerical Combustion*. R.T. Edwards.

Pope, S. B. 1985 Pdf methods for turbulent reactive flows. *Prog. Energy Combust. Sci.* **11**, 119–192.

Pope, S. B. 2000 *Turbulent Flows*. Cambridge University Press.

Skote, M., Haritonidis, J. H. & Henningson, D. 2002 Varicose instabilities in turbulent boundary layers. *Phys. Fluids* **14** (7), 2309–2323.

Spalding, D. 1971 Mixing and chemical reaction in steady confined turbulent flames. In *Thirteenth Symposium (Int.) on Combustion*, pp. 649–657. The Combustion Institute, Pittsburgh.

Stanley, S. A., Sarkar, S. & Mellado, J. P. 2002 A study of flow-field evolution and mixing of in a planar turbulent jet using direct numerical simulation. *J. Fluid Mech.* **450**, 377–407.

Vervisch, L. & Poinsot, T. 1998 Direct numerical simulation of non-premixed turbulent flames. *Ann. Rev. Fluid Mech.* **30**, 655–691.

Veynante, D. & Vervisch, L. 2002 Turbulent combustion modeling. *Prog. Energy Combust. Sci.* **28**, 193–266.

Wang, Y. & Trouvé 2005 Direct numerical simulation of nonpremixed flame-wall interactions. *Combust. Flame* **144**, 461–475.

Wikström, P. M., Wallin, S. & Johansson, A. V. 2000 Derivation and investigation of a new explicit algebraic model for the passive scalar flux. *Phys. Fluids* **12**, 688–702.

Part II

Papers

1

Paper 1

Direct numerical simulation of a plane turbulent wall-jet including scalar mixing

By Daniel Ahlman, Geert Brethouwer and Arne V. Johansson

KTH Mechanics, SE-100 44 Stockholm, Sweden

To be submitted

Direct numerical simulation is used to study a turbulent plane wall-jet including the mixing of a passive scalar. The inlet based Reynolds and Mach numbers are $Re = 2000$ and $M = 0.5$ respectively. A constant coflow of 10% of the inlet jet velocity is applied above the wall-jet. The passive scalar is added to the jet, at the inlet, in a non-premixed manner, enabling the investigation of the wall-jet mixing as well as the dynamics. The mean development and the respective self-similarity of the inner and outer shear layers are studied. Comparisons of properties in the shear layers of different character are performed by applying inner and outer scaling. The characteristics of the wall-jet is compared to what is reported for other canonical shear flows. In the inner part, out to approximately $y^+ = 13$, the wall-jet is found to closely resemble a zero pressure gradient boundary layer. The outer layer is found to resemble a free plane jet. The downstream growth rate of the scalar is approximately equal to that of the streamwise velocity, in terms of the growth rate of the half-width. The scalar fluxes in the streamwise and wall-normal direction are found to be of comparable magnitude.

1. Introduction

A plane wall jet is obtained by injecting fluid, with high velocity parallel to a wall, in such a way that the velocity of the fluid over some distance from the wall supersedes that of the ambient flow. The structure of a turbulent wall jet can be described as composed of two canonical shear layers of different character. The inner shear layer, from the wall to the point of maximum streamwise velocity, resembles a boundary layer, while the outer layer from the maximum velocity out to the ambient fluid resembles a free shear layer. A consequence of the double shear layer structure is that properties such as momentum transfer and mixing will exhibit distinctively different character and scalings in the two shear layers.

Plane wall jets are used in a wide range of engineering applications. Many of these applications apply wall jets to modify heat and mass transfer close

to walls. Well known examples of these are e.g. film-cooling of leading edges of turbine blades and in automobile demisters. In the first applications, the purpose is to use a cool layer of fluid to protect the solid surface from the hot external stream, while in the case of the demister, warm jet fluid is used to heat the inside of the wind shield. An important aspect in these applications is turbulent mixing in the vicinity of walls. However, the mixing processes in this region are presently not fully understood, and it is therefore of interest to add to this knowledge. An extended understanding of the mixing properties close to walls is also of relevance for applications containing combustion. In most combustion systems, such as in internal combustion engines and in gas turbines, part of the combustion takes place in the vicinity of walls. The aim of the present simulation effort is hence to study the dynamics and mixing in a plane wall jet.

The first experimental work on plane wall jets was carried out by Förthmann (1936). He concluded that the mean velocity field develops in a self-similar manner, the half-width grows linearly and that the maximum velocity is inversely proportional to the square root of the downstream distance. Glauert (1956) studied the wall jet theoretically, seeking a similarity solution to the mean flow by applying an empirical eddy viscosity model. However, because different eddy viscosities are needed in the inner and outer part of the jet he concluded that a single similarity solution is not possible. Bradshaw & Gee (1960) were the first to present turbulence measurements from a wall-jet and reported that the shear stress attains a finite value at the point of maximum velocity. Tailland & Mathieu (1967) reported a Reynolds number dependency of the half-width growth and maximum velocity decay.

The wall jet experiments carried out prior to 1980 have meritoriously been compiled and critically reviewed by Launder & Rodi (1981,1983), using the fulfilment of the momentum integral equation as a criterion to asses the two-dimensionality of the experiments. In the experiments considered to be satisfactorily two-dimensional, the linear spreading rates were found to fall within the range $dy_{1/2}/dx = 0.073 \pm 0.002$. The position of zero shear stress was concluded to be displaced from the position of maximum velocity, however the uncertainties in the turbulence statistics were reported to be high. In the experiments reviewed no near-wall peak in the energy was found. This was assumed to result from the strong influence of the free shear layer on the inner layer. In the study of Abrahamsson, Johansson & Löfdahl (1994), inner maxima were found in the experimental streamwise and lateral turbulence intensities, however the calculated kinetic energy did not possess an inner peak, only a tendency towards a plateau.

Schneider & Goldstein (1994) used LDV to measure turbulence statistics in a wall-jet at $Re = 14000$. They found the Reynolds stresses in the outer region to be higher than the previous data acquired using hot-wire measurements, which underestimated properties in this region. LDV was also used by Eriksson, Karlsson & Persson (1998), to perform highly resolved velocity measurements

in a wall jet of $Re = 9600$ all the way into the viscous sublayer, enabling direct determination of the wall shear stress. In accordance with other flows, scaling laws for the velocity and Reynolds stress profiles, have been sought for the plane wall jet. One first choice is to make use of the velocity and jet height at the inlet as the characteristic scales, but this does not lead to a collapse the data from different experiment in an convincing manner (see e.g. Launder & Rodi 1981). Using a different approach, Narashima, Narayan & Parthasarathy (1973) suggested that the mean flow parameters should scale with the jet momentum flux and the kinematic viscosity. The same approach was employed by Wygnanski, Katz & Horev (1992) in an effort to remove the inlet Reynolds number dependency and to determine the skin friction from the decrease in momentum flux. Wygnanski *et al.* (1992) also reported that the assumption of constant Reynolds stress in the overlap region does not hold for a wall jet. Irwin (1973) used a momentum balance approach, neglecting viscous stresses, to derive that in the case of jets a coflow, the ratio of the streamwise velocity to the coflow must be kept constant for strict self-similarity to be possible. Also for the wall jet in an external stream Zhou & Wygnanski (1993) proposed a scaling based on the work of of Narashima *et al.* (1973).

Concerning the wall jet in quiescent surroundings, George *et al.* (2000) performed a similarity analysis of the inner and outer part of the wall jet. Both the inner and outer region were reported to reduce to similarity solutions of the boundary layer equations in the limit of infinite Reynolds number, however for finite Reynolds numbers, neither inner nor outer scaling leads to a complete collapse of the data.

The task of computing solutions to the plane wall jet has proven to be challenging. Part of the problem arises from the combination of two distinct shear layers in the wall jet. Since the two regions interact strongly, many characteristics of wall jets differ from those of other canonical shear layers. Early computational efforts using RANS type methods are reviewed by Launder & Rodi (1983), more recent attempts are reviewed by Gerodimos & So (1997). Tangemann & Gretler (2001) proposed an algebraic stress model and compared it to the standard k–ϵ model and a full Reynolds stress model by computing a two-dimensional wall jet in an external stream. They found the algebraic and the Reynolds stress model, but not the $k - \epsilon$ model, to be able to produce a region of negative production of turbulent kinetic energy where the inner and outer shear layers interact. Dejoan & Leschziner (2005) performed a highly resolved large eddy simulation (LES) matching the experiments by Eriksson *et al.* (1998). The simulation was found to agree well with the experiments, also for the Reynolds stresses. By examining the budgets of the turbulent energy and Reynolds stresses, the turbulent transport was found to play a particularly important role in the region where the outer and inner layers overlap. The transition process was reported difficult to accurately reproduce in LES, and a defect in the wall-normal stress in the simulation was attributed to this difficulty.

Reports of direct numerical simulations (DNS) of wall jets, have up to recently been scarce, even more so for investigations providing time averaged statistics. Wernz & Fasel (1996,1997) employed DNS to investigate the importance of three-dimensional effects in the transition of wall jets. The breakdown of a finite-aspect-ratio wall jet was studied by Visbal, Gaitonde & Gogineni (1998). Recently Levin *et al.* (2005) studied a wall jet both experimentally and by means of DNS. In the simulation two-dimensional waves and optimal streaks corresponding to the most unstable scales were introduced in a wall jet at $Re = 3090$. The presence of streaks were found to suppress pairing and to enhance the breakdown to turbulence. In an extension to the previous work, Levin (2005) used the same forcing and a larger computational box to obtain turbulence statistics.

Despite the numerous investigations of wall jets, including theoretical, experimental simulation studies, the question of self-similarity and proper scaling is not fully understood. The reason for this originates in the existence of two different types of shear layers. Each of the layers have a distinct set of characteristics and scalings which excludes a full self-similarity of the wall jet. Presumably statistics close to the wall are governed by inner scales, in accordance to boundary layers, and likewise in the outer part, where some type of outer scales will be the appropriate ones. However, the definition of scalings is not clear, and may as well vary between different quantities.

The aim of the present investigation is to study the turbulent propagation of a plane wall-jet by means of direct numerical simulation. The study aims at increasing the knowledge of the dynamics and mixing present in this flow case. Presently, few simulations have been performed for this flow case, and this is to the authors' knowledge the first to include scalar mixing.

In the simulation an effort is made to provide efficient inlet disturbances in order to facilitate a fast and efficient transition to turbulence. The research is part of an ongoing project with the aim of studying turbulent combustion through DNS. Since realistic simulations of combustion involve heat release and considerable density fluctuations, the fully compressible formulation of the fluid dynamics problem is used.

In terms of dynamics characteristics, both mean development and fluctuations of the wall-jet are of interest. The mean development is characterized by investigating the jet spread rate and the decay of the streamwise velocity. The different properties of the inner and outer layers are investigated by applying different scalings in the respective layers. It is of interest to determine the different dynamical properties of these layers and to relate them to what has previously been found for other canonical shear flows, such as e.g. boundary layers and free shear flows. The different scaling approaches are also valuable in assessing to what extent the wall-jet can be considered self-similar. In terms of mixing, the wall jet provides an interesting flow case with implications for engineering applications, since it involves mixing in the vicinity of a wall. Mixing in this region is of importance for example in development and investigation

of combustion models for accurate predictions in the presence of a wall. For this reason scalar properties in the wall-jet in the inner and outer region of the wall-jet, such as scalings and self-similarity, is studied in analogy to those of the velocity field.

2. Governing equations

The equations governing conservation of mass, momentum and energy (see e.g. Poinsot & Veynante 2001) are

$$\frac{\partial \rho}{\partial t} + \frac{\partial \rho u_j}{\partial x_j} = 0, \tag{1}$$

$$\frac{\partial \rho u_i}{\partial t} + \frac{\partial \rho u_i u_j}{\partial x_j} = -\frac{\partial p}{\partial x_i} + \frac{\partial \tau_{ij}}{\partial x_j}, \tag{2}$$

$$\frac{\partial \rho E}{\partial t} + \frac{\partial \rho E u_j}{\partial x_j} = -\frac{\partial q_j}{\partial x_j} + \frac{\partial (u_i(\tau_{ij} - p\delta_{ij})}{\partial x_j}, \tag{3}$$

where ρ is the mass density of the fluid, u_i the velocity components, p is the pressure and $E = (e + 1/2 u_i u_i)$ is the total energy. The fluid is considered to be Newtonian with a zero bulk viscosity, for which the general form of the viscous stress is

$$\tau_{ij} = -\frac{2}{3}\mu \frac{\partial u_k}{\partial x_k}\delta_{ij} + \mu \left(\frac{\partial u_i}{\partial x_j} + \frac{\partial u_j}{\partial x_i} \right), \tag{4}$$

where μ is the dynamic viscosity. The heat diffusion is approximated using Fourier's law for the heat fluxes $q_i = -\lambda \partial T / \partial x_i$ where λ is the coefficient of thermal conductivity and T is the temperature. In the simulations a Prandtl number of

$$Pr = \frac{\nu}{\lambda/(\rho C_p)} = 0.72, \tag{5}$$

is used. The fluid is furthermore assumed to be calorically perfect and to obey the perfect gas law. The compressibility of the jet is parameterized by the Mach number. To keep the compressibility effects small, while maintaining reasonably large simulation time steps, a moderate Mach number is used. The inlet Mach number of the simulation is set to $M = U_{in}/a = 0.5$, where U_{in} is the velocity at the inlet and a is the speed of sound.

The mixing in the plane wall jet is studied by introducing a passive scalar in the simulations. The scalar is conserved i.e. no production or destruction of the scalar is present and the scalar is passive in the sense that the motion of the fluid is unaffected by the presence of the scalar. The equation governing the passive scalar concentration, θ, is (see e.g. Poinsot & Veynante 2001),

$$\frac{\partial \rho \theta}{\partial t} + \frac{\partial}{\partial x_j}(\rho u_j \theta) = \frac{\partial}{\partial x_j}\left(\rho \mathcal{D} \frac{\partial \theta}{\partial x_j} \right) \tag{6}$$

where $\mathcal{D}$ is the diffusion coefficient of the scalar. In the simulations the scalar diffusivity in terms of the Schmidt number is $Sc = \nu/\mathcal{D} = 1$.

3. Numerical method

3.1. *Spatial integration*

Spatial integration of the governing equations is achieved by employing a formally sixth order compact finite difference scheme for the first derivative (Lele 1992). In the non-periodic directions, schemes of reduced order are used at the nodes close to the boundary. At the node directly on the boundary, a one-sided third order scheme is used. At the consecutive node a central fourth order scheme is used.

3.2. *Temporal integration*

For the temporal integration an explicit Runge-Kutta scheme of third order is employed. The scheme is four stage, formulated in low-storage form and is presented in Lundbladh *et al.* (1999). During simulation the linear CFL number is kept constant, varying the time step.

3.3. *Computational domain*

The computational domain used in the simulations consists of a rectangular box. The physical domain size, in terms of the jet inlet height h, is $L_x/h = 47$, $L_y/h = 18$ and $L_z/h = 9.6$ in the streamwise, wall-normal and spanwise directions respectively. The inlet of the jet is positioned directly at the wall with the flow parallel to it. In the simulation, the streamwise and the wall-normal directions are non-periodic, while the spanwise direction is treated periodically.

3.4. *Grid stretching*

The computational domain is discretized using a structured grid. The number of nodes used in the simulation is $384 \times 192 \times 128$, in the streamwise, wall-normal and spanwise direction respectively, amounting to a total of 9.4×10^6 nodes. The grid employed is stretched in the wall-normal and the streamwise direction but uniform in the spanwise.

In the streamwise direction a third order polynomial is used to stretch the grid. The grid spacing is finest in the transition region of the jet, and coarsest at the outlet, maintaining a node separation of $10 < \Delta x^+ < 12$ in terms of wall units in the developed region used for turbulent statistics $15 \leqslant x/h \leqslant 40$. Also in wall units, the spanwise node separation decreases from $\Delta z^+(x/h = 15) = 8.2$ to $\Delta z^+(x/h = 40) = 5.5$ in the developed region.

In the wall-normal direction, the grid is stretched using a combination of a hyperbolic tangent and a logarithmic function. The combination allows for clustering of nodes close to the wall while maintaining a high resolution of the outer layer. In the inner region, the viscous sublayer, $y^+ < 5$, is always resolved with three or more nodes. In the outer layer the wall-normal node spacing equals that of the spanwise direction at a wall distance $y = 2.9h$.

3.5. *Filtering*

To avoid accumulation and growth of unresolved waves in the high wave number range, a low-pass filter is applied continuously to the scalar and velocity fields. Filtering of the fluid variables is performed every ten time steps using the explicit sixth order filter suggested by Lele (1992).

In an effort to prevent negative concentrations, owing to the dispersion errors of the numerical scheme, a second order filter is applied to the scalar concentration in the initial part of the domain, $x/h < 12$. The inlet region is filtered with a longer time interval of 300 time steps, to reduce the introduced numerical diffusivity of the low-order filter. In the rest of the domain the scalar is filtered using the same filter and the same filtering period as the fluid variables. This approach did reduce but not completely prevent negative scalar concentration. The second order filter completely avoids the creation of negative concentration in the initial region, downstream however, spots are still generated from vortices propagating into the zero scalar coflow. Resulting from the initial lower order filtering the magnitude of the appearing spots of negative concentrations are basically less than 3% of the inlet scalar concentration.

4. Inlet and boundary conditions

4.1. *Inlet profiles*

The inlet profiles used for the velocity and the scalar concentration are shown in figure 1. Both profiles are constructed using hyperbolic tangent functions. The velocity profile includes a coflow, parallel to the wall, positioned above the jet. The magnitude of the coflow is 10% of the jet inlet velocity, $U_c = 0.10U_{in}$, and is applied for computational efficiency reasons. Due to engulfing processes, large scale vortices are created in the outer part of the jet and propagate into the ambient flow. Without the coflow these structures are very persistent (see Levin 2005). The coflow ensures that the vortices can leave the domain without contaminating the statistics. The Reynolds number based on the inlet height h and velocity U_{in} of the jet is $Re = U_{in}h/\nu = 2000$. The inlet profile for the scalar concentration is finite at the wall and zero above the jet i.e. no coflow condition is used for the scalar. On the wall a no-flux condition, $\partial(\theta(y = 0))/\partial y = 0$, is used for the scalar.

4.2. *Inlet disturbances*

The aim of the simulation is to study properties of the turbulent wall jet.Therefore inlet disturbances are introduced to facilitate a fast transition to turbulence. For efficient transition, three types of disturbances are used in the present simulation, random disturbances of a prescribed length scale, streamwise vortices and periodic streamwise forcing. All disturbances are superpositioned at the inlet. The random disturbances are generated using a filter technique by Klein *et al.* (2003). The filter produces correlated disturbances with a length scale of $h/3$ and a root-mean-square magnitude of $0.05U_{in}$. In the investigation of Levin

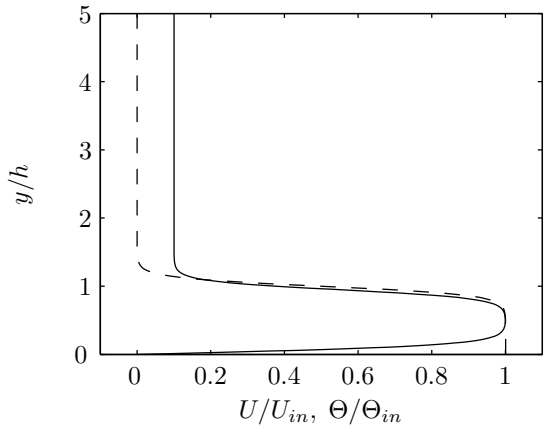

FIGURE 1. Inlet profiles for the velocity (solid) and scalar concentration (dashed).

et al. (2005) it was reported that streamwise streaks play an important role in the breakdown to turbulence in plane wall jets. In the light of this, streamwise vortices are added in the upper shear layer in the simulation. The amplitude of the vortices are $0.01U_{in}$. In the streamwise directions, a periodic disturbance composed of two harmonic functions, each with a maximum amplitude of $5 \times 10^{-3}U_{in}$ and a respective Strouhal number of 0.3 and 0.45.

4.3. *Top inflow condition*

At the top of the domain an inflow velocity is used to simulate entrainment of fluid by the jet. Since the domain is finite, the entrainment must be accounted for at the top of the domain, so that the jet development is not constrained. Integrating the stationary two-dimensional continuity equation from the wall out, an estimation of the mean inflow velocity can be found as

$$\frac{\partial \rho U}{\partial x} + \frac{\partial \rho V}{\partial y} = 0 \quad \Longrightarrow \quad \rho_\infty V_\infty = -\frac{\partial}{\partial x}\int_0^\infty \rho U dy = -\frac{\partial}{\partial x} M_x(x) \qquad (7)$$

where $M_x(x)$ is the streamwise mass flux. Using the data of Eriksson *et al.* (1998), the streamwise mass flux is found to increase linearly according to $M_u(x) \sim 0.031 M_x^0(x/h)$ in terms of the jet inlet mass flux M_x^0 and the slot normalized downstream distance. This leads to

$$V_\infty = -0.031 M_x^0/h\rho_\infty \qquad (8)$$

which has been used in the present DNS to prescribe the entrainment velocity at the top of the domain.

4.4. *Boundary zones*

In simulations where large non-linear disturbances are to pass the boundary with minimal reflection, such as at wall-jet outlet, it has previously been been

found necessary to add boundary zones or absorbing layers adjacent to the boundaries (see e.g. Colonius 2004). To minimize the reflection and generation of spurious waves at the boundaries, boundary zones in the manner of Freund (1997) are therefore used in the simulation. The zones consist of two additional terms, one convective and one dissipative, which are added smoothly to the equations in the vicinity of the inlet, the outlet and the top boundary. The thickness of the boundary zones are approximately h at the inlet, $2.5h$ at the outlet and $4h$ at the top. A more thorough description of the boundary zones is available in Ahlman *et al.* (2006).

5. Results

To account for the slight compressibility, the statistics from the simulation are computed using mass-weighted averaging, often referred to as Favre averaging. Assuming a variable f, the decomposition into a mean and fluctuating part is performed through,

$$f = \tilde{f} + f'' = \overline{\rho f}/\bar{\rho} + f'' \tag{9}$$

where ρ is the fluid density and the usual average is denoted by $\bar{f}$. The mass-weighted mean is conventionally denoted by $\tilde{f}$ and the corresponding fluctuation by f''. In the simulation results presented, mass-averaged variables are denoted by plain uppercase letters, e.g. $U = \tilde{U}$.

To accumulate statistics, the solution was sampled every 200 time steps corresponding to approximately $0.5t_j$, where $t_j = h/U_{in}$ is the jet inlet time scale. During sampling averaging is performed over all spanwise positions. The sampling was started at $t = 185t_j$ and continued for a duration of $t_{\text{samp}} = 309t_j$. The simulation was performed on a Linux cluster with dual 3.4 GHz Intel Xeon processor nodes, and an Infiniband Mellanox network for MPI traffic. The total computational time used was 22000 CPU hours.

5.1. *Scaling of flow variables*

The results from the simulation are presented using inner and outer scaling. When properties in the inner part of the jet are considered, a conventional boundary layer scaling will be applied in terms of the friction velocity $u_\tau = \sqrt{\tau_w/\rho}$ and the viscous length scale $l_* = \nu/u_\tau$. When properties of the outer region are considered, the velocity scale is assumed to be the excess velocity $(U_m - U_c)$, where U_m is the local maximum streamwise velocity and U_c the coflow velocity, in analogy to a free shear layer. The length scale applied in outer region is the half-width position $y_{1/2}$ which is the distance from the wall to the position where the mean velocity equals $\frac{1}{2}(U_m - U_c)$. For the scalar concentration a similar distinction of an inner and outer layer is not obvious. At the wall a no-flux condition is enforced in the wall-normal direction, hence prescribing the scalar gradient to be zero. A single concentration, the local maximum concentration Θ_m, is therefore used to scale the concentration in the inner and outer layers. It should be noted that from the scalar boundary condition, the mean concentration maximum occurs at the wall. The characteristic

length scales of the scalar are assumed to be in correspondence to the ones of the velocity field. In the inner region the viscous length scale is used and in the outer the scalar half-width $y^{\theta}_{1/2}$ is applied. The scalar half-width is defined as the distance from the wall to the position where the mean concentration is equal to half the maximum value, $\Theta(y^{\theta}_{1/2}) = \frac{1}{2}\Theta_m$.

5.2. *Flow structure*

Instantaneous plots from the simulation are presented in figure 2-4 to provide an insight into the dynamics of the flow and mixing. Figure 2 shows a snapshot of the streamwise velocity and the scalar concentration in an xy-plane. The transition process can be seen to start prior to $x/h = 5$ and to be rapid. Few coherent structures are seen prior to full transition, due to the strong and diverse inlet disturbances. Downstream of the transition the jet slows down and spreads in the wall-normal direction. The scalar is also dispersed in the wall-normal direction.

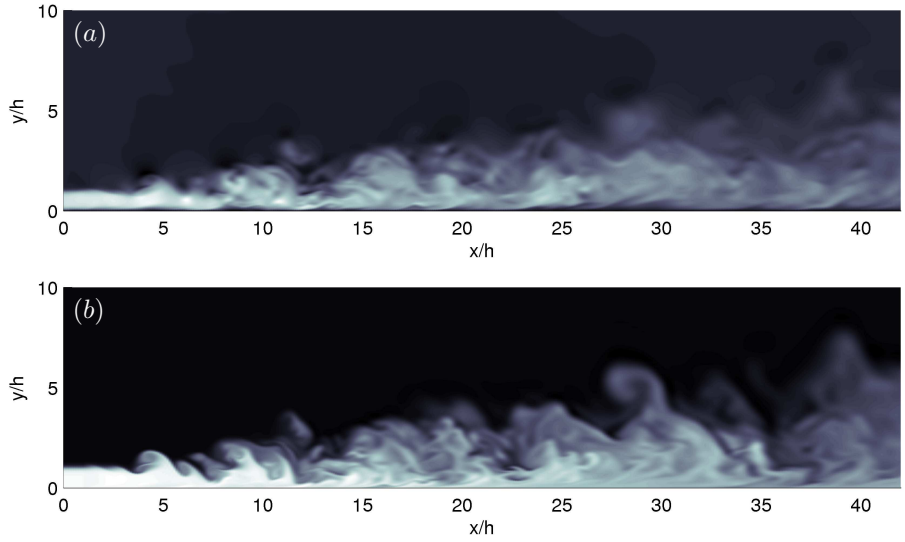

FIGURE 2. Instantaneous plots of the streamwise velocity, u (a) and the scalar concentration θ (b) in an xy-plane. For the velocity light areas represent positive values and dark negative, while for the scalar light areas represent finite concentration and dark areas correspond to zero concentration.

Instantaneous plots of the streamwise, u''/u_τ, and scalar fluctuation, θ''/Θ_m, in two cross flow planes (zy-planes) are shown in figure 3. The cross flow planes are positioned at $x/h = 20$ and at $x/h = 40$. Comparing the structures at the two positions, the length scales are seen to be larger further downstream, particularly in the outer part of the jet.

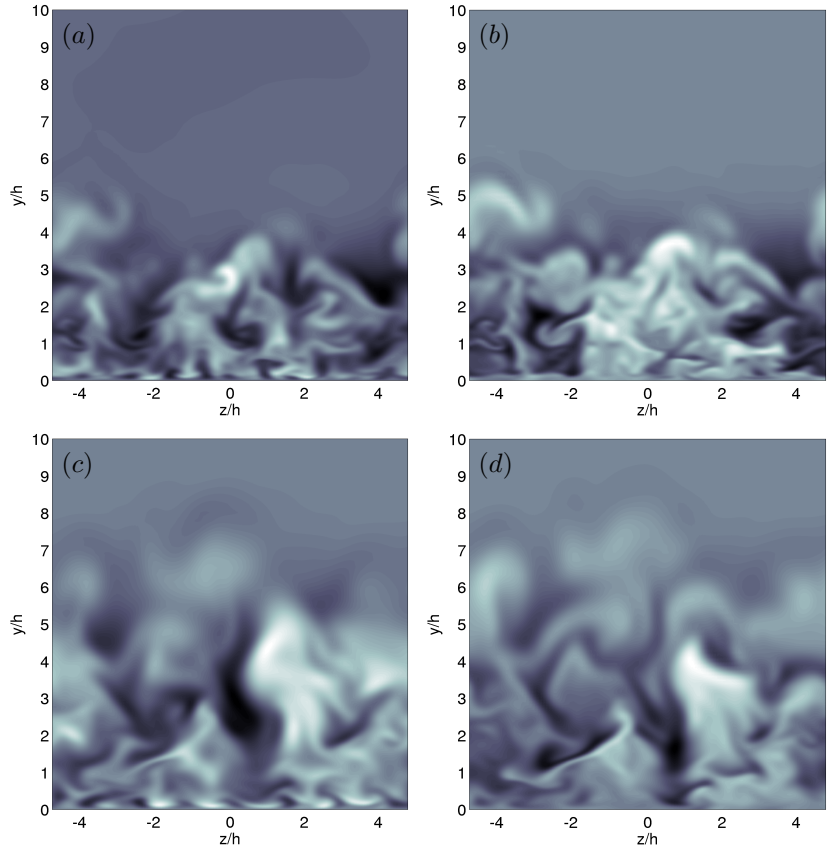

FIGURE 3. Instantaneous plots of the velocity fluctuation u''/u_τ (a) and (c) and the scalar fluctuation θ''/Θ_m (b) and (d) in two cross stream planes (zy-planes) at $x/h = 20$ (a) and (b) and at $x/h = 40$ (c) and (d). Light areas represent positive fluctuation values and dark negative.

In figure 4 instantaneous plots of the velocity and scalar fluctuations are shown in two xz-planes, one close to the wall, at $y^+ = 9$ and one in the outer region at $y/h = 0.95$. In the inner velocity plot, elongated streamwise streaks, typical of boundary layers are seen. These structures can also be seen close to the wall in figure 3. These structures are not seen in the scalar in the same region, which is probably due to the low scalar gradient close to the wall. In the outer layer region the structures are much more isotropic.

5.3. *Mean jet development*

The spatial development of the wall jet is presented in figure 5. By observing the friction velocity it can be seen that the inner layer exhibits a laminar

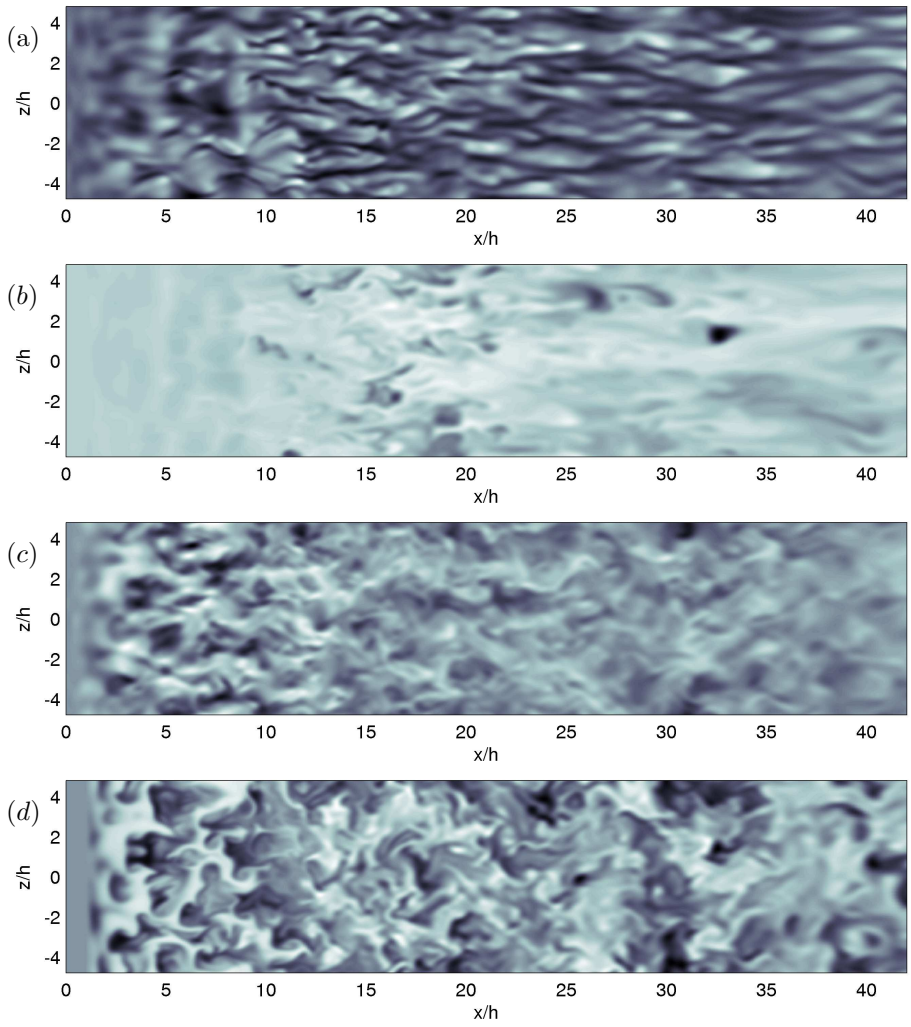

FIGURE 4. Instantaneous plots of the velocity fluctuation u''/u_τ (a) and (c) and the scalar fluctuation θ''/Θ_m (b) and (d) in an xz-plane at $y^+ = 9$ (top two) and an in xz-plane at $y/h = 0.95$ (lower two). Light areas represent positive fluctuation values and dark negative.

propagation from the inlet down to approximately $x/h = 4$. After this position the friction velocity increases, indicating transition to turbulence of the inner layer. The transition progresses downstream, to the next local extremum positioned approximately at $x/h = 11$. The wiggle noted in the friction velocity at the inlet is an artifact of the inlet boundary zone technique. The transition

process of the outer layer is less clear, judging by the half-width, which grows monotonically. Observing the outer layer in figure 4, the transition is seen to occur early in the outer region. Significant fluctuations are noted already at $x/h = 2$. Past $x/h = 11$ the jet half-width development is approximately linear, indicating self-similar growth. The maximum velocity U_m and the wall scalar concentration Θ_w remain virtually constant until the point of transition. In the region of concurrent inner and outer transition, $4 \leqslant x/h \leqslant 11$, they both exhibit a decrease. Downstream of $x/h = 15$ the mean properties in both the inner and the outer region appear to have evolved into a fully turbulent propagating wall jet. Concerning the transition, the mean properties in figure 5 together with the previous instantaneous plots are only able to give an overview of the transition processes in the plane wall jet. A more thorough study of the transition processes can be found in the investigation by Levin *et al.* (2005).

5.4. *Mean velocity and scalar development*

The downstream development of the mean streamwise velocity and the scalar concentration is depicted in figures 6-10. Profiles are plotted at positions downstream of the transition region. The positions corresponds to $x/h = 15$, 20, 30 and 40, and are the same positions that will be used for all statistics unless noted otherwise.

In figure 6, mean streamwise profiles are plotted using inner scaling. In the inner-most portion of the jet, very close to the wall, the profiles are found to be very well collapsed by the inner scaling. This region, where $y^+ = U^+$, corresponds to the viscous sublayer, present in boundary layers. Also in accordance to boundary layers, the velocity profile of the plane wall jet deviate from the viscous relation at a wall distance of $y^+ = 5$. In order to compare the inner region with that in a boundary layer, the simulation data of Skote *et al.* (2002) at $Re_{\delta^*} = 200$ is also added in the figure. It is found that our data and the boundary layer data agree well, in terms of the inner scaling, out to $y^+ = 13$. Further away from the wall, the profiles in figure 6 do not collapse indicating that inner scaling is not appropriate beyond this point.

As the inner-most part of the wall-jet closely resembles the viscous sublayer and buffer layer of a boundary layer, an inertial sublayer is presumed to exist further out from the wall, provided the Reynolds number is large enough. Logarithmic overlap regions have also been found in previous wall jet investigations e.g. by Wygnanski *et al.* (1992), Eriksson *et al.* (1998) and Dejoan & Leschziner (2005). The logarithmic region is however usually seen to be reduced in the wall-jets, Eriksson *et al.* (1998) report an overlap region of $30 \leq y^+ \leq 80$ for a wall jet of $Re_h = 9600$. In figure 6, a logarithmic region is plotted on the classical form $U^+ = \frac{1}{\kappa}\ln(y^+) + B$. The coefficients are chosen in accordance to the estimations in the experiments by Österlund (1999) ($\kappa = 0.38$, $B = 4.1$). No logarithmic region is however found in the streamwise profiles of the wall jet. The low Reynolds number, $Re_h = 2000$, evidently does not allow for large enough scale separation.

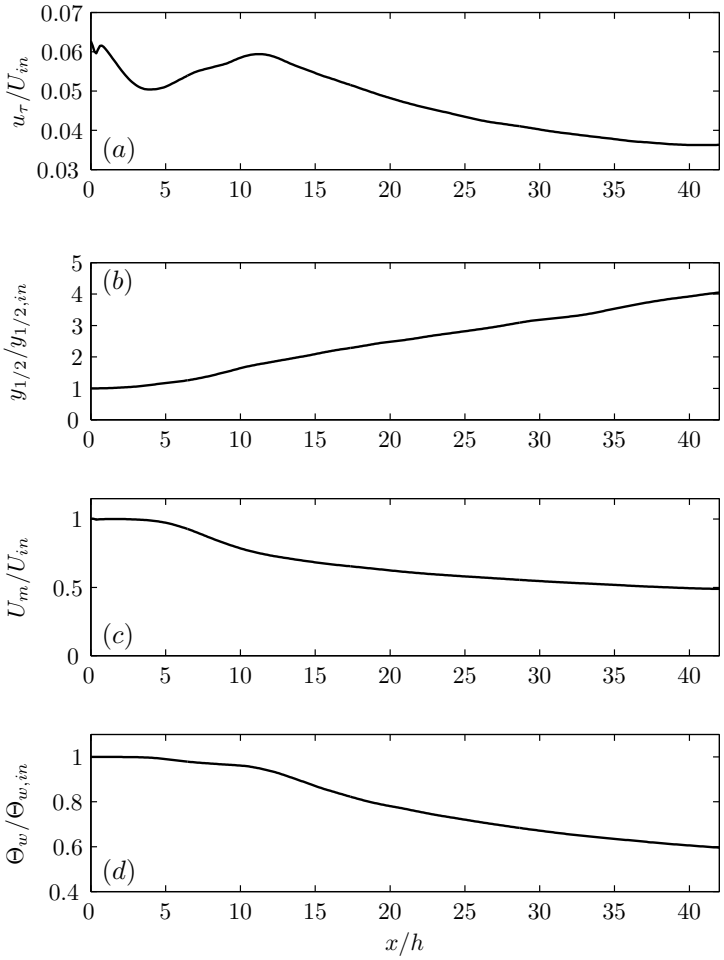

FIGURE 5. Downstream development of the wall jet; friction velocity u_τ/U_{in} (a), velocity half-width $y_{1/2}/y_{1/2,in}$ (b), maximum streamwise velocity U_m/U_{in} (c) and wall scalar concentration $\Theta_w/\Theta_{w,in}$ (d) normalized by the respective inlet conditions.

Since the inner scaling does not apply outside of $y^+ = 13$, an other scaling is used for the center region of the jet in figure 7. The wall distance is scaled with the half-width $y_{1/2}$ and the velocity is scaled with the local maximum velocity U_m. This is the conventional outer wall jet scaling and has previously been used to collapse profiles in wall-jets without coflow (Launder & Rodi 1981; Schneider & Goldstein 1994; Abrahamsson *et al.* 1994; Eriksson *et al.* 1998). Using this scaling the outer part of the inner layer, reaching out to the jet center, is seen to collapse.

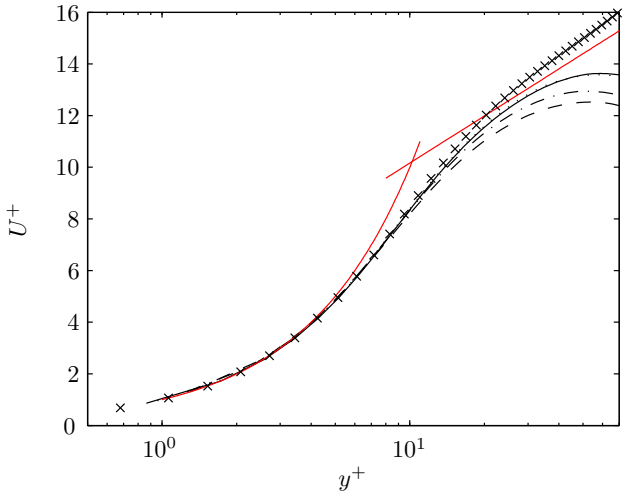

FIGURE 6. Mean velocity profiles in inner scaling ($U^+ = U/u_\tau$, $y^+ = yu_\tau/\nu$) at different downstream positions; $x/h = 15$ (dashed), $x/h = 20$ (dashed-dotted), $x/h = 30$ (dotted) and $x/h = 40$ (solid). The linear viscous relation $U^+ = y^+$, the logarithmic inertial relation $U^+ = \frac{1}{0.38}\ln(y^+) + 4.1$ and DNS data ($Re_{\delta^*} = 200$) from Skote *et al.* (2002) ($\times$) are also shown.

Using this scaling, the velocity profiles up to the point of maximum streamwise velocity collapse, except for the region very close to the wall where the inner scaling applies, as was seen before. The reason for the collapse is that the maximum velocity is positioned at a constant distance from the wall, in terms of the half-width. The maximum position is $y_m/y_{1/2} \approx 0.24$, which is significantly higher than the value 0.17 quoted by Eriksson *et al.* (1998) and the range $0.13 - 0.17$ by Launder & Rodi (1981). However the previous results were acquired for wall jets without external stream and at higher Reynolds numbers. Zhou & Wygnanski (1993) found the ratio $y_m/y_{1/2}$ to increase with the inlet coflow ratio from 0.16 at $U_c/U_m = 0$ to 0.31 at $U_c/U_m = 0.38$.

As is seen in the insert in figure 7, the conventional outer scaling fails to collapse the mean profiles far out from the wall, $y/y_{1/2} > 1$. This is an effect of the constant coflow. Figure 8 shows the streamwise velocity profiles in the outer layer, using an outer scaling adjusted for the coflow. The wall distance is scaled by $y_{1/2}$ and the velocity difference $(U - U_c)$ is scaled by the excess velocity of the outer layer $(U_m - U_c)$. This scaling was suggested by Zhou & Wygnanski (1993) for wall jets with a coflow, and yields a good collapse of the velocity profiles, also far out from the wal. The scaling corresponds to that used to collapse plane jets, indicating a similarity of the wall-jet outer region and the plane jet. Irwin (1973) used a classical momentum balance approach,

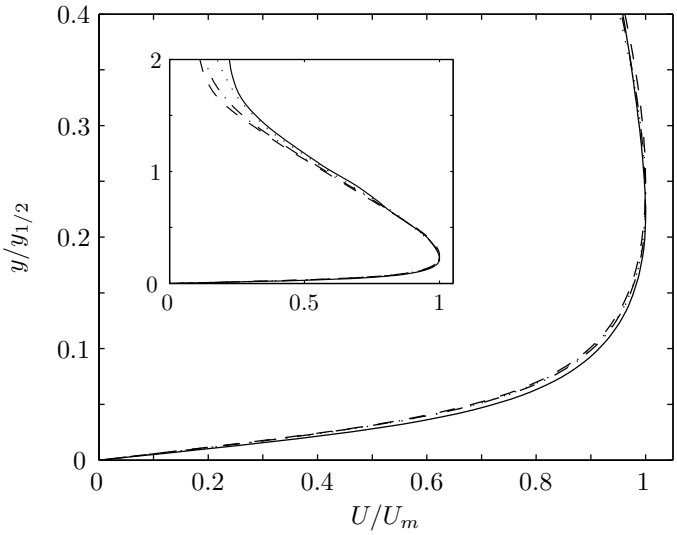

FIGURE 7. Mean velocity profiles using conventional outer scaling. Insert shows the full profiles using the same scaling. Lines as in fig. 6.

neglecting viscosity, to asses the self-preservation of the outer layer of a wall jet with a coflow. He concluded that in order for precise self-similarity, the velocity excess to the coflow ratio $(U_m - U_c)/U_c$ must be kept constant. Hence a constant coflow will generate a departure from self-similarity and also from linear half-width growth. The observation that the mean profiles of the outer layer are well collapsed therefore indicate that the magnitude of the constant coflow only causes a slight departure from self-similarity.

The downstream development of the wall-normal velocity is depicted in figure 9 using inner and outer scaling. The conventional wall units and friction velocity are used for the inner scaling, while for the outer scaling the half-width and the velocity defect $(U_m - U_c)$ are used to scale the wall distance and the velocity. The maxima of the wall-normal velocity are positioned approximately at $y = 0.7y_{1/2}$ which is further away from the wall than the maximum streamwise velocity position $y = 0.24y_{1/2}$ as shown i figure 7. The maximum wall-normal velocity is also found to decrease with downstream distance. From the inner scaling it can be seen that all but the last profile, $x/h = 40$, collapse fairly well in the inner layer $y^+ < 50$.

The mean scalar concentration is plotted in figure 10 using the scalar half-width $y^{\theta}_{1/2}$ to scale the wall distance. The concentration profiles are scaled by the maximum concentration. The employed scaling leads to a good collapse of the profiles, except for the $x/h = 40$ profile in the outer part of the jet. More samples are required for better convergence.

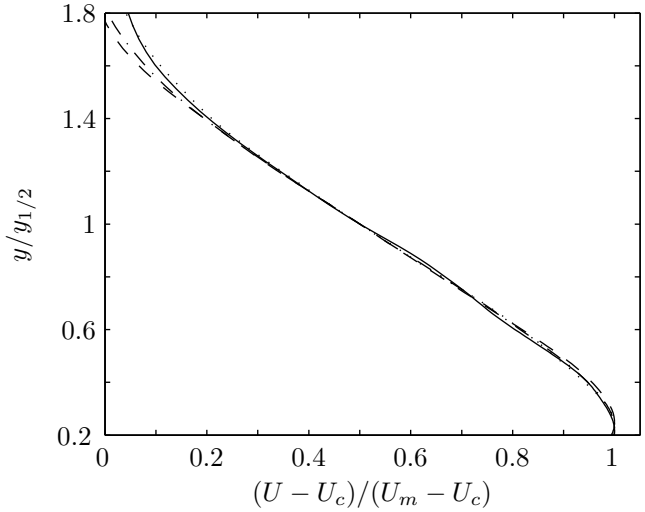

FIGURE 8. Mean velocity profiles in the outer shear layer, using an outer scaling adjusted for the coflow. Lines as in fig. 6.

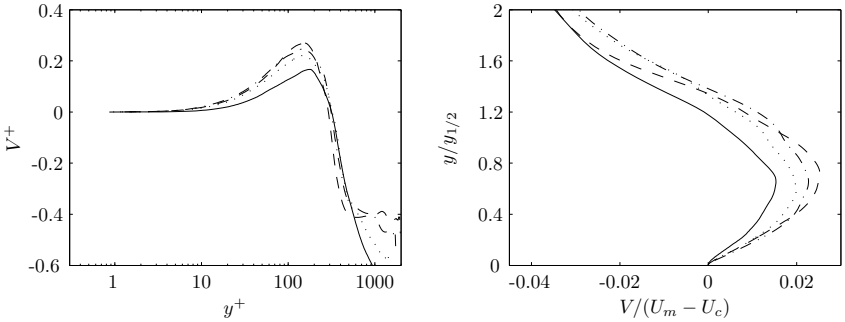

FIGURE 9. Mean wall-normal velocity profiles, using inner (left) and outer (right) scaling. Lines as in fig 6.

5.5. *Jet growth*

The growth rate is of profound importance, especially in engineering applications, because it characterizes the rate of momentum transfer and mixing by the jet. The commonly used measure of the growth rate is the downstream development of the half-width $y_{1/2}$. In figure 11 the half-width is plotted against downstream distance. Both the conventional growth, in terms of the half-width based on the velocity $y_{1/2}$, and the half-width of the scalar concentration $y^{\theta}_{1/2}$ are shown, as well as $y_{1/2}$ from the experiments by Eriksson *et al.* (1998). The virtual origin of the jet is positioned further downstream in the experiments by Eriksson *et al.* (1998) implying that there is a faster transition to turbulence in the DNS. It should be noted here that the inlet disturbances used in

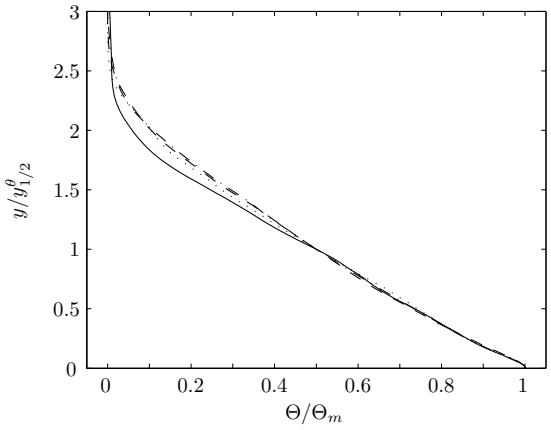

FIGURE 10. Mean scalar concentration using outer scaling. Lines as in fig. 6.

the simulation were not constructed to resemble the initial disturbances present in the experiments. From $x/h = 15$, the development of $y_{1/2}$ is approximately linear in the DNS. This is development is also found in self-similar plane jets. Presumably, for wall-jets of high Reynolds numbers, the momentum loss at the wall is not significant enough to generate a deviation from a linear development of the half-width. However, the growth rate of wall-jets is reduced. Rodi (1975) reported the rate of growth rate to be more than 30% less than that of a plane free jet. Launder & Rodi (1983) proposed that the reduction is a consequence of the damping of turbulent structures in the wall-normal direction.

Fitting a linear relation, using values from $x/h = 15$ to $x/h = 40$, yields a half-width growth rate of $dy_{1/2}/dx = 0.068$ for the simulation. This is lower than both the growth rate measured by Eriksson *et al.* (1998) $dy_{1/2}/dx = 0.078$, and the range given in the review by Launder & Rodi (1981) $dy_{1/2}/dx = 0.073 \pm 0.002$. The lack of universality using slot scaling is well known from previous wall jet studies (see e.g. Tailland & Mathieu 1967; Wygnanski *et al.* 1992; Zhou & Wygnanski 1993). The difference in growth rate can be attributed to the differences in Reynolds number and the use of a coflow in the simulation. A decrease in half-width growth for increasing Reynolds number was found by Wygnanski *et al.* (1992) and Abrahamsson *et al.* (1994). The presence of a constant external stream was found by Zhou & Wygnanski (1993) also to decrease the half-width growth.

Concerning the spread of the scalar, the growth rate of the scalar half-width is approximately equal to that of the velocity. This is in contrast to the corresponding property in plane jets, where the downstream scalar growth rate is greater than the velocity based growth rate (Davies *et al.* 1974; Ramparian & Chandrasekhara 1985; Stanley *et al.* 2002). The reason for this difference in behavior of the wall-jet mixing is assumed to be the damping of fluctuations

in the wall normal direction, but also the shift of the outer layer, out from the maximum scalar position.

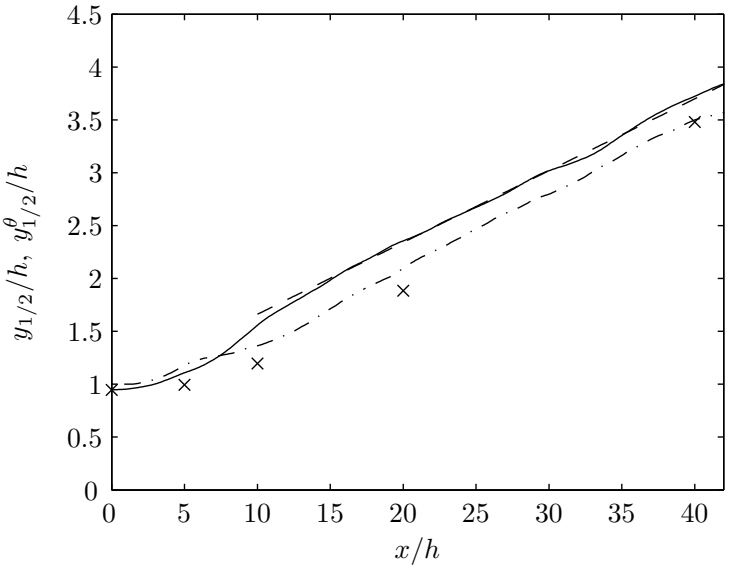

FIGURE 11. Wall jet growth rate; velocity half-width $y_{1/2}/h$ (solid), linear fit (dashed), scalar half-width $y^{\theta}_{1/2}$ (dash-dotted) and experimental values for the velocity half-width by Eriksson *et al.* (1998) ($\times$).

In figure 12a, the ratio $(U_{in} - U_c)^2/(U_m - U_c)^2$ is plotted as a function of x/h. This quantity is expected to be approximately linear, from the resemblance of a plane jet, where from self-similarity the maximum velocity decay is $U_m \approx 1/\sqrt{x}$.

The more abrupt transition of the simulation is again evident. The streamwise decay ratio adjusts to an approximately linear relation already at $x/h = 15$, whereas in the experiments this happens at larger x/h values. The growth rate is increasing up to about $x > 70x/h$, after which the linear growth rate is close to that of the simulation. This suggests that the transition in the simulation is very efficient and that the experiments becomes fully turbulent significantly further downstream.

The growth of the outer layer is further characterized in figures 13 and 14. In the first, the ratio of the outer length scale $y_{1/2}$ to the inner viscous length scale $l^* = u_\tau/\nu$ is plotted. The ratio is seen to increase drastically in the transition region, caused by the rapid increase in u_τ in this region. Throughout the rest of the domain the ratio increases from $y_{1/2}/l^* = 217$ at $x/h = 15$ to $y_{1/2}/l^* = 270$ at $x/h = 40$. This implies that, when the jet evolves, the characteristic length scale of the outer layer grows faster than the corresponding

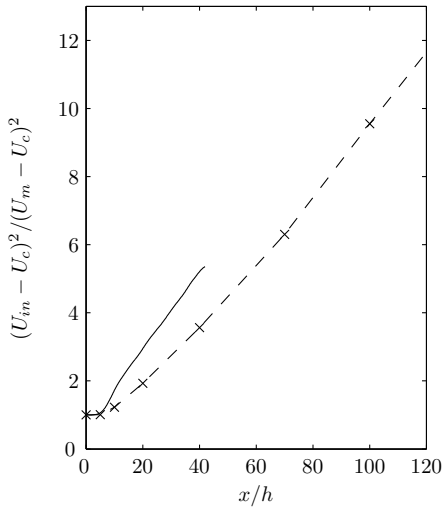

FIGURE 12. Decay of streamwise mean velocity against downstream distance. Simulation (solid) and experimental data by Eriksson *et al.* (1998) ($- \times -$).

inner length scale of the boundary layer. In figure 14 the growth of the outer Reynolds number $Re_o = U_m y_{1/2}/\nu$ is depicted, which over the domain is seen to become twice as high as at the inlet. The development is found to be lower than linear. Because the half-width growth is close to linear and the square of the velocity excess was found to be inversely proportional to the downstream distance, the outer Reynolds number should grow roughly as the square root of x/h.

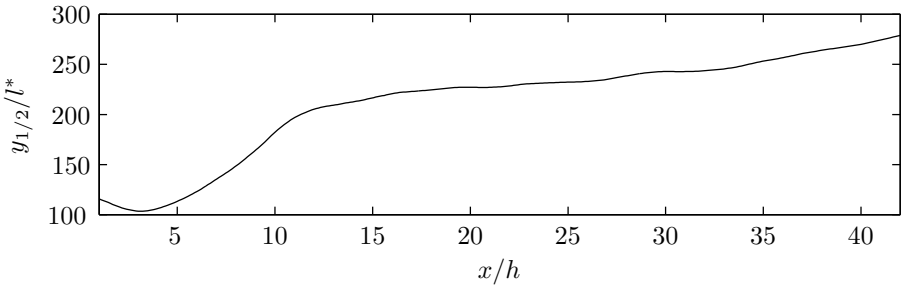

FIGURE 13. Length scale relation $y_{1/2}/l^*$, where $l^* = u_\tau/\nu$

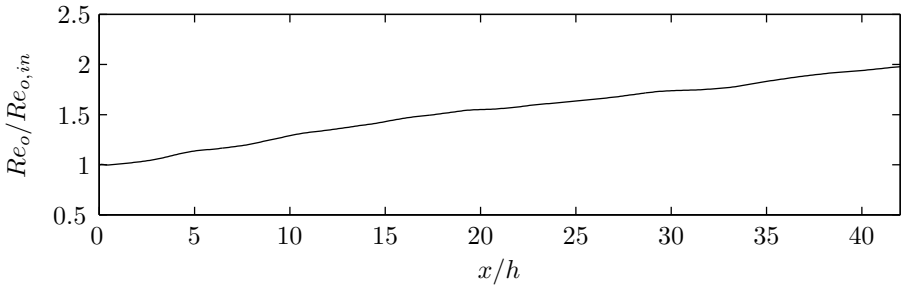

FIGURE 14. Outer Reynolds number $Re_o = U_m y_{1/2}/\nu$ normalized by the inlet condition.

5.6. *Fluctuations*

Velocity fluctuation intensity from the simulation are presented in figures 15-17. Both inner and outer scaling are used in order to elucidate characteristic properties of the different layers. The fluctuations are also compared to the data of Eriksson *et al.* (1998). The fluctuation intensities presented are root-mean-square values of the Favre fluctuation term defined in (9). Given the collapse of the mean velocity profiles and also the good agreement with boundary layer data in terms of inner scales up to $y^+ \approx 13$, we might expect to see a similar behavior for the fluctuations in the same range.

Figure 15 shows the individual intensitites and the turbulent kinetic energy in inner scaling. The impact of the wall on the wall-normal fluctuations can clearly been seen. The wall-normal component has a single peak, positioned in the outer layer. Close to the wall the wall-normal fluctuations are significantly smaller than the other components leading to a strong anisotropy. The profile of the streamwise velocity component u'' on the other hand has two separate peaks, in the inner and outer layers respectively. The inner peak is positioned at $y^+ = 13$, which is in good agreement with zero pressure gradient boundary layers (Österlund 1999). The maximum value of u^+ in the inner layer is approximately $u^+ = 2.4$. This is in agreement with Spalart (1988), who found a maximum value of $u^+ = 2.51$ in a boundary layer of $Re_\theta = 300$.

The minimum of the streamwise fluctuation between the two peaks is positioned at $y^+ = 50$, corresponding to the U_m position (see fig. 6), where the production due to mean shear vanishes. Both u'' peaks are of the same magnitude in contrast to the experiments performed at higher Reynolds numbers (e.g. Eriksson *et al.* 1998; Abrahamsson *et al.* 1994), where the streamwise intensity is higher in the outer region.

The spanwise fluctuation intensity is found to be of yet another character. In this direction the inner peak is absent, instead a plateau is formed reaching from the inner peak position in u'' approximately out to the U_m position. In the outer part the w'' intensity distributions are similar to those of the other

components. Comparing the outer layer parts of the intensity profiles, they all have a peak close to $y^+ = 200$. Regarding scaling in the inner boundary layer part, $y^+ < 13$, both the u'' and v'' profiles collapse well. The amplitude of the outer peak is also collapsed by the inner scaling.

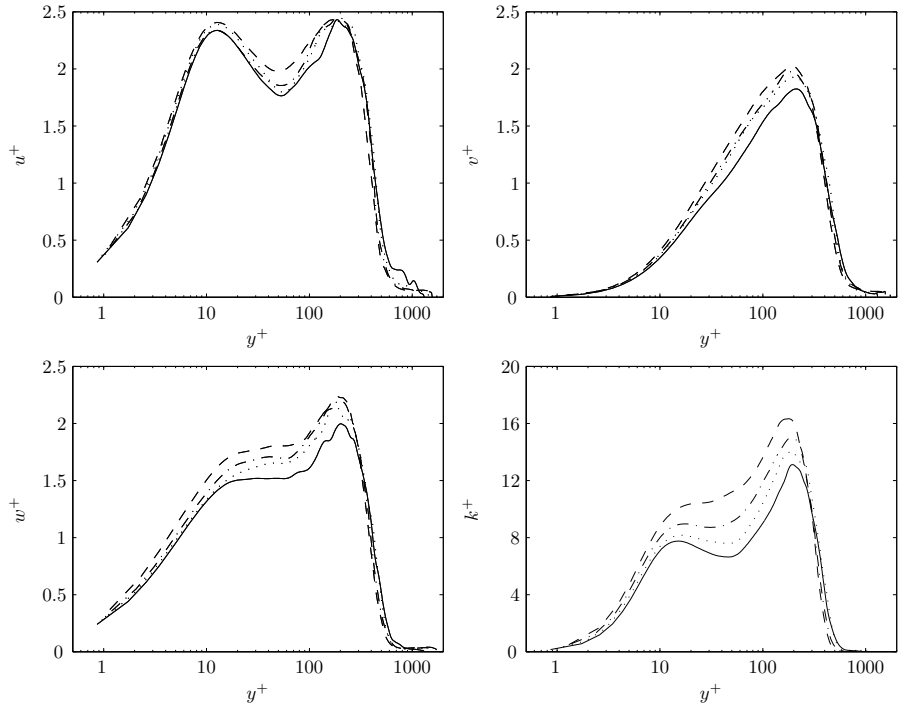

FIGURE 15. Streamwise (u^+), wall-normal (v^+) and spanwise (w^+) velocity fluctuation intensities, and the turbulent kinetic energy ($k^+ = k/\frac{1}{2}\bar{\rho}u_\tau^2$), using inner scaling. Lines as in fig. 6.

The turbulent kinetic energy decreases with downstream distance in terms of the inner scaling as shown in figure 15. At $x/h = 15$ the profile of k has only one peak in the outer part, but further downstream also a peak in the inner part of the jet appears. This behavior is most likely owing to the moderate length scale separation, in the inner and outer shear layers, for the present simulation at $Re = 2000$. As the wall jet progresses donwstream, the length scale ratio increases, as was seen in fig. 13, increasing the distinction between the two layers.

In figure 16 the turbulence intensity, u''_{rms}/U, using local quantities u'' and U, is plotted using inner scaling of the wall-normal distance. This property has previously been shown to be constant in the viscous sublayer up to about $y^+ = 5$. Alfredsson *et al.* (1988) found the value 0.4 in both turbulent boundary layers and channel flows. This value seems to approximately hold also for the

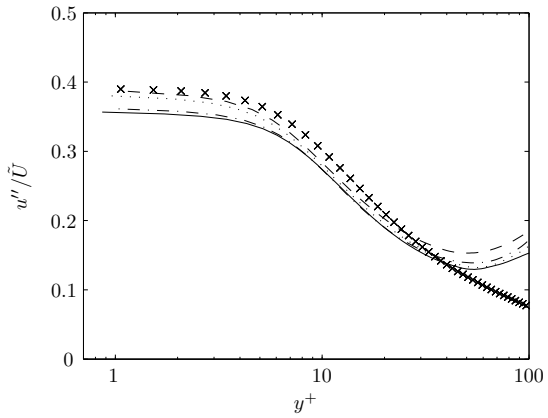

FIGURE 16. Near-wall behavior of the turbulence intensity u''_{rms}/U. Line as in fig. 6. Simulation data by Skote *et al.* (2002) $Re_{\delta^*} = 200$ ($\times$).

turbulent wall jet. The profiles all approach values in the range of $0.35 - 0.39$ in the viscous sublayer. As a comparison, the data of Skote *et al.* (2002) for $Re_{\delta^*} = 200$ has been added in the figure. In conclusion, the inner part of the wall jet closely resembles the corresponding region in zero pressure gradient boundary layers.

The turbulent fluctuation intensities and the turbulent kinetic energy in outer scaling are plotted in figure 17. The outer peaks of the are positioned approximately at $y = 0.8y_{1/2}$.

In agreement with other typical turbulent shear flows, the streamwise component is found to be larger than the other two components, which are of comparable magnitudes. The peak value of the fluctuations are found to agree reasonably well with what has been reported in the self-similar region of plane jets (see e.g. Gutmark & Wygnanski 1976; Thomas & Prakash 1991; Ramparian & Chandrasekhara 1985; Stanley *et al.* 2002). The maximum streamwise intensity $u''_{rms}/(U_m - U_c)$ is about 0.22 which is close to the range $0.24 - 0.3$ observed in the aforementioned studies. In the wall-normal and spanwise directions the intensity decreases slightly downstream and attains values between $0.19 - 0.17$ and $0.21 - 0.18$ respectively. This is in good agreement with Gutmark & Wygnanski (1976) who found values of about 0.19 and 0.20 for the corresponding components. Hence, we may conclude that the properties in the outer layer of the plane wall-jet outer layer closely resemble the properties of a plane jet.

The profiles of all the fluctuation components collapse fairly well, except the profile furthest downstream, $x/h = 40$. It is possible that the number of samples is not large enough to obtain well converged statistics at this position since the characteristic time scale of the outer layer increases.

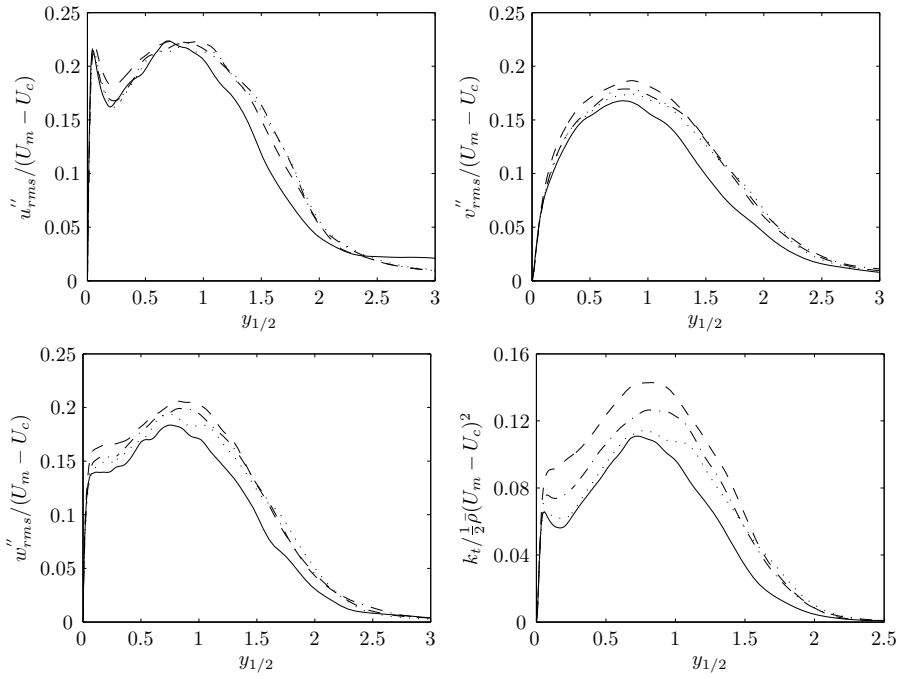

FIGURE 17. Streamwise $(u''_{rms}/(U_m - U_c))$, wall-normal $(v''_{rms}/(U_m - U_c))$ and spanwise $(w''_{rms}/(U_m - U_c))$ velocity fluctuations, and the turbulent kinetic energy $(k_t/\frac{1}{2}\bar{\rho}(U_m - U_c)^2)$, using outer scaling. Lines as in fig. 6.

The streamwise and wall-normal velocity fluctuation intensities from the simulation are compared to the experimental results of Eriksson *et al.* (1998), using inner and outer scaling in figure 18. It was previously shown that the transition to turbulence was different in the simulation and the experiments. Therefore profiles from positions downstream of the observed transition are compared. Hence, profiles from $x/h = 30$ from the simulation are compared with the experimental data acquired at $x/h = 70$. Using inner scaling, the widths of the simulation profiles are less than those in the experiments, because of the lower Reynolds number. Comparing the inner layer, the intensity of the velocity fluctuations is lower in the simulation, in particular in the streamwise component. Also this could be interpreted as a Reynolds number effect. In outer scaling, the fluctuations are found to agree well, with the exception of positions far out from the wall, where the experimental fluctuations are larger.

The wall jet Reynolds shear stress is shown in figure 19, using inner and outer scaling. Symbols are added marking the U_m and $y_{1/2}$ positions. The inner negative peaks at different downstream positions collapse using inner scaling and have a minimum of magnitude of $uv^+ = -0.56$, at $y^+ = 18$ The

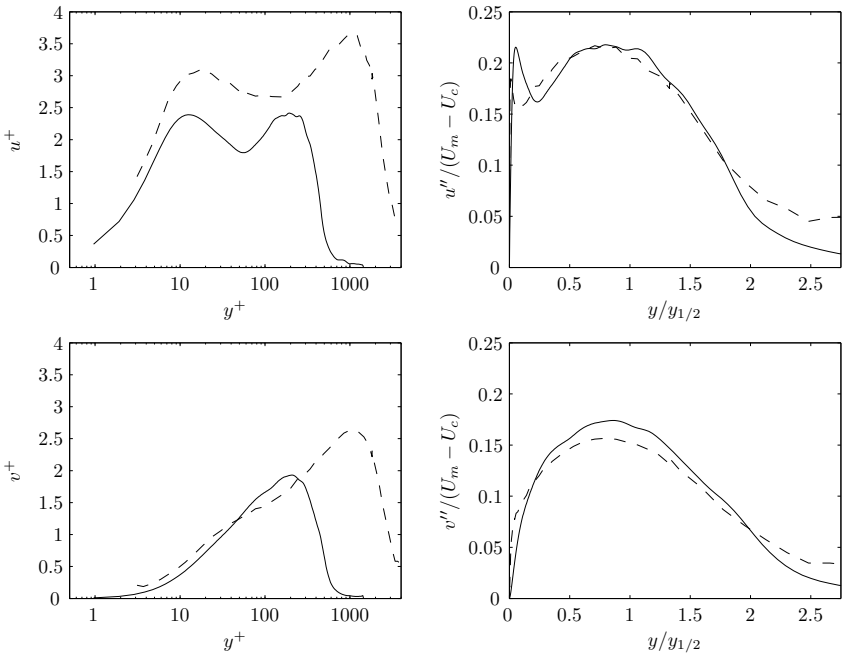

FIGURE 18. Streamwise and wall-normal velocity fluctuation comparison, using inner (left) and outer (right) scaling. Simulation profiles at $x/h = 30$ (solid) and experiments by Eriksson *et al.* (1998) at $x/h = 70$ (dashed).

outer maxima are positioned at approximately $0.8y_{1/2}$, slightly inside of the half-width, which was also seen in figure 17.

The position of vanishing Reynolds stress does not coincide with the U_m position. This is a well known property of wall jets and is evidence of the outer layer interaction with the inner layer. One interpretation of the this phenomenon is that the Reynolds stress is transported from the outer to the inner layer, possibly due to the larger length scales present in the outer layer. In the simulation the Reynolds stress vanishes in the range of $43 \leqslant y^+ \leqslant 49$ for the downstream distances profiles plotted in the figure, while the maximum position occurs in the range of $51 \leqslant y^+ \leqslant 59$. The positions are slightly increasing with downstream distance. George *et al.* (2000) proposed that the Reynolds stress should scale with the friction velocity squared, u_τ^2, also in the outer layer. It is not possible to asses this suggestion from the present data.

5.7. *Scalar fluctuations and fluxes*

Profiles of the intensity of the scalar fluctuations θ''_{rms} are plotted in figure 20 in terms of wall units and the scalar half-width $y^\theta_{1/2}$. The local maximum concentration, occuring at the wall, Θ_m is used to scale the intensity. In the

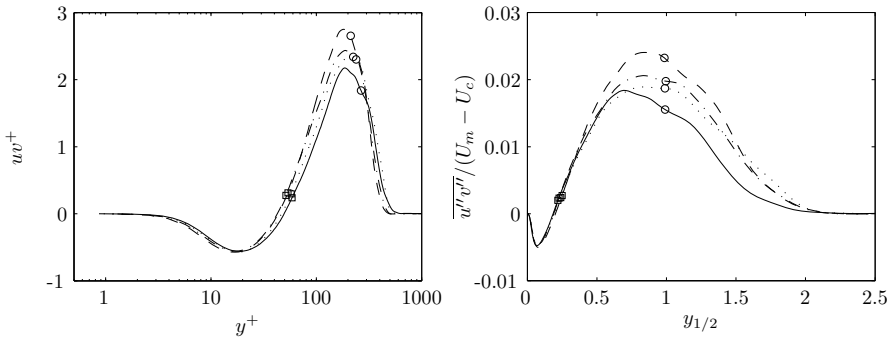

FIGURE 19. Reynolds shear stress using inner (left) and outer scaling (right). Symbols mark the U_m (□) and $y_{1/2}$ (○) positions. Lines as in fig. 6.

near-wall region, the scalar θ''_{rms}/Θ_m is constant in the wall-normal direction. This is a direct effect of the zero gradient boundary condition on the wall. The maximum concentration however does not collapse the intensity in the inner region. The scalar fluctuation intensity increases outside of $y^+ = 5$, i.e. outside the viscous sublayer, and has a maximum intensity near $y = y^{\theta}_{1/2}$. In the outer region, the intensity is fairly well scaled by the maximum concentration and the scalar half-width. The scaled maximum intensity is found to be fairly constant, $\theta''_{rms} \approx 0.18\Theta_m$, throughout a significant part of the outer layer $y_m < y < 1.5y_{1/2}$. The maximum intensity is in good agreement with what is reported for a plane jet by Davies *et al.* (1974), $\theta'' \approx 0.19\Theta_m$. In a round jet, the corresponding intensity is found to be higher. Panchapakesan & Lumley (1993) reported a value of 0.26 and Chevray & Tutu (1978) found approximately 0.24.

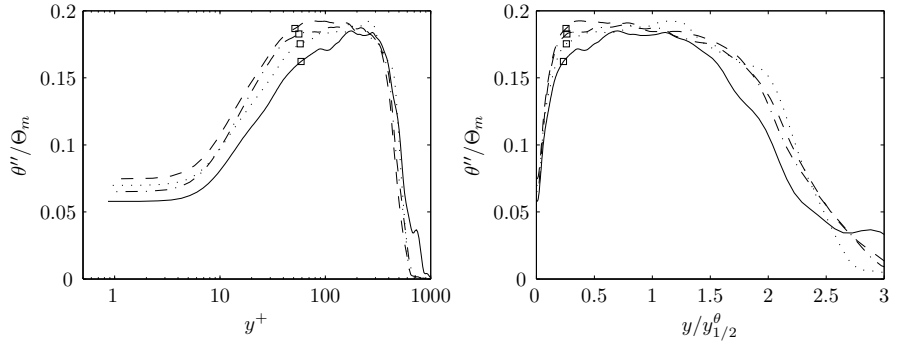

FIGURE 20. Root-mean-square of the scalar fluctuation using inner (left) and outer (right) scaling of the wall distance. Symbols (□) mark the U_m positions. Lines as in fig. 6.

The streamwise and wall-normal scalar flux profiles are plotted in figure 21. Inner and outer scaling is used for the velocity and the wall distance. Furthermore Θ_m is used for scalar scaling both in the inner and the outer layer, as was done for the scalar intensity. The wall-normal flux is with the present initial and boundary condition of course always positive. The outer peaks, in both fluxes, are centered approximately around the scalar half-width $y = y^{\theta}_{1/2}$.

The streamwise flux profile attains negative values close to the wall and larger positive values in the outer layer. The inner negative flux is found to increase in extent in the downstream direction. The non-zero streamwise scalar flux implies that the scalar flux vector is not aligned with the mean scalar gradient, which approximately is pointing in the wall normal direction. The origin of this miss-alignment of the scalar flux vector is the interaction of the velocity and scalar fluctuations This can be visualized by writing the production of streamwise scalar flux in a plan shear layer, neglecting streamwise mean development (see e.g. Wikström *et al.* 2000)

$$P_{\theta x} = -\overline{uv}\frac{\partial \Theta}{\partial y} - \overline{v\theta}\frac{\partial U}{\partial y} \tag{10}$$

which includes two finite components, for any shear flow including a mean scalar gradient in the direction of shear. The implication of the finite streamwise scalar flux, in terms of modeling, is that accurate predictions require a more advanced scalar flux model than the standard gradient based model (see e.g. Wikström *et al.* 2000).

The scalar flux in the streamwise and wall-normal directions are of comparable magnitudes and of about 0.019. For a plane jet, Ramparian & Chandrasekhara (1985) found the equivalently normalized streamwise and wall-normal fluxes to be 0.024 and 0.018 and in a round jet, Panchapakesan & Lumley (1993) found the corresponding fluxes to be about 0.031 and 0.21.

6. Conclusion

Simulation of a plane compressible wall-jet in a constant coflow, including the mixing of a passive scalar was performed. Statistics from the simulation were computed and analyzed in order to study the dynamics and mixing properties in the present flow case. The statistics were compared to what has been reported experimentally for wall-jets as well as for other wall bounded and free shear flows. In the simulation an effort was made to introduce efficient inlet conditions for a fast transition to turbulence. This was achieved by superposition of three types of disturbances, random disturbances correlated in space and time, streamwise vortices positioned in the upper shear layer and streamwise harmonic forcing. The disturbances triggered transition to start at about $x/h = 3$ and turbulent development of the entire jet was considered from $x/h = 15$ and downstream. In terms of mean development of the jet, the growth rate of the jet was found to be approximately linear according to $dy_{1/2}/dx = 0.068$. Also the maximum velocity decay, in terms of $(U_{in} - U_c)^2/(U_m - U_c)^2$, was found to be approximately linear. To elucidate properties in the inner and outer shear

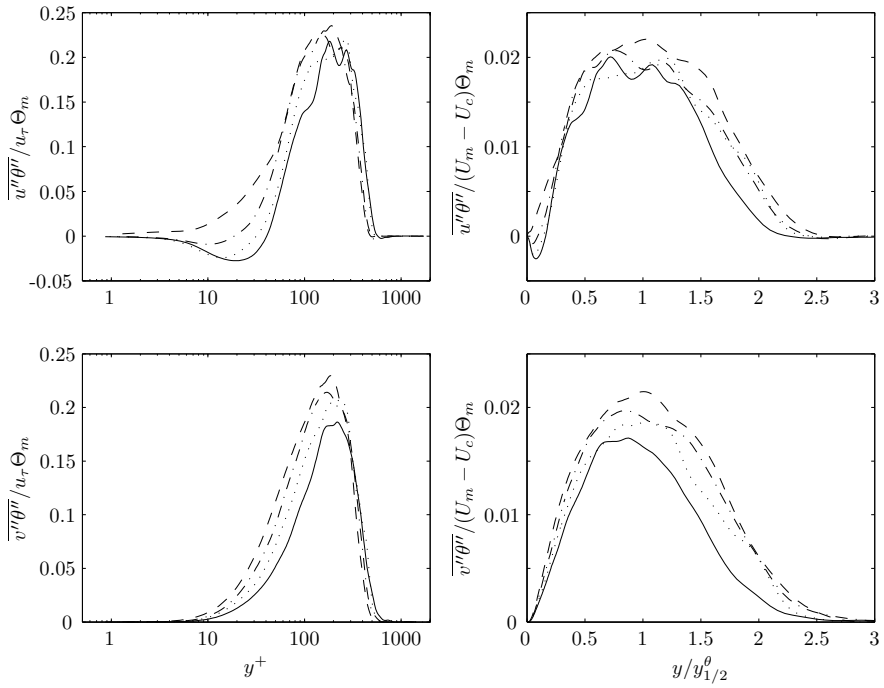

FIGURE 21. Streamwise and wall-normal scalar flux using inner (left) and outer (right) scaling. Lines as in fig. 6.

layers of the wall-jet, inner and outer scaling was employed. The inner scaling applied corresponded to the boundary layer scaling, in terms of plus units, and the outer scaling in employed the velocity half-width and the outer excess velocity $(U_m - U_c)$.

The inner part of the wall-jet, out to approximately $y^+ = 13$, was found to closely resemble a turbulent zero pressure gradient boundary layer. In the inner part, the mean and fluctuation profiles collapses, using inner scaling, a viscous sublayer is present out to $y^+ = 5$, also the maximum streamwise fluctuation position and magnitude agree well with what is found in a boundary layer. In the viscous sublayer, the local turbulence intensity becomes constant in resemblance to boundary layers and channel flows.

The outer layer, from the position of maximum mean streamwise velocity and out, resembles a free plane jet. The mean and fluctuation profiles in this region scale with the employed outer scaling. The outer maximum fluctuation magnitudes agree well with the wall-jet experiments by Eriksson *et al.* (1998) and also reasonable well with data from plane jet experiments.

The downstream growth rate of the scalar, in terms of the scalar half-width, was found to be approximately equal to the growth rate based on the velocity half-width. Hence scalar and momentum are spread in the wall normal

direction at a corresponding rate, in contrast to plane jets where the scalar is reported to exhibit a greater spread rate. Concerning the scaling of the passive scalar, the mean concentration when scaled by the maximum concentration and the scalar half-width, collapses over the entire profile. The scalar fluctuation is constant in the viscous sublayer, owing to the boundary and initial conditions used. No appropriate inner scaling for the fluctuation was however found, which is not surprising since a zero-gradient wall boundary condition was used for the scalar.

The maximum scalar fluctuation in the outer layer corresponds to that present in a free plane jet. The streamwise and wall-normal scalar fluxes were found to be of comparable magnitude, implying that the scalar flux vector differs significantly from the mean scalar gradient direction.

Appendix A. Inlet conditions

A.1. *Inlet profiles*

The inlet velocity consists of a composite profile constructed from three individual parts, an inner profile from the wall out U_w, a jet center profile U_c and an outer profile U_t containing the top of the jet and the above coflow region. The full profile U_{inlet} is defined as

$$U_{\text{inlet}}(y) = \begin{cases} U_w(y) & 0 \leqslant y \leqslant y_{c1} \\ U_c(y) & y_{c1} \leqslant y \leqslant y_{c2} \\ U_t(y) & y_{c2} \leqslant y \leqslant L_y \end{cases} \tag{11}$$

with connecting points beneath, $y_{c1} = 0.46h$, and above the jet $y_{c2} = 0.54h$. At the connecting points the functions are curve fitted to be continuous and to preserve the first derivatives. For the inner and outer profiles hyperbolic tangent profiles of the same form are used while the connecting center profile is a second order polynomial. The individual profiles are prescribed according to

$$U_w(y) = U_{in} \tanh\left[G(\sqrt{(y-c)^2} - \frac{w}{2})\right] \tag{12}$$

$$U_c(y) = -A_c y^2 + B_c y + C_c \tag{13}$$

$$U_t(y) = \frac{U_{in}}{2}\left(\left(1 + \frac{U_c}{U_{in}}\right)\left\{1 - \tanh\left[G_t\left(\sqrt{(y-c_t)^2} - \frac{w_t}{2}\right)\right]\right\}\right) \tag{14}$$

where G and G_t determine the profile gradients, c and c_t the jet center and w and w_t the width of the inner and outer *tanh* profiles. The jet width and center position are assigned when creating the inner profile. The gradient G is determined through specification of an estimated U^+ at the jet center. The value used $U^+ = 16$ is half that used in the experiments by Eriksson *et al.* (1998). The constants for the center profile (A, B & C) are set by specifying the jet center and by fitting the value and derivative to correspond to the ones of the inner profile at y_{c1}. For the outer profile the center is chosen in accordance to the inner profile $c_t = c$, and the width w_t and gradient G_t are determined through fitting the function value and derivative to correspond to

those of the center profile at the outer connecting point y_{c2}. On the wall a no-slip condition, $u_i(y=0)=0$, is used for the velocities.

The inlet shape of the passive scalar is prescribed by a hyperbolic tangent profile

$$\theta_{\text{inlet}}(y) = \frac{\theta_{in}}{2}\left\{1-\tanh\left[G_\theta\left(\sqrt{y^2}-h_\theta\right)\right]\right\} \tag{15}$$

where θ_{in} is the inlet scalar concentration at the wall. The profile steepness is specified in accordance to the outer velocity profile $G_\theta = G_t$ and the scalar inlet height is set to the jet height $h_\theta = h$. The resulting profile is finite at the wall and zero above the jet i.e. no coflow condition is used for the scalar.

A.2. *Inlet disturbances*

For efficient transition three types of inlet disturbances are used in the simulation, random disturbances of a prescribed length scale, streamwise vortices and periodic streamwise forcing. All three disturbances are superpositioned at the inlet. The random disturbances are generated using a filter technique by Klein *et al.* (2003). The method employs a prescribed autocorrelation and a characteristic length scale of the disturbances to generate a digital filter. The filter is then applied to random fields to generate disturbances of a finite length scale which are also correlated in both time and space. The rms magnitude of the random disturbances used is 5% of the jet inlet velocity and the length scale used is $h/3$ in all three directions. In the investigation of Levin *et al.* (2005) it was reported that streamwise streaks play an important role in and also enhance the breakdown to turbulence in plane wall jets. The optimal longitudinal type disturbances were found to be streamwise vortices positioned in the upper shear layer. In the light of this, streamwise vortices are added in the upper shear layer in the simulation. The vortices are constructed using wall-normal and spanwise velocities of the form

$$v_v = A_v U_{in}\cos\left(\pi\frac{z}{w_v}\right)\sin\left(\pi\frac{(y-y_0)}{w_v}\right) \tag{16}$$

$$w_v = -A_v U_{in}\sin\left(\pi\frac{z}{w_v}\right)\cos\left(\pi\frac{(y-y_0)}{w_v}\right) \tag{17}$$

where $A_v = 0.01U_{in}$ is the vortex amplitude, $w_v = 0.6h$ the vortex width and $y_0 = 0.6h$ the lower bound of the vortices. In the streamwise direction periodic disturbances are used of the form

$$\begin{aligned} u_{st} =& A_{st}U_{in}\sin(2\pi St(t/\tau))+ \\ & A_{st}U_{in}\sin(1.5\times 2\pi St(t/\tau)) \end{aligned} \tag{18}$$

where $A_{st} = 5\times10^{-3}U_{in}$ is the disturbance amplitude, $St = 0.3$, is the Strouhal number and $\tau = h/U_{in}$ is the characteristic jet inlet time scale.

References

Abrahamsson, H., Johansson, B. & Löfdahl, L. 1994 A turbulent plane two-dimensional wall-jet in a quiescent surrounding. *Eur. J. Mech. B/Fluids* **13** (5), 533–556.

Ahlman, D., Brethouwer, G. & Johansson, A. V. 2006 A numerical method for simulation of turbulence and mixing in a compressible wall-jet. *Tech. Rep*. Dept. of Mechanics, Royal Instutute of Technology.

Alfredsson, P. H., Johansson, A. V., Haritonidis, J. H. & Eckelmann, H. 1988 The fluctuating wall-shear stress and the velocity field in the viscous sublayer. *Phys. Fluids* **31**, 1026–1033.

Bradshaw, P. & Gee, M. T. 1960 Turbulent wall-jets with and without external stream. *Aero. Res. Council R&M 3252* .

Chevray, R. & Tutu, N. K. 1978 Intermittency and preferential transport of heat in a round jet. *J. Fluid Mech.* **88**, 133–160.

Colonius, T. 2004 Modeling artificial boundary conditions for compressible flow. *Ann. Rev. Fluid Mech.* **36**, 315–345.

Davies, A. E., Keffer, J. F. & Baines, W. D. 1974 Spread of a heated plane turbulent jet. *Phys. Fluids* **18**, 770–775.

Dejoan, A. & Leschziner, M. A. 2005 Large eddy simulation of a plane turbulent wall jet. *Phys. Fluids* **17** (2), Art. No. 025102.

Eriksson, J. G., Karlsson, R. I. & Persson, J. 1998 An experimental study of a two-dimensional plane turbulent wall jet. *Experiments in Fluids* **25**, 50–60.

Förthmann, E. 1936 Turbulent jet expansion. *NACA TM* **789**, (English Translation).

Freund, J. B. 1997 Proposed inflow/outflow boundary condition for direct computation of aerodynamic sound. *AIAA Journal* **35** (4), 740–742.

George, W. K., Abrahamsson, H., Eriksson, J., Karlsson, R. I., Löfdahl, L. & Wosnik, M. 2000 A similarity theory for the turbulent plane wall jet without external stream. *J. Fluid Mech.* **425**, 367–411.

Gerodimos, G. & So, R. M. C. 1997 Near wall modeling of plane turbulent jets. *J. Fluids Eng.* **119**, 304–313.

Glauert, M. B. 1956 The wall jet. *J. Fluid Mech.* **1**, 625–643.

Gutmark, E. & Wygnanski, I. 1976 The planar turbulent jet. *J. Fluid Mech.* **73**, 465–495.

Irwin, H. P. A. H. 1973 Measurements in a self-preserving plane wall jet in a positive pressure gradient. *J. Fluid Mech.* **61** (1), 33–63.

Klein, M., Sadiki, A. & Janicka, J. 2003 A digital filter based generation of inflow data for spatially developing direct numerical or large eddy simulations. *J. Comp. Phys.* **186**, 652–665.

Launder, B. E. & Rodi, W. 1981 The turbulent wall jet. *Prog. Aerospace Sci.* **19**, 81–128.

Launder, B. E. & Rodi, W. 1983 The turbulent wall jet – measurements and modelling. *Ann. Rev. Fluid Mech.* **15**, 429–459.

Lele, S. K. 1992 Compact finite differences with spectral-like resolution. *J. Comp. Phys.* **103**, 16–42.

Levin, O. 2005 Numerical studies of transition in wall-bounded flows. PhD thesis, Royal Institute of Technology, KTH.

Levin, O., Chernoray, V. G., Löfdahl, L. & Henningson, D. 2005 A study of the blasius wall jet. *J. Fluid Mech.* **539**, 313–347.

Lundbladh, A., Berlin, S., Skote, M., Hildings, C., Choi, J., Kim, J. & Henningson, D. S. 1999 An efficient spectral method for simulation of incompressible flow over a flat plate. *Tech. Rep*. Dept. of Mechanics, Royal Instutute of Technology.

Narashima, R., Narayan, K. Y. & Parthasarathy, S. P. 1973 Parametric analysis of turbulent wall jets in still air. *Aeronaut. J.* **77** (July), 335–359.

Österlund, J. M. 1999 Experimental studies of zero pressure-gradient turbulent boundary layer flow. PhD thesis, Royal Institute of Technology, KTH.

Panchapakesan, N. R. & Lumley, J. L. 1993 Turbulence measurements in jets of air and helium. part 2. helium jet. *J. Fluid Mech* **246**, 225–247.

Poinsot, T. & Veynante, D. 2001 *Theoretical and Numerical Combustion*. R.T. Edwards.

Ramparian, B. R. & Chandrasekhara, M. S. 1985 LDA measurements in plane turbulent jets. *Trans. ASME: J. Fluids Eng.* **107**, 264–271.

Rodi, W. 1975 A review of experimental data of uniform density free turbulent boundary layers. In *Studies in convection* (ed. B. Launder), pp. 70–165. Academic.

Schneider, M. E. & Goldstein, R. J. 1994 Laser doppler measurement of turbulence parameters in a two-dimensional plane wall jet. *Phys. Fluids* **6** (9), 3116–3129.

Skote, M., Haritonidis, J. H. & Henningson, D. 2002 Varicose instabilities in turbulent boundary layers. *Phys. Fluids* **14** (7), 2309–2323.

Spalart, P. R. 1988 Direct numerical simulation of a turbulent boundary layer up to $Re_\theta = 1410$. *J. Fluid Mech.* **187**, 61–98.

Stanley, S. A., Sarkar, S. & Mellado, J. P. 2002 A study of flow-field evolution and mixing of in a planar turbulent jet using direct numerical simulation. *J. Fluid Mech.* **450**, 377–407.

Tailland, A. & Mathieu, J. 1967 Jet pariétal. *J. Mech.* **6**, 103–131.

Tangemann, R. & Gretler, W. 2001 The computation of a two-dimensional turbulent wall jet in an external stream. *Trans ASME: J. Fluids Eng.* **123**, 154–157.

Thomas, F. O. & Prakash, K. M. K. 1991 An experimental investigation of the natural transition of an untuned planar jet. *Phys. Fluids A* **3**, 90–105.

Visbal, M., Gaitonde, D. V. & Gogineni, S. P. 1998 Direct numerical simulation of a forced transitional plane wall jet. *AIAA Paper* 98-2643.

Wernz, M. R. & Fasel, H. F. 1996 Numerical investigation of unsteady phenomena in wall jets. *AIAA Paper* 96-0079.

Wernz, M. R. & Fasel, H. F. 1997 Numerical investigation of forced transitional wall jets. *AIAA Paper* 97-2022.

Wikström, P. M., Wallin, S. & Johansson, A. V. 2000 Derivation and investigation of a new explicit algebraic model for the passive scalar flux. *Phys. Fluids* **12**, 688–702.

Wygnanski, I., Katz, Y. & Horev, E. 1992 On the applicability of various scaling laws to the turbulent wall jet. *J. Fluid Mech.* **234**, 669–690.

Zhou, M. D. & Wygnanski, I. 1993 Parameters governing the turbulent wall jet in an external stream. *AIAA Journal* **31** (5), 848–853.

2

Paper 2

A numerical method for simulation of turbulence and mixing in a compressible wall-jet

By Daniel Ahlman, Geert Brethouwer and Arne V. Johansson

KTH Mechanics, SE-100 44 Stockholm, Sweden

A method for the direct numerical simulation of turbulent flow and mixing in the presence of a wall is described. The flow case considered is a plane wall-jet, where the passive scalar is added in the jet at the inlet in a non-premixed manner. The governing equations of fully compressible fluid flow, including a passive scalar are solved. The implementation of the numerical method in a computer code, using the Fortran language, is described. For the spatial integration compact finite difference schemes are used, and for the temporal integration a low-storage Runge-Kutta method is employed. The implementation is aimed at studying turbulence dynamics and mixing in the plane wall-jet configuration. Boundary zones are applied adjacent to the boundaries to minimize non-physical reflections. At the inlet, disturbances are introduced to facilitate fast transition to turbulence. The implementation uses MPI (Message-Passing Interface) to enable parallel computations on distributed memory computers.

1. Introduction

The area of turbulent mixing is interesting for a number of reasons. First and foremost, turbulent mixing is by far the most frequently occurring type of mixing in natural processes as well as in engineering applications. In nature atmospherical boundary layers, the Gulf Stream and the flow of rivers are all manifestations of turbulent flows. This means that phenomena such as heat transfer between the land and the atmosphere and the motion of plankton in the sea are substantially influenced by turbulent motion. Concerning engineering applications the flow in pipelines, the wake behind aircrafts and the discharge from smoke stacks all contain turbulent motion and mixing. One specifically important phenomena involving turbulent mixing is combustion. Combustion is used in a wide range of applications for power conversion such as e.g. gas turbines, furnaces and burners. The combustion in these devices almost exclusively consists of turbulent combustion, and is therefore dependent on turbulent mixing of reacting species prior to combustion. Practically all of these applications also contain solid walls e.g. enclosing chambers or piston cylinders. In the near-wall area, all previous mentioned mechanims, turbulence, mixing and combustion, will be altered. The wall introduces anisotropy of the

flow properties and also a heat flux towards the wall, since the wall in general is significantly colder than the reacting mixture.

One of the inherent features of turbulence is that any region of turbulent fluid contains a wide range of physical scales and according time scales. To fully resolve these scales in a simulation of turbulent mixing requires high resolution and numerical methods of high accuracy. Moreover, the high resolution has to be kept over the entire range of appearing physical scales.

The recent years of unprecedented increase in computational power have enabled ever increasing problems to be simulated, and has rendered possible significant insight into the fundamental character and features of turbulence and turbulent mixing. The methods used to perform simulations have similarly undergone gradual optimizations and extensions. Still, using the technology available today, the complexity of the problem necessitates a vast amount of computational time and memory.

With the aim of studying mixing in a turbulent wall-bounded flow, the present report presents a method for direct numerical simulation of mixing. The problem considered is the fully compressible form of the Navier-Stokes equations combined with the conservation equation of a passive scalar. The compressible formulation is used in order for the method to be applicable for extension to reacting flows, including heat release. The implemented flow case is a plane turbulent wall jet, where the passive scalar is added in the jet at the inlet in a non-premixed manner. The implemented method utilizes compact finite differences for the spatial integration in the manner described by Lele (1992). Adapting this approach enables high numerical accuracy at a reasonable computational cost while maintaining the ease in applying different boundary conditions. For time integration, a low-memory version of the standard Runge-Kutta scheme is used.

2. Governing equations

Below, the governing equations for compressible flow including mixing, are presented. The equations are first introduced in their general form, for a fluid flow containing any number of reacting species. Following this, the implemented equations, describing compressible flow including a non-reacting passive scalar are derived. The fully compressible formulation is used to facilitate a possible extension to reactive flow, including heat release, and the transport equation of a passive scalar is solved to investigate fluid mixing in the absence of reaction. The scalar is passive in the sense that is does not affect the motion of the fluid.

2.1. *Conservation of mass and species*

Global mass conservation for compressible flows, is expressed as

$$\frac{\partial \rho}{\partial t} + \frac{\partial \rho u_j}{\partial x_j} = 0 \tag{1}$$

where ρ is the mass density and u_j the velocity vector. Mass conservation for the individual species is dictated by transport equations, according to

$$\frac{\partial \rho_k}{\partial t} + \frac{\partial}{\partial x_j}\left(\rho_k(u_j + V_{k,j})\right) = \dot{\omega}_k \tag{2}$$

where ρ_k is the density of species $k = 1, \ldots, N$ participating in the simulated reaction or mixing. The $V_{k,j}$ term is the diffusion velocity V_k of species k in the x_j-direction, and $\dot{\omega}_k$ is the reaction rate of species k. Note that summation is not performed over the species index k. A more convenient approach for the species conservation is to utilize the species mass fractions of the mixture defined by

$$\theta_k = \frac{m_k}{m} \tag{3}$$

where m_k is the mass of the species k in a given volume V and m the total mass in this volume. This renders the species mass conservation equations on the form

$$\frac{\partial \rho\theta_k}{\partial t} + \frac{\partial}{\partial x_j}\left(\rho\theta_k(u_j + V_{k,j})\right) = \dot{\omega}_k \tag{4}$$

In multi species simulations the diffusion velocities and reaction rates are also subjected to global conservation

$$\sum_{k=1}^{N} \theta_k V_{k,j} = 0 \quad \textit{and} \quad \sum_{k=1}^{N} \dot{\omega}_k = 0 \tag{5}$$

To solve the conservation equations of a multicomponent system, the diffusion velocities $V_{k,j}$ have to be determined. The most exact way to do this is to solve the multicomponent diffusion equation, which can be derived from kinetic theory (see e.g. Chapman & Cowling 1990). This requires solving a linear system of size N^2 in each direction at each point, and hence the computational cost of this operation is often prohibitively high.

Most simulation codes therefore resorts to simplifications based on Fick's law. Following Fick's law the diffusive fluxes are assumed to be linearly dependent on the species gradients according to

$$V_{k,i}\theta_k = -\mathcal{D}_k \frac{\partial \theta_k}{\partial x_i} \tag{6}$$

where $\mathcal{D}_k$ is the diffusion coefficient of species k. Using this approximation, the species conservation equation, of a non-reacting ($\dot{\omega}_k = 0$) passive scalar takes the form

$$\frac{\partial \rho\theta}{\partial t} + \frac{\partial}{\partial x_j}\left(\rho u_j \theta\right) = \frac{\partial}{\partial x_j}\left(\rho \mathcal{D} \frac{\partial \theta}{\partial x_j}\right). \tag{7}$$

2.2. *Conservation of momentum*

Conserving the momentum results in the following governing equation valid for both reacting and non-reacting flows

$$\frac{\partial \rho u_i}{\partial t} + \frac{\partial \rho u_i u_j}{\partial x_j} = -\frac{\partial p}{\partial x_i} + \frac{\partial \tau_{ij}}{\partial x_j} + F_i \tag{8}$$

Here τ_{ij} represents the viscous stress tensor and F_i represent a present body force. Using the assumption of an isotropic Newtonian fluid, it is possible to derive a general form of the viscous stress tensor (Schlichting 1979)

$$\tau_{ij} = \mu\left(\frac{\partial u_i}{\partial x_j} + \frac{\partial u_j}{\partial x_i}\right) + \mu' \delta_{ij} \frac{\partial u_k}{\partial x_k} \tag{9}$$

where μ is the dynamic viscosity and μ' the second coefficient of viscosity, which is related to the bulk viscosity λ_b of the fluid through

$$\lambda_b = \mu' + \frac{2}{3}\mu. \tag{10}$$

The bulk viscosity represents the property of the fluid responsible for energy dissipation during a finite volume change of a fluid element at uniform temperature. Unless in some special inquiries, such as in the study of shock wave structure for example, the bulk velocity is in general assumed to be negligible. This is the case also in reacting flows (Kou 1986). Assuming zero bulk velocity, $\lambda_b = 0$, and no volume forces present, the momentum equation becomes

$$\frac{\partial \rho u_i}{\partial t} + \frac{\partial \rho u_i u_j}{\partial x_j} = -\frac{\partial p}{\partial x_i} + \frac{\partial}{\partial x_j}\left[-\frac{2}{3}\mu \frac{\partial u_k}{\partial x_k}\delta_{ij} + \mu\left(\frac{\partial u_i}{\partial x_j} + \frac{\partial u_j}{\partial x_i}\right)\right] \tag{11}$$

In the implementation, the dynamic viscosity μ is furthermore assumed to be constant.

2.3. *Conservation of energy*

The governing equation for the total energy, the sum of the internal and kinetic energy per unit mass $E = e + \frac{1}{2}u_i u_i$, reads

$$\frac{\partial \rho E}{\partial t} + \frac{\partial \rho E u_j}{\partial x_j} = -\frac{\partial q_j}{\partial x_j} + \frac{\partial (u_i(\tau_{ij} - p\delta_{ij})}{\partial x_j} \tag{12}$$

where q_j is the energy flux.

For a real non-reacting gas, the internal energy e can be described using two state varibles. The specific internal energy per unit mass e, and the enthalpy h are defined as

$$\begin{aligned} e &= e(T, v) \\ h &= e + pv = h(T, p). \end{aligned} \tag{13}$$

where v is the specific volume, $v = 1/\rho$. We assume a thermally perfect gas, and therefore the internal energy and enthalpy are functions of temperature only according to

$$\begin{aligned} e = e(T) \quad &\Longrightarrow \quad de = c_v dT \\ h = h(T) \quad &\Longrightarrow \quad dh = c_p dT. \end{aligned} \tag{14}$$

Here c_v and c_p denotes the specific heats at constant volume and pressure, which in general are functions of the temperature. If the specific heats are also assumed constant, the system is calorically perfect according to

$$\begin{aligned} e &= c_v T \\ h &= c_p T. \end{aligned} \tag{15}$$

The gas is assumed ideal and to obey the perfect gas law stating that

$$p = \rho R T. \tag{16}$$

where R is the specific gas constant. Rewriting the definition of enthalpy, using the perfect gas law, the specific heats can be expressed as

$$\begin{aligned} c_p &= \frac{\gamma R}{(\gamma - 1)} \\ c_v &= \frac{R}{\gamma - 1} \end{aligned} \tag{17}$$

where $\gamma = c_p/c_v$. Using these relations, the pressure and temperature can be written as functions of the internal energy e as

$$p = \rho R T = \rho R \frac{e}{c_v} = (\gamma - 1)\rho e \tag{18}$$

$$T = \frac{p}{\rho R} = \frac{(\gamma - 1)}{R} e \tag{19}$$

The energy flux q_i is composed of the heat diffusion, which is approximated by Fourier's law according to

$$q_i = -\lambda \frac{\partial T}{\partial x_i} \tag{20}$$

where λ is the coefficient of thermal conductivity. The heat diffusion can be expressed as a function of the inner energy and the specific heat c_p using (19) and (17) as

$$q_i = -\lambda \frac{\partial}{\partial x_i} \left(\frac{(\gamma - 1)e}{R} \right) = -\lambda \frac{\partial}{\partial x_i} \left(\frac{\gamma e}{c_p} \right). \tag{21}$$

The heat diffusion is often defined in terms of the Prandtl number, relating the momentum and heat transport

$$Pr = \frac{\nu}{\lambda/(\rho c_p)} = \frac{\mu c_p}{\lambda}. \tag{22}$$

Assuming a constant thermal conductivity, the energy flux becomes

$$q_i = -\frac{\partial}{\partial x_i}\left(\frac{\gamma\mu}{Pr}e\right) \tag{23}$$

and the energy equation, in terms of $E_t = \rho E$, for a non-reacting ideal gas becomes

$$\frac{\partial E_t}{\partial t} + \frac{\partial E_t u_j}{\partial x_j} = \frac{\partial}{\partial x_j}\left\{\frac{\partial}{\partial x_j}\left[\frac{\gamma\mu}{Pr}\left(\frac{E_t}{\rho} - \frac{1}{2}u_i u_i\right)\right]\right\} + \frac{\partial(u_i(\tau_{ij} - p\delta_{ij})}{\partial x_j}. \tag{24}$$

3. Spatial integration

A number of numerical algorithms exist for solving the governing equations (1), (7), (11) and (24). Turbulence contains a wide range of temporal and spatial scales, hence for a successful direct numerical simulation, algorithms that provide an accurate representation of the entire range of scales must be employed.

Presently the computational efficiency by employing spectral methods (see e.g. Canuto *et al.* 1987) is unsurpassed, and it has been successfully used in a wide range of simulations of turbulent flows including turbulent channel flows by Kim *et al.* (1987) and turbulent boundary layers in e.g. Spalart (1988) and Skote & Henningson (2002). However, spectral methods are limited to simple domains, from their global representation, and require special treatment at non-periodic boundaries and solid walls. This is a severe constraint, since there is an apparent need for simulations in complex geometries. Finite differences and finite elements use local numerical representations and hence maintain the flexibility in discretizing the geometry. Spectral elements (see e.g. Karniadakis & Orzsag 1993) represents an effort to combine the local discretization of finite elements and spectral methods. Simulations using this method include the works of Karniadakis (1989) and Fischer *et al.* (2002).

3.1. *Compact finite difference scheme*

In the present implementation compact finite differences are used for the spatial integration of the governing equations. Lele (1992) found that compact finite difference schemes provides both high accuracy and the ability to resolve a wider range of scales than ordinary finite differences. Using Fourier analysis, the resolution characteristics of the difference approximation is examined and found to provide an improved representation of the high wave numbers. Solvers based on compact finite differences have long been used in simulation of both fluid mechanics and other physics problems (see e.g. Hirsh (1975) and Adam (1977)). In the recent years an increasing number of simulations, of both reacting and non-reacting flows, have been performed using high order compact schemes.

Examples of such are e.g. Bédat *et al.* (1999), Stanley *et al.* (2002), Pantano *et al.* (2003), Boersma (2004) and Wang & Trouvé (2005).

3.1.1. *First derivative approximation*

The derivatives in the governing equations are discretized and solved on a equidistant computational grid X_i of unit length. The node positions are defined as

$$X_i = \Delta X_i(l-1) \tag{25}$$

using the node spacing $\Delta X_i = 1/(N_i - 1)$ and the node number l reaching from 1 to N_i, the respective number nodes in each direction.

To approximate the first derivatives, a formally sixth order compact finite difference scheme (Lele 1992) is used. The approximation is defined as

$$\frac{1}{3}f'_{i-1} + f'_i + \frac{1}{3}f'_{i+1} = \frac{7}{9\Delta x_i}(f_{i+1} + f_{i-1}) + \frac{1}{36\Delta x_i}(f_{i+2} + f_{i-2}). \tag{26}$$

where f'_i denotes the derivative at node i and f_i the corresponding functional value. Mimicking the global behavior of spectral methods, the compact discretization is implicitly dependent on the derivatives at neighboring points. The implicit formulation requires a tridiagonal system to be solved, providing all derivative values along a line in the domain. The system is solved using the Thomas algorithm, usually found in handbooks on numerical methods (see e.g. Tannehill *et al.* 1997).

3.1.2. *Boundary formulation*

At periodic boundaries the domain is simply assumed to be convoluted, and the near boundary nodes are treated in the same manner as the inner points. At non-periodic boundaries, one-sided or reduced stencils are used at the near boundary nodes. The boundary approximations used are presented in Lele (1992). The right-hand-side stencil size of the derivative approximation (26) is 5, meaning that dedicated boundary formulations are required at the two first nodes.

At the boundary a one-sided third order approximation which reads

$$f'_1 + 2f'_2 = \frac{1}{\Delta x}\left(-\frac{5}{2}f'_1 + 2f'_2 + \frac{1}{2}f'_3\right) \tag{27}$$

is used. The formulation is designed to maintain the tridiagonal form of the system matrix. A fourth order scheme also exists of the same form, but the spectral analysis in (Lele 1992) reveal that the third order scheme provides smaller dispersion errors. On the other hand, the third order scheme is noted to exhibit dissipative errors, confined in the high wavenumber range.

At the node next to the boundary, the following fourth order compact scheme is used

$$\frac{1}{4}f'_{i-1} + f'_i + \frac{1}{4}f'_{i+1} = \frac{3}{4\Delta x}\left(f_{i+1} - f_{i-1}\right) \tag{28}$$

3.2. *Grid mapping*

The physical domain x_i is defined through coordinate transformations of the computational domain as $x_i = x_i(X_j)$. The grid is structured and each coordinate direction can be stretched independently. Coordinate transformations used in the simulations of the plane wall-jet are defined in section 6.1.1. Following differentiation on the computational grid, the nodal values on the physical grid are recovered by use of the chain rule since

$$\frac{\partial f}{\partial X_j} = \frac{\partial f}{\partial x_i}\frac{\partial x_i}{\partial X_j}. \tag{29}$$

4. Temporal integration

4.1. *Low-storage Runge-Kutta scheme*

Temporal integration of the governing equations are performed by applying a low-storage Runge-Kutta scheme. The scheme used is accurate to the third order and was proposed in Lundbladh *et al.* (1999). If the system of governing equations are written as

$$\frac{\partial \psi}{\partial t} = G, \tag{30}$$

where G is the entire right-hand-side of the system, the time step discretization is performed through

$$\psi^{n+1} = \psi^n + a_n G^n + b_n G^{n-1} \tag{31}$$

where n is the time level and a_n and b_n are discretization constants. The discretization contains four stages, i.e. the solution is advanced one full time step by computing the solution at four intermediate time stages $t = t + c_n$. The discretization is referred to as low-storage, because a reduced number of variables, compared to the original formulation, are kept in the memory at each time stage. The discretization constants are presented in table 4.1.

RK3	$n=1$	$n=2$	$n=3$	$n=4$
$a_n/\Delta t$	8/17	17/60	5/12	3/4
$b_n/\Delta t$	0	−15/68	−17/60	−5/12
$c_n/\Delta t$	0	8/17	8/15	2/3

TABLE 1. RK3 time discretization constants.

4.2. *Time step restriction*

From basic theory of numerical solution of partial differential equations (see e.g. Tannehill *et al.* 1997) it is known that in order to keep a simulation stable, the time step needs to be restricted. For the linear case, conditional stability requirements for the time step and spatial mesh spacing can be derived. This is called the CFL (Courant-Friedrichs-Lewy) condition. In analogy, a CFL

number can be defined for the present non-linear case, and used to restrict the time. The global CFL number for the simulation is here defined as

$$CFL_{\text{global}} = \Delta t \ \max\left(\frac{|u(x,y,z)+c|}{\Delta x} + \frac{|v(x,y,z)+c|}{\Delta y} + \frac{|w(x,y,z)+c|}{\Delta z}\right) \tag{32}$$

where c is the local speed of sound, $(\Delta x, \Delta y, \Delta z)$ the local node spacing and Δt the time step. For a plane wall jet, using the discretization techniques defined above, $CFL_{\text{global}} = 0.6$ has been found to provide stable simulations.

5. Filtering

In DNS of turbulent flows using compact finite differences for spatial discretization, some energy accumulates in the high wave numbers. This is caused by aliasing errors when calculating nonlinear terms and sometimes due to insufficient resolution. Non-physical high wave number waves may also be produced by reflections at the boundary. To avoid the accumulation of high wave number disturbances, low-pass filters are applied to the solution variables. Filtering of the fluid variables is performed every ten time steps using the explicit sixth order filter suggested by Lele (1992),

$$\hat{f}_i = \frac{11}{16}f_i + \frac{15}{32}(f_{i+1} - f_{i-1}) - \frac{3}{16}(f_{i+2} - f_{i-2}) + \frac{1}{32}(f_{i+3} - f_{i-3}) \tag{33}$$

where $\hat{f}_i$ denotes the filtered property. In the two nodes adjacent to the boundary a fourth order filter from Lele (1992) is used

$$\hat{f}_2 = \frac{3}{4} + \frac{1}{16}(f_1 + 6f_3 - 4f_4 + f_5), \tag{34}$$

$$\hat{f}_3 = \frac{5}{8} + \frac{1}{16}(-f_1 + 4f_2 + 4f_4 + f_5). \tag{35}$$

For the scalar another filtering approach is used. From previous simulations it was noted that unphysical disturbances, caused by dispersion errors, led to negative concentrations. This problem is well known for compact finite differences and is inherent from the central formulation. In an effort to reduce the negative concentrations, a low order filter is applied to the scalar concentration in the first part of the jet, $x/h < 12$. In the initial region the scalar is filtered using a second order filter

$$\hat{f}_i = f_i + \frac{f_{i+1} + f_{i-1}}{2}. \tag{36}$$

The inlet region is filtered with a longer time interval of 300 time steps, to minimize the numerical diffusion. In the remainder of the domain the scalar is filtered with the same filter as the fluid variables, using the same filtering period. Employing the lower order filter for the scalar over the transition region, one completely avoids the creation of negative concentration in this region, but downstream some spots with negative concentration still develop. Using the described filtering approach, the largest negative concentrations are

approximately 3% of the inlet scalar concentration, and the regions of negative concentration are reduced.

5.1. *Boundary Conditions*

Boundary conditions are a crucial part of simulation of fluid flow. This is especially true in the case of direct simulation using high order numerical schemes. In this case the scheme introduces very low levels of numerical viscosity, and errors generated at the boundaries may propagate large distances through the domain interacting with the rest of the flow.

Errors initiated by the numerical boundary treatment basically originate from simulation compromises. First there is often a need for truncation of the computational domain. Usually in simulations one or more directions have to be considered non-periodic. The simulation compromise of a truncated domain is that the influence of the exterior region is not available in the simulation. Lacking information on what the flow is like outside the computational domain, means that the physical effects on the interior solution have to be modelled. Apart from the truncation compromise, the desired feature of a boundary condition can be formulated in one statement, to not allow any sort of non-physical reflections.

Basically numerical waves can be said to be generated when the numerical method, including the boundary treatment, is unable to resolve the full spectrum of the physical processes. Using initial conditions with too steep gradients produce spurious waves since the steep profiles contain high wavenumber components. Rapid grid stretching or changes in the differencing scheme also excite numerical waves since the resolving capability is altered over the grid. In the vicinity of the boundary, the scheme inevitably has to be changed, and hence spurious waves will be produced here.

The task of producing boundary condition implementations fulfilling all the requirements is quite a formidable one. For linear equations of motion or in problems where linearization around a mean flow is a good approximation, it is possible to derive non-reflecting boundary conditions of arbitrary order (Rowley & Colonius 2000). However this is not the case when significant nonlinear effects are present near the boundary, as is the case at turbulent outlets. In this case it has been found necessary to add relatively crude, but effective, boundary zones or absorbing layers adjacent to the boundaries (see e.g. Colonius 2004).

5.1.1. *Boundary zones*

In the present implementation boundary zones in the manner of Freund (1997) are employed in order to minimize the reflection and generation of spurious waves at the boundaries. The method involves the addition of two extra terms to the governing equations, in the vicinity of inflow and outflow boundaries. The terms consist of an additional convection velocity $U_a(x)$ and a damping term $\sigma_a(x)$. The form of the modified equations, after addition of the boundary

zone terms, is exemplified by the continuity equation which becomes

$$\frac{\partial \rho}{\partial t} = -\rho \frac{\partial u_i}{\partial x_i} - [u_i + U_a(x)] \frac{\partial \rho}{\partial x_i} + \sigma_a(x)(\rho - \rho_{tg}) \tag{37}$$

$$= -\frac{\partial \rho [u_i + U_a(x)]}{\partial x_i} + \rho \frac{\partial U_a(x)}{\partial x_i} + \sigma_a(x)(\rho - \rho_{tg}) \tag{38}$$

The extra convection term $U_a(x)$ is designed to generate supersonic conditions in the zones adjacent to the boundary, while the purpose of the damping term is to force the solution towards a target function. At the inlet an upstream traveling disturbance will slow down as it encounters the artificial convection and eventually be dissipated by the damping term.

At the outflow the disturbances are accelerated out of the domain, so that they cannot travel back into the domain, and subsequently dissipated by the damping term. The boundary terms added are finite only near the boundaries and exponentially small in the interior of the domain.

6. Plane wall-jet simulation

The following section describes the setup of the plane wall-jet simulation. The definition of the computational domain and its inlet and boundary conditions are described. The application of inlet disturbances is also presented.

6.1. *Computational domain*

6.1.1. *Grid definition*

To simulate a plane wall jet, the governing equations are solved on a rectangular domain of physical size $L_x \times L_y \times L_z$ in the streamwise, wall-normal and spanwise direction respectively. The computational domain is discretized using a structured grid containing `imax` × `jmax` × `kmax` nodes. The grid is stretched in the wall-normal and the streamwise direction but uniform in the spanwise.

In the streamwise direction a third order polynomial is used to transform the uniform computational distance $0 \leqslant x \leqslant 1$ to physical distance x_r according to

$$x_r = L_x(ax^3 - ax^2 + bx) \tag{39}$$

where a and b are stretch constants. The formulation and the stretch constants are chosen so the highest node density is positioned in the transition region, where small scales are present. Further downstream the node separation increases.

In the wall-normal direction, the grid is stretched using a combination of two transformation functions. The physical wall distance y_r is defined as

$$y_r = L_y \left(A_y f_1^y + (A_y - 1) f_2^y\right) + c_0 \tag{40}$$

$$= L_y \left(A_y \frac{1 + \tanh\left[2\pi\alpha(y-1)\right]}{\tanh\left(2\pi\alpha\right)} + (A_y - 1) \frac{\ln[(\beta + y)/(\beta - y)]}{\ln[(\beta + 1)/(\beta - 1)]} \right) + c_0 \tag{41}$$

where y is the uniform computational coordinate, $0 \leqslant y \leqslant 1$. The first function f_1^y provides a clustering of nodes at the wall in order to resolve the inner part of the boundary layer. Using this function alone however would introduce large node separations in the outer shear layer, particularly far downstream, from the outward expansion of the jet. Therefore a second function f_2^y is used, to reduce the node separations in the outer part of the jet, and also to increase the node stretching in the region above the jet. The individual stretch rate of the functions are determined by the constants α and β, while the constant A_y determines the fraction of each function used in the combination. The constant c_0 is used to place the first node at $y_r = 0$.

6.2. *Inlet profiles*

The wall-jet is formed by applying a two-dimensional jet profile at the inlet. The jet is injected along the wall and parallel to it. Above the jet inlet, a constant coflow of 10% of the jet inlet velocity, $U_c = 0.10U_{in}$ is applied. The coflow is applied for computational efficiency reasons. Due to engulfing processes, large scale vortices are created in the outer part of the turbulent jet. Theses structures may propagate out into the ambient flow. Without the coflow these structures are very persistent (see Levin 2005). The coflow ensures that the vortices above the jet can leave the domain, without contaminating the statistics.

The inlet velocity consists of a composite profile constructed from three parts, an inner profile from the wall out U_w, a jet center profile U_c and an outer profile U_t containing the top of the jet and the above coflow region. The full profile, $U_{\text{inlet}}(y)$, is defined as

$$U_{\text{inlet}}(y) = \begin{cases} U_w(y) & 0 \leqslant y \leqslant y_{c1} \\ U_c(y) & y_{c1} \leqslant y \leqslant y_{c2} \\ U_t(y) & y_{c2} \leqslant y \leqslant L_y \end{cases} \tag{42}$$

with connecting points, $y_{c1} = 0.46h$ and $y_{c2} = 0.54h$, just beneath and above the jet center, with h denoting the jet height. At the connecting points, the functions are curve fitted to be continuous and preserve the first derivative. For the inner and outer profiles, hyperbolic tangent profiles are used, while the connecting center profile is a second order polynomial. The individual profiles are prescribed according to

$$U_w(y) = U_{in} \tanh\left[G(\sqrt{(y-c)^2} - \frac{w}{2})\right] \tag{43}$$

$$U_c(y) = -A_c y^2 + B_c y + C_c \tag{44}$$

$$U_t(y) = \frac{U_{in}}{2}\left(\left(1 + \frac{U_c}{U_{in}}\right)\left\{1 - \tanh\left[G_t\left(\sqrt{(y-c_t)^2} - \frac{w_t}{2}\right)\right]\right\}\right) \tag{45}$$

where G and G_t determine the profile gradients, c and c_t the jet center and w and w_t the width of the inner and outer profiles. The jet width and center position are assigned when creating the inner profile.

The inlet profile for the passive scalar is defined as

$$\theta_{\text{inlet}}(y) = \frac{\theta_{in}}{2}\left\{1 - \tanh\left[G_\theta\left(\sqrt{y^2} - h_\theta\right)\right]\right\} \tag{46}$$

where θ_{in} is the inlet scalar concentration at the wall. The profile steepness is specified in accordance to the outer velocity profile $G_\theta = G_t$ and the scalar inlet height is set to the jet height $h_\theta = h$. The resulting scalar profile is finite at the wall and zero above the jet, i.e. no coflow condition is used for the scalar.

On the wall, no-slip conditions are used for the velocity components and a no-flux condition is enforced for the scalar through $\partial\theta(y=0)/\partial y = 0$.

6.3. *Top inflow condition*

At the top of the domain an inflow velocity is used for entrainment reasons. In the outer part of the wall-jet, coflow fluid is entrained by turbulent structures, introducing a downstream increase of the streamwise mass flux. Since the domain is finite, the entrainment must be accounted for at the top of the domain, in order to not constrain the jet development. Integrating the stationary two-dimensional continuity equation from the wall out, an estimation of the mean inflow velocity can be found as

$$\frac{\partial \rho U}{\partial x} + \frac{\partial \rho V}{\partial y} = 0 \quad \Longrightarrow \quad \rho_\infty V_\infty = -\frac{\partial}{\partial x}\int_0^\infty \rho U\, dy = -\frac{\partial}{\partial x} M_x(x) \tag{47}$$

where $M_x(x)$ is the streamwise mass flux. Using the data of Eriksson *et al.* (1998), the streamwise mass flux is found to increase linearly according to $M_u(x) \sim 0.031 M_x^0(x/h)$ in terms of the jet inlet mass flux M_x^0 and the slot normalized downstream distance. Tailoring the simulation according to the experiment the top inflow velocity is prescribed as

$$V_\infty = -0.031 M_x^0/h\rho_\infty \tag{48}$$

6.4. *Boundary zones*

Boundary zones in the manner of Freund (1997) are employed to minimize the reflection and generation of spurious waves at the boundaries. The formulation and background of the technique applied were described in section 5.1.1. The shape of the boundary zones terms used are

$$\begin{aligned} U_a(x) =& A^U_{\text{inl}}(1 - \tanh[\beta_{\text{inl}}(x/L_x - x_{\text{p,inl}})]) + \\ & A^U_{\text{out}}(1 + \tanh[\beta_{\text{out}}(x/L_x - x_{\text{p,out}})]) \end{aligned} \tag{49}$$

$$\begin{aligned} \sigma_a(x) =& A^\sigma_{\text{inl}}(1 - \tanh[\beta_{\text{inl}}(x/L_x - x_{\text{p,inl}})]) + \\ & A^\sigma_{\text{out}}(1 + \tanh[\beta_{\text{out}}(x/L_x - x_{\text{p,out}})]) \end{aligned} \tag{50}$$

$$\sigma_a(y) = A^\sigma_{\text{top}}(1 + \tanh[\beta_{\text{top}}(y/L_y - y_{\text{p,top}})]) \tag{51}$$

where the A coefficients determine the zone magnitude, the β coefficients the zone gradients and x_p the zone positions. From previous simulations the boundary zones have been found to be very efficient in terms of the width of the zones needed. Zone widths in the order of a couple of jet inlet heigths h are sufficient for reasonable non-reflecting boundaries. The boundary zone coefficients used are presented in the tables below.

Term	A_{inl}	A_{out}	β_{inl}	β_{out}	$x_{\mathrm{p,inl}}$	$x_{\mathrm{p,out}}$	w_{inl}	w_{out}
Convection; U_a	0.6	0.6	220	120	0.005	0.985	h	$2h$
Damping; σ_a	0.45	0.2	220	120	0.005	0.985	h	$2h$

TABLE 2. In and outlet boundary zone coefficients and the zone widths generated.

Term	A_{top}	β_{top}	$x_{\mathrm{p,top}}$	w_{top}
Damping; σ_a	0.225	2.0	0.944	$4h$

TABLE 3. Top boundary zone coefficients and the zone width generated.

6.5. *Inlet Disturbances*

At the inlet, disturbances are added to the velocity fields in order to trigger breakup to turbulence. The aim of the simulation is to study properties in the turbulent wall-jet, therefore proper inlet disturbances are of importance to facilitate a fast transition, leaving as large portion of the domain as possible for turbulent propagation. For efficient transition three types of inlet disturbances are used in the present simulation, random disturbances of a prescribed length scale, streamwise vortices and periodic streamwise forcing. The random disturbances are generated using a filter technique by Klein *et al.* (2003). The method uses a prescribed autocorrelation and a characteristic length scale of the disturbances to generate a digital filter. The filter is applied to random fields to generate disturbances of a finite length scale, which are also correlated in both time and space.

In the investigation of Levin *et al.* (2005) it was reported that streamwise streaks play an important role and also enhance the breakdown to turbulence in plane wall-jets. The optimal longitudinal type disturbances were found to be streamwise vortices positioned in the upper shear layer. In the light of this, streamwise vortices are added in the upper shear layer in the wall-jet. The vortices are constructed using wall-normal and spanwise velocities of the form

$$v_v = A_v U_{in} \cos\left(\pi \frac{z}{w_v}\right) \sin\left(\pi \frac{(y-y_0)}{w_v}\right) \tag{52}$$

$$w_v = -A_v U_{in} \sin\left(\pi \frac{z}{w_v}\right) \cos\left(\pi \frac{(y-y_0)}{w_v}\right) \tag{53}$$

where A_v is the vortex amplitude, w_v the vortex width and y_0 the lower bound of the vortices. In the streamwise direction periodic disturbances are used of the form

$$\begin{aligned} u_{st} =& A_{st}U_{in}\sin(2\pi St(t/\tau))+ \\ & A_{st}U_{in}\sin(1.5\times 2\pi St(t/\tau)) \end{aligned} \tag{54}$$

where A_{st} is the disturbance amplitude, St, is a Strouhal number and $\tau = h/U_{in}$ is the characteristic jet inlet time scale.

7. Implementation

In the previous sections, a numerical method for solving the propagation of a turbulent and compressible plane wall-jet, including the mixing of a passive scalar, was presented. Here an implementation of the complete algorithm is described. The implementation is named `parjet` and is written in standard Fortran 90. Parallelization of the computation is performed through the use of MPI functions (see e.g. Snir *et al.* 1996).

7.1. *Code origin and development*

The present code was originally written by Dr. Bendiks Jan Boersma, and used to simulate the sound field produced by a round jet (Boersma 2004). The code has been changed and extended in order to perform simulations of a plane-wall jet including passive scalar mixing. The basic structure of the solution procedure, the computational techniques and the method for parallel computation, has been maintained from the original implementation.

The development of the code consisted of a redesign of the computational domain, the formulation of boundary conditions and inlet disturbances and the addition of a passive scalar equation. The numerical spatial and temporal integration schemes has been changed while retaining the original discretization methods.

In the redesign of the domain, the spanwise direction was made periodic, including appropriate modifications of the spanwise derivative scheme, and the a grid stretching for the plane wall-jet was developed. To facilitate plane wall-jet simulation, a corresponding inlet profile was developed. Boundary conditions, including boundary zones later described, were adjusted for the wall-jet. An effort was made to develop efficient inlet disturbances using three different types of disturbances. A program was written to precalculate disturbances of a defined length scale. To minimize dispersion errors in the passive scalar, a filtering scheme, using a lower order filter in the initial part of the domain, was developed.

7.2. *Program Structure overview*

The simulation code `parjet` consists of one main program file, `jet.f`, and a number of separate subroutines. The subroutines perform specific tasks in the solution procedure and are either positioned in the latter part of `jet.f` or in

separate files. Apart from the main program and the subroutines employed, files specifying variables common for several subroutines are used. These files contain declarations and specifications of common parameters, variables and I/O paths. A list of the common files are found in Appendix Appendix A, and full list of the algorithm files for the implementation can be found in Appendix Appendix B. The algorithm file list includes a brief description of each file and which subroutines they contain.

It should be noted that the implementation uses a reversed dimension convention for the wall-normal and spanwise direction. The second dimension corresponds to the spanwise direction, and variables and derivatives in this direction are named accordingly (using j, y or v). The third dimension is the wall-normal direction, with variables names containing k, z or w.

The program structure basically consists of two major parts, initialization of the problem and the time stepping loop, where the second part, in turn, can be further split into five stages. The program structure is depicted in figure 1. The time step loop contains the specific parts of CFL condition, time stepping, filtering, statistics calculation and output. The latter three procedures are dashed indicating that they are not passed in all time steps. The program parts are further described below.

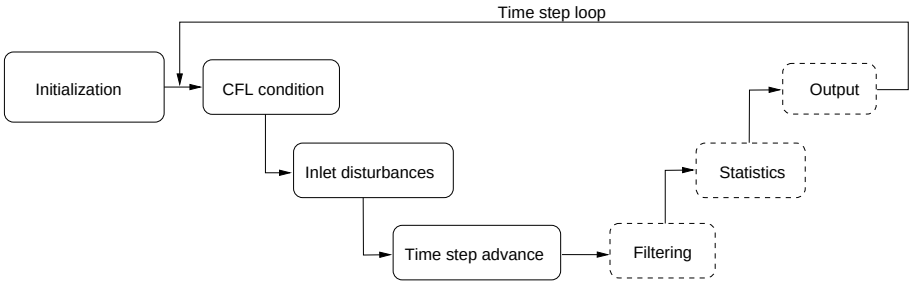

FIGURE 1. Program structure overview.

7.3. *Initialization*

The first part of `jet.f` contains the run initialization, which in turn consists of the following instances in sequential order:

- The parallelization is initialized, distributing the solution variables over the processes. Each processes is assigned a `rank` number, defining its position in the streamwise direction. The `rank` ranges from `0` at the inlet to `(Px-1)` at the outlet.
- The timing files are opened. These remain open throughout the execution of the code as timing information of the various instances of the solution is appended to these files during runtime.
- The data transpose procedure is initialized by calling `init_transpose()`

- The case parameter file `DNSinput.txt` is read by all processes. The first process, `rank` = 0, outputs the run parameters as well as appends them to `caseINFO.txt`.
- Subroutine `grid()` defines the computational domain and the node transformation describing the physical domain.
- Subroutine `init()` initializes the runtime variables. Solution variables are assigned initial values while boundary condition variables are defined to be used throughout the simulation.
- If the starting time step as defined in `DNSinput.txt` is larger than 0, a previous solution is read by `read_field()` to allow for continued simulation. The previous global time is recovered by reading time step file `starttime`.
- Subroutine `bound()` is called to set the boundary conditions.

7.4. *CFL condition*

An adaptive time step approach is used in the simulations, i.e. the time increment is calculated, at each time step, to correspond to a constant CFL number. The subroutine `cfl()` is called to generate the time increment and the CFL criteria is governed by the variable `cflCrit`, which is defined in the subroutine. It was previously noted that, the simulation might be sensitive to inlet disturbances at startup. For this reason a reduced CFL number is used at the initial `startupts` time steps.

The settings used for the plane wall jet simulations were, `cflCrit=0.6`, `cflCrit_init=cflCrit/2` and `startupts=500`

7.5. *Inlet disturbances*

The wall-jet simulations uses three types of inlet disturbances defined in section 6.5. For computational efficiency, the correlated disturbances (Klein *et al.* 2003) are precalculated. Complete sets of inlet velocity fields, describing disturbances in the three velocity components over the jet inlet, are stored in files and read in each time step. The inlet disturbances are superpositioned and stored in `common` variables `uinplane`, `vinplane` and `winplane`. These inlet disturbance variables are updated by calling subroutine `inprof_func()`, and applied to the computational domain by invocing `bound()`.

7.6. *Time step advancement*

Time advancement of the solution is performed by invoking the subroutine `lsRK3()`, which uses a third order Runge-Kutta method on low-storage storage form, as described in Lundbladh *et al.* (1999). The time stepping procedure is outlined using Fortran style pseudo code in figure 2. The method uses four sub-steps, denoted by `RKstep`, to advance the solution one time step. In each time steps the components of the stress tensor $\sigma_{i,j}$ are first computed using subroutine `stress()`, after which the entire right hand sides of the governing equations on the form of are computed. The computation is done sequentially

by `rhs_x()`, `rhs_y()` and `rhs_z()`, each computing the terms with derivatives in the x, y and z respectively. The parallelization of the simulation requires that the variables are transformed prior to and after the computation of the x-direction. The parallelization procedure described in detail in section 7.9.

The solution is then advanced one sub-step by multiplication by the time stepping coefficients. Following the sub-step advancement the boundary conditions are re-set and the previous right hand side solution is stored for use in next sub-step.

```
!234567
      do RKstep=1,4

!        *** Calculate stress tensor s_ij
         call stress()

!        *** Spatial integration of the rhs
         call tposei2k()          ! i2k transpose
         call rhs_x()
         call tposek2i()          ! k2i transpose

         call rhs_y()
         call rhs_z()

!        *** Update variables
         do node=1,all
            var(node) = var(node) + a(RKstep)*var_rhs_New(node)
     1                            + b(RKstep)*var_rhs_Old(node)
         enddo

!        *** Set boundary conditions
         call bound()

!        *** Save previous rhs
         var_rhs_Old = var_rhs_Old
      enddo
```

FIGURE 2. Pseudo Fortran snippet describing the time stepping subroutine `lsRK()`.

7.7. *Filtering*

During simulation, the solution variables are continuously filtered using low-pass filters to avoid accumulation of dispersion errors in the high wave number range. The high order numerical schemes used introduce very little numerical diffusion, and hence if filtering is not performed, or if a too long filtering period is used, the high wave number errors may grow causing a break down of the

simulation. For a further discussion of the origins of numerical errors and a description of the filters in use see section 5.

Filtering of the solution variables is performed following the solution advancement. How often, in terms of time steps, the filtering is applied is defined by the filtering separation variables `filt_sep`, `Yfilt_sep_inl` and `Yfilt_sep` where the first defines the filtering rate for the five fluid mechanics variables, u_i, ρ and E_t, (over the entire domain), the second one the filtering rate for the scalar concentration θ over the initial part of the domain and the last one the rate for the scalar over the remaining part of the domain. As was described in section 5, the filtering of the scalar in the initial part of the domain is performed with a second order scheme, and the application frequency of this filter is therefore reduced in order to keep the introduced numerical diffusion to a minimum. The filtering rate variables are specified in the runtime parameter file `DNSinput.txt`.

7.8. *Statistics*

Statistics of the flow and mixing can be generated by continuously writing the solution variables for post-processing, or by in-loop sampling. The various output routines used by `parjet` are described in the section below. The in-loop statistics are produced by the routine `jet_ProfAvFavre2Func()`, which generates first and second oder statistics, i.e. means, fluctuations and fluxes, of the fluid and scalar variables. Statistics characteristic of the inner, boundary layer type shear layer, such as the wall friction τ_w and the friction velocity u_τ are also calculated. These can be used to scale the wall jet statistics.

All in-loop statistics are generated in an ensemble manner by sampling using a time step separation of `av_sep` defined in `DNSinput.txt`. The same time step separation is used for the whole domain. In each sampling instance, the statistics is averaged over all positions in the periodic spanwise direction, but not over the developing, downstream, or the wall normal direction. The averaging procedure used is

$$\langle f(x_i, y_j)\rangle = \frac{1}{N}\sum_{n=1}^{N}\frac{1}{\texttt{kmax}}\sum_{k}^{\texttt{kmax}} f(x_i, y_j, z_k)^{\{n\}} \tag{55}$$

where n denotes the sample number, N is the total number of samples and `kmax` the number of nodes in the spanwise direction. Concerning decompositions of the variables, both Reynolds and Favre averages are produced. Reynolds averaged properties, which are the conventional ones for incompressible flow, are produced by decomposing the instantaneous variable f into an average part $\bar{f}$ and a fluctuating part f' according to

$$f = \bar{f} + f'. \tag{56}$$

Mass-weighted, or Favre, averaged properties are produced through the decomposition

$$f = \widetilde{f} + f'' = \overline{\rho f}/\overline{\rho} + f'' \tag{57}$$

where the mass-weighted average is denoted $\widetilde{f}$ and the fluctuation by f''.

Apart from the statistics, information on the global convergence rate of a set of the statistics variables are produced by continuously calculating the $L2$-norm of the change in the variable compared to the previous sampling. For example the convergence of the mean streamwise velocity is monitored by

$$\widetilde{u}_{L2}^{\{n\}} = \left(\sum_{i=1}^{\texttt{imax}} \sum_{j=1}^{\texttt{jmax}} \sum_{k=1}^{\texttt{kmax}} \left(\widetilde{u}(i,j,k)^{\{n\}} - \widetilde{u}(i,j,k)^{\{n-1\}} \right)^2 \right)^{1/2} . \tag{58}$$

It should however be kept in mind that this is a global measure for the whole domain. The flow scales in the wall-jet are developing downstream and the global measure cannot give information on the local convergence. In the wall-jet simulations the convergence decreases in the downstream direction because both length and time scales increase in this direction, requiring larger sampling times for converged statistics.

A full list of the statistics generated by `jet_ProfAvFavre2Func()` and their definitions are provided in Appendix Appendix C. All statistics variables are declared as `common` in the main file `jet.f` and `jet_ProfAvFavre2Func.f` to enable continuous sampling during runtime. The statistics variables are initialized as zero in the first calculated time step. In each sampling time step the statistics are also written to files. These files in turn are read at startup of a continuing run.

7.9. *Parallelization*

Parallelization of the simulation procedure is realized by running the compiled code on a number of processors using a Single Program, Multiple Data (SPMD) approach, where each processor runs the same program using a particular part of the total data set. The partitioning of the data and intercommunication between processors is handled by employing an implementation of the *Message Passing Interface* (MPI) standard, Snir *et al.* (1996).

The parallelization formally consists of subdividing the complete set of solution variables, the fluid dynamics and the scalar concentration, into a number of partitions, and supplying each partition together with a copy of the code to a number of processes. The solution is carried out in parallel by the different processes, each solving the problem on its assigned domain partition. The partitioning of the variables is done along the first index, i, which for the wall-jet corresponds to the x or downstream direction, so that each partition contains an equal number, `imax/Px`, of x-direction nodes where `Px` is the number of processes in use. The number of processes is set by assigning a number to the parameter `Px` in the parameter file `param.txt` prior to compilation. The partitions are statically declared at compilation time. The number of processes is not strictly defined by the available number of physical processors (CPUs). In principal any number of processes can be used, more or less than the number of available processors. However for maximum computational efficiency it is

strongly suggested that the number of processes correspond to the number of processors.

The choice of compact finite differences as means of spatial integration, however precludes the parallelization to rely solely on domain variable subdivision. As was noted in section 3.1, the derivative at any given point is implicitly dependent on the derivative at the neighboring points, which requires a system of linear equations to be solved. Hence the finite difference formalism requires all functional values in the direction of differentiation to be given. Differentiation along the two directions where subdivision is not employed, j and k, can be performed locally on each process. Along the i direction, on the other hand, the data is distributed over the processors, which prevents local differentiation. To allow for differentiation in the i-direction, the distributed variables are transposed to be distributed over the k direction instead. The transpose procedure includes collective communications, including all processes, using the MPI function `mpi_alltoall()`. Following the transposition, the differentiation in the i direction is performed, before a re-transposition is carried out to return to the the variables to their initial distribution. The transposition procedure required for downstream differentiation of `unew`, the downstream velocity component, is outlined in figure 3. The subroutine `tposei2k()` is used to transpose the data and `tposek2i()` is used for the re-transpose.

It should be noted that for transposition of the data to be possible, the number of nodes in the two distribution directions `imax` and `kmax` have to be evenly divisible by the number of processors `Px`. This requirement is checked at the run startup.

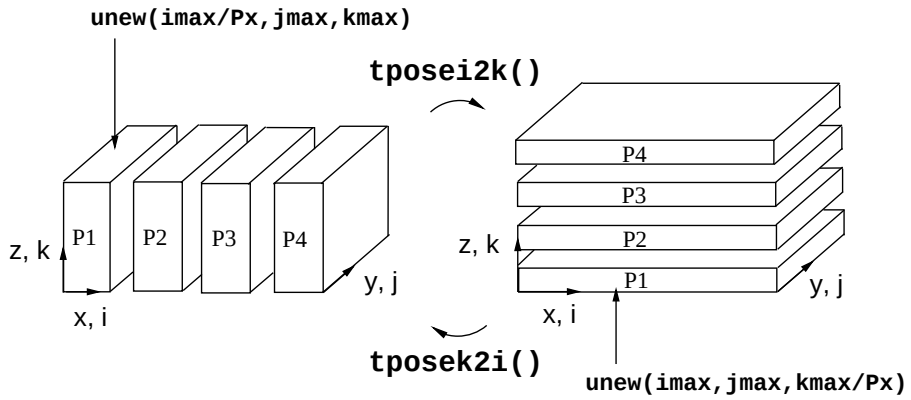

FIGURE 3. Transpose procedure required for i-direction differentiation using 4 processors (`Px=4`).

Appendix A. Implementation common files

Table 4: Common files of the `parjet` implementation.

File	Description
`DNSinput.txt`	Runtime parameters
`makefile`	Compilation makefile
`param.txt`	Compilation parameters
`common.txt`	`COMMON` file
`jetmodules.f`	`module` file
`commonPaths.txt`	I/O file paths
`defaultBT.txt`	Default boundary type specification

Appendix B. Implementation algorithm files

Table 5: Algorithm files of the `parjet` implementation.

File	Description	Subroutines included

`jet.f`	Main program	`cfl()`
		`init()`
		`stress()`
		`write_field()`
		`write_planes()`
		`read_field()`
		`vorticity()`
		`flux_x()`
		`flux_y()`
		`flux_z()`

`WallJetGrid.f`	Grid generation	`grid()`
`lsRK3.f`	Time advancement	`lsRK3()`

`transp3.f`	Data transpose	`init_transpose()`
		`tposei2k()`
		`tposek2i()`

`rhs_x.f`
`rhs_y.f`
`rhs_y.f`
	Spatial integration	`rhs_x()`
		`rhs_y()`
		`rhs_z()`

`tridsol.f`	Matrix solver	`trid_cyc()`

`der1_O6.f`	Spatial derivative	`der1x()`
		`der1y()`
		`der1z()`

`bound.f`	Boundary cond.	`bound()`

Continued on next page

File	Description	Subroutines included
		`topInfVel`
`inprof_func.f`	Inlet profile	`inprof_func()` `arctanh()`

`turbinflowGen.f`	Inlet disturbances	`turbinflowInit()`
		`turbinflowFunc()`
		`turbinflowStat()`
		`turbinflowRead()`

`filt04-06exp_new.f`	Filter	`filterx()`
		`filtery()`
		`filterz()`

`filt02_new.f`	Scalar filter	`filt02x()`
		`filt02y()`
		`filt02z()`

`jetstat.f`	Statistics	`jet_ProfAvFavre2Func()`
interp996.for	Interpolation	`interp996()`

Appendix C. Boundary layer statistics.

Table 6: Definition of boundary layer statistics variables in routine `jet_ProfAvFavreFunc()`.

Variable	Definition	Description
`tau_w(imax)`	$\tau_w = \mu \frac{\partial \overline{U}_{y=0}}{\partial y}$	Wall friction
`u_tau(imax)`	$u_\tau = \sqrt{\tau_w / \overline{\rho}_{y=0}}$	Friction velocity
`yplus(imax,kmax)`	$y^+ = y/l^* = y/(\nu/u_\tau)$	Wall units

Appendix D. Averaged statistics

Table 7: Statistics variables in routine `jet_ProfAvFavreFunc()`.

Favre decomposition		Reynolds decomposition	
VARIABLE	DEFINITION	VARIABLE	DEFINITION
Average profiles			
u_avF	$\widetilde{u} = \langle \rho u \rangle / \langle \rho \rangle$	u_avR	$\overline{u} = \langle u \rangle$
v_avF	$\widetilde{v} = \langle \rho v \rangle / \langle \rho \rangle$	v_avR	$\overline{v} = \langle v \rangle$
w_avF	$\widetilde{w} = \langle \rho w \rangle / \langle \rho \rangle$	w_avR	$\overline{w} = \langle w \rangle$
r_avF	$\widetilde{\rho} = \langle \rho \rangle$	r_avR	$\overline{\rho} = \langle \rho \rangle$
e_avF	$\widetilde{E}_t = \langle \rho E_t \rangle / \langle \rho \rangle$	e_avR	$\overline{E}_t = \langle E_t \rangle$
Turbulent fluctuations			
urmsF	$u'' = \sqrt{\langle (u - \widetilde{u})^2 \rangle}$	urmsR	$u' = \sqrt{\langle (u - \overline{u})^2 \rangle}$
vrmsF	$v'' = \sqrt{\langle (v - \widetilde{v})^2 \rangle}$	vrmsR	$v' = \sqrt{\langle (v - \overline{v})^2 \rangle}$
wrmsF	$w'' = \sqrt{\langle (w - \widetilde{w})^2 \rangle}$	wrmsR	$w' = \sqrt{\langle (w - \overline{w})^2 \rangle}$
yrmsF	$\theta'' = \sqrt{\langle (\theta - \widetilde{\theta})^2 \rangle}$	yrmsR	$\theta' = \sqrt{\langle (\theta - \overline{\theta})^2 \rangle}$
Reynolds stresses			
uvF	$\widetilde{u''v''} = \langle \rho u'' v'' \rangle / \overline{\rho}$	uvR	$\overline{u'v'} = \langle u'v' \rangle$
uwF	$\widetilde{u''w''} = \langle \rho u'' w'' \rangle / \overline{\rho}$	uwR	$\overline{u'w'} = \langle u'w' \rangle$
vwF	$\widetilde{v''w''} = \langle \rho v'' w'' \rangle / \overline{\rho}$	vwR	$\overline{v'w'} = \langle v'w' \rangle$
uuF	$\widetilde{u''u''} = \langle \rho u'' u'' \rangle / \overline{\rho}$	vvF	$\widetilde{v''v''} = \langle \rho v'' v'' \rangle / \overline{\rho}$
wwF	$\widetilde{w''w''} = \langle \rho w'' w'' \rangle / \overline{\rho}$		
Kinetic energy			
meanKxF	$\widetilde{K}_x = \frac{1}{2}\overline{\rho}\widetilde{u}\widetilde{u}$	meanKxR	$\overline{K}_x = \frac{1}{2}\overline{\rho u u}$
meanKyF	$\widetilde{K}_y = \frac{1}{2}\overline{\rho}\widetilde{v}\widetilde{v}$	meanKyR	$\overline{K}_y = \frac{1}{2}\overline{\rho v v}$

Continued on next page

Favre decomposition		Reynolds decomposition	
VARIABLE	DEFINITION	VARIABLE	DEFINITION
`meanKzF`	$\widetilde{K}_z = \frac{1}{2}\overline{\rho}\widetilde{w}\widetilde{w}$	`meanKzR`	$\overline{K}_z = \frac{1}{2}\overline{\rho w w}$
`KxF`	$\widetilde{k}_x = \frac{1}{2}\overline{\rho u'' u''}$	`KxR`	$\overline{k}_x = \frac{1}{2}\overline{\rho u' u'}$
`KyF`	$\widetilde{k}_y = \frac{1}{2}\overline{\rho v'' v''}$	`KyR`	$\overline{k}_y = \frac{1}{2}\overline{\rho v' v'}$
`KzF`	$\widetilde{k}_z = \frac{1}{2}\overline{\rho w'' w''}$	`KzR`	$\overline{k}_z = \frac{1}{2}\overline{\rho w' w'}$

References

Adam, Y. 1977 Highly accurate compact implicit methods and boundary conditions. *J. Comp. Phys.* **24**, 10–22.

Bédat, B., Egolfopoulos, F. N. & Poinsot, T. 1999 Direct numerical simulation of heat release and NO_x formation in turbulent premixed flames. *Combust. Flame* **119**, 69–83.

Boersma, B. J. 2004 Numerical simulation of the noise generated by a low Mach number, low Reynolds number jet. *Fluid Dyn. Res.* **35** (6), 425–447.

Canuto, C., Hussaini, M. Y., Quarteroni, A. & Zang, T. A. 1987 *Spectral methods in Fluid Dynamics*. Springer-Verlag.

Chapman, S. & Cowling, T. G. 1990 *The mathematical theory of non-uniform gases*, 3rd edn. Cambridge University Press.

Colonius, T. 2004 Modeling artificial boundary conditions for compressible flow. *Ann. Rev. Fluid Mech.* **36**, 315–345.

Eriksson, J. G., Karlsson, R. I. & Persson, J. 1998 An experimental study of a two-dimensional plane turbulent wall jet. *Experiments in Fluids* **25**, 50–60.

Fischer, P. F., Kruse, G. W. & Loth, F. 2002 Spectral element methods for transitional flows in complex geometries. *J. Sci. Comp.* **17**, 81–98.

Freund, J. B. 1997 Proposed inflow/outflow boundary condition for direct computation of aerodynamic sound. *AIAA Journal* **35** (4), 740–742.

Hirsh, R. S. 1975 Higher order accurate difference solutions of fluid mechanics problems by a compact differencing technique. *J. Comp. Phys.* **19**, 90–109.

Karniadakis, G. E. 1989 Spectral element simulations of laminar and turbulent flows in complex geometries. *Appl. Numer. Math.* **6**, 85–105.

Karniadakis, G. E. & Orzsag, S. A. 1993 *Algorithmic Trends in Computational Fluid Dynamics*. Springer-Verlag.

Kim, J., Moin, P. & Moser, R. D. 1987 Turbulence statistics in fully developed turbulent channel flow at low reynolds number. *J. Fluid Mech.* **177**, 133–166.

Klein, M., Sadiki, A. & Janicka, J. 2003 A digital filter based generation of inflow data for spatially developing direct numerical or large eddy simulations. *J. Comp. Phys.* **186**, 652–665.

Kou, K. K. 1986 *Principles of Combustion*. John Wiley.

Lele, S. K. 1992 Compact finite differences with spectral-like resolution. *J. Comp. Phys.* **103**, 16–42.

Levin, O. 2005 Numerical studies of transition in wall-bounded flows. PhD thesis, Royal Institute of Technology, KTH.

Levin, O., Chernoray, V. G., Löfdahl, L. & Henningson, D. 2005 A study of the blasius wall jet. *J. Fluid Mech.* **539**, 313–347.

Lundbladh, A., Berlin, S., Skote, M., Hildings, C., Choi, J., Kim, J. & Henningson, D. S. 1999 An efficient spectral method for simulation of incompressible flow over a flat plate. *Tech. Rep*. Dept. of Mechanics, Royal Instutute of Technology.

Pantano, C., Sarkar, S. & Williams, F. A. 2003 Mixing of a conserved scalar in a turbulent reacting shear layer. *J. Fluid Mech.* **481**, 291–328.

Rowley, W. R. & Colonius, T. 2000 Discretely nonreflecting boundary conditions for linear hyperbolic systems. *J. Comp. Phys.* **157**, 500–538.

Schlichting, H. 1979 *Boundary Layer Theory*, 7th edn. McGraw-Hill.

Skote, M. & Henningson, D. S. 2002 Direct numerical simulation of a separated turbulent boundary layer. *J. Fluid Mech.* **471**, 107–136.

Snir, M., Otto, S., Huss-Lederman, S., Walker, D. & Dongarra, J. 1996 *MPI: The Complete Reference*. The MPI Press.

Spalart, P. R. 1988 Direct numerical simulation of a turbulent boundary layer up to $Re_\theta = 1410$. *J. Fluid Mech.* **187**, 61–98.

Stanley, S. A., Sarkar, S. & Mellado, J. P. 2002 A study of flow-field evolution and mixing of in a planar turbulent jet using direct numerical simulation. *J. Fluid Mech.* **450**, 377–407.

Tannehill, J. C., Anderson, D. A. & Pletcher, R. H. 1997 *Computational Fluid Mechanics and Heat Transfer*, 2nd edn. Taylor & Francis.

Wang, Y. & Trouvé 2005 Direct numerical simulation of nonpremixed flame-wall interactions. *Combust. Flame* **144**, 461–475.